Department of Precision and Microsystems Engineering

Tunable Magnets: Dynamic Flux-feedback Compensation Methods for Improved Magnetization State Tuning Performance and Minor-loop Magnetization State Tuning for the Validation and Reduction of the Break-even Tuning Interval

R. Meijer

Report no : 2021.049
Supervisors : Dr. S.H. HosseinNia & Dr. A. Hunt
Specialisation : Mechatronic System Design
Type of report : MSc Thesis
Date : July 30 2021

Tunable Magnets

Dynamic Flux-feedback Compensation Methods for Improved Magnetization State Tuning Performance

and

Minor-loop Magnetization State Tuning for the Validation and Reduction of the Break-even Tuning Interval

by

R. Meijer

to obtain the degree of Master of Science
at the Delft University of Technology,
to be defended publicly on Friday August 20, 2021 at 09:00 AM.

Student number:	4431804	
Project duration:	September 1, 2020 – August 20, 2021	
Thesis committee:	Dr. ir. S.H. HosseinNia	TU Delft, project supervisor
	Dr. Ir. A. Hunt	TU Delft, daily supervisor
	Ir. J. W. Spronck	TU Delft, independent examiner

An electronic version of this thesis is available at `http://repository.tudelft.nl/`.

TU Delft

Preface

In the execution and writing of this research, I have been fortunate to receive help from many people dear to my heart.

First of all, I would like to thank the academic staff and students present in the weekly meetings for providing invaluable feedback during the execution of the project.

Thanks as well to my friends at the Formula Student Team Delft, my time at the team has really inspired and helped me to discover my interest in precision engineering.

A special thanks as well to my supervisors Hassan and Andres, whose feedback and continuous support have motivated me to make the most of this work - I really enjoyed working on the project with you.

Thanks to my life-long friends: Jens, Martijn, Ramon, Robert, Sjors, Xander and Youri for all the fun times we have had over the years - and will undoubtedly have in the future.

A special thanks to my parents and brother for always loving and supporting me in my private and academic endeavours.

Lastly, a loving thank you to my girlfriend Debra for loving me unconditionally and through the years making me the best version of me.

Dedicated to and in loving memory of my grandfather Joop, for sparking what will undoubtedly be a life-long interest in mechanical engineering.

R. Meijer
Delft, July 2021

Summary

In precision engineering, thermal stability is of great importance in order to keep up with the ever-increasing demand for faster and more precise positioning actuators. Most notably, actuator magnetizing coils dissipate heat to surrounding machine components as a result of Joule heating. With changing temperatures, system components expand and contract - causing unwanted structural deformations that can lead to a decline in positioning accuracy and repeatability. This phenomenon is especially pronounced in quasi-static processes that operate in a vacuum environment – examples of which can be found in lithography mirror alignment systems, deformable space mirrors and magnetic gravity compensators.

In prior TU Delft research by S.G. Viëtor a method to accurately tune a low-coercivity AlNiCo 5 magnet to a set of user-predefined magnetization states was introduced – the novel Tunable Magnet (TM) actuator. This way, by precisely 'tuning' the magnet with a sequence of short current pulses, the magnetization state is sustained even after tuning - making this method especially efficient for quasi-static operation. In order to advance the development of functional TM actuators, this research provides four contributions.

First, limitations within the original setup have prohibited dynamic stage movements, which in practice make a reluctance actuator functional. By designing and building a compliant module that can be attached to the existing setup, this discrepancy is overcome – making dynamic-gap experimentation possible.

Second, magnetization state tuning robustness, accuracy and repeatability are significantly improved by introducing a series of four dynamic compensation methods: Dynamic Recoil-line Slope (DRS), Dynamic Air-gap (DA) and Fringe Flux-loss (FF) compensation improve tuning predictions by more accurately accounting for dynamic air-gap effects. In conjunction, a Parallel PI (PPI) flux-feedback controller is used to reduce the remaining errors in the magnetized state.

Third, a novel Minor-loop Magnetization State Tuning (MMST) approach is proposed as a replacement of the original Saturation Magnetization State Tuning (SMST) major loop algorithm. The new method eliminates the need for a saturation step within the tuning sequence, in turn yielding improved energy efficiency, dynamic behavior and tuning times.

Lastly, the Break-even Tuning Interval (BTI) metric as introduced by prior work has been experimentally validated – allowing for a comparison between TM and conventional electromagnetic (EM) actuators. This also allows for an extrapolation of the validated predictions, estimating the limits of TM performance and applications if tuning times were to be reduced in future work.

Contents

List of Figures

List of Tables

Glossary

List of Acronyms

TU	Technische Universiteit
PME	Precision and Microsystems Engineering
MSD	Mechatronic System Design
TM	Tunable Magnet
EM	Electromagnet
PM	Permanent Magnet
EPM	Electropermanent Magnet
MMF	Magnetomotive Force
EMF	Electromotive Force
BTI	Break-Even Tuning Interval
AlNiCo	Aluminium-Nickel-Cobalt
NdFeB	Neodymium-Iron-Boron
SmCo	Samarium-Cobalt
MGC	Magnetic Gravity Compensator
SMST	Saturation Magnetization State Tuning (method)
MMST	Minor-loop Magnetization State Tuning (method)
DRS	Dynamic Recoil-line Slope (compensation)
DA	Dynamic Air-gap (compensation)
FL	Fringe-flux Loss (compensation)
PPI	Parallel PI (flux-feedback control)
OpAmp	Operational Amplifier
RTI	Real Time Interface
DEMO	Dienst Elektrische en Mechanische Ontwikkeling (hardware support division TU Delft)
LPF	Low Pass Filter
PCB	Printer Circuit Board

List of Symbols

Symbol	SI Unit	Name
$\Delta B_r'$	T	load-line error
Δx_{MAE}	m	MAE accuracy position error
$\Delta x_{3\sigma}$	m	3σ repeatibility position error
η	-	efficiency
μ_0	Hm^{-1}	permeability of free space
μ_{max}	-	maximum relative permeability of BH-curve
μ_r	-	relative permeability
μ_{rec}	-	relative recoil permeability
$\mu_{r,y}$	-	average St. 37 yoke relative permeability
ρ_c	Ωm	resistivity of copper
ρ_{al}	Ωm	resistivity of AlNiCo
σ	-	standard deviation
ϕ_m	Wb	magnet flux
ϕ_g	Wb	air-gap flux
ϕ_c	Wb	magnetic circuit flux
χ_v	-	volume magnetic susceptibility
ω_c	rad	crossover frequency
ω_{cl}	$rads^{-1}$	closed loop bandwidth
A_m	m^2	magnet cross-sectional area
A_g	m^2	air-gap cross-sectional area
A_w	m^2	wire cross-sectional area
b_c	m	coil width
b_f	m	compliant flexure in-plane width
B_c	T	corner-point flux density
B_g	T	air-gap flux density
B_g^{set}	T	air-gap flux density set-point
B_m	T	magnet flux density
B_o	T	magnet operating-point flux density
B_r	T	maximum remanent flux density
$B_r^{'}$	T	setpoint remanent flux density
B_{rec}	T	linearized recoil line flux density
B_{sat}	T	saturation flux density
$C(s)$	-	controller
d_c	m	average coil diameter
$d_{contact}$	m	magnet-pole piece contact distance
d_{cm}	m	magnet position w.r.t. pole pieces
d_m	m	magnet diameter
d_w	m	coil wire diameter
E	J	energy
f	Hz	frequency
f_{bw}	Hz	bandwidth
f_{pwm}	Hz	PWM switching frequency
f_s	Hz	sampling frequency
f_{-3dB}	Hz	-3 dB cut-off frequency
F_g	N	force exerted by magnet
F_s	N	force exerted by compliant spring
F_0	N	constant bias force
$\mathscr{F}_M MF$	AT	saturating MMF
$G(s)$	-	plant
G_0	-	plant DC gain
h_p	m	pole piece height

Symbol	SI Unit	Name
H_c	Am^{-1}	corner-point field intensity
$H_{c,i}$	Am^{-1}	magnet intrinsic coercivity
H_g	Am^{-1}	air-gap field intensity
h_k	m	mover height
H_m	Am^{-1}	magnet field intensity
H_o	Am^{-1}	magnet operating point field intensity
H_{sat}	Am^{-1}	saturation field intensity
I	A	coil current
I_{sat}	A	saturation coil current
ΔI_{pp}	A	peak-to-peak current noise
J	Am^{-2}	current density
k_1	-	flux leakage coefficient
k_2	-	MMF loss factor
l_f	m	compliant stage flexure length
l_g	m	air-gap length
l_w	m	wire length
$L(s)$	-	loop gain
L	H	selft inductance
l_m	m	magnet length
l_k	m	mover length
l_p	m	pole piece length
M	Am^{-1}	permanent magnet magnetization
MMF_m	A	magnet magnetomotive force
MMF_g	A	gap magnetomotive force
n	-	number of magnetizing coil turns
p_k	-	polynomial coefficients
P	Js^{-1}	power
R	Ω	resistance
$\mathscr{R}$	H^{-1}	reluctance
$\mathscr{R}_g$	H^{-1}	air-gap reluctance
$\mathscr{R}_m$	H^{-1}	permanent magnet reluctance
$\mathscr{R}_y$	H^{-1}	yoke reluctance
s_x	m	compliant spring displacement
t	s	time
t_f	m	compliant flexure thickness
T_{be}	s	*Break-Even Tuning Interval*
T_s	s	sampling period
U_{ADC}	V	analog to digital voltage range
U_s	V	power source voltage
U_{sat}	V	saturation voltage
ΔU_{pp}	V	peak-to-peak voltage noise
w_k	m	mover width
w_p	m	pole piece width

1 Introduction

1.1. Motivation

In precision engineering, thermal stability is of great importance in order to keep up with the ever-increasing demand for faster and more precise positioning actuators. Most notably, actuator magnetizing coils dissipate heat to surrounding machine components as a result of Joule heating. With changing temperatures, system components expand and contract - causing unwanted structural deformations that can lead to a decline in positioning accuracy and repeatibility [11, 15].

Traditionally, Lorentz actuators were favored for high-precision applications, due to their inherently linear force-current relationship - making them highly predictable [21]. This type of actuator, however, is also characterized by a low force density - which results in relatively poor efficiency [27]. In recent years, the control predictibility of modern reluctance actuators has improved significantly – allowing for up to 10 times larger force density compared to Lorentz actuators [27]. This allows the designer to greatly reduce the actuator size, and thus magnetizing current required for positioning - which in turn improves efficiency [17].

Still, the effect of Joule heating within an electromagnetic (EM) reluctance actuator remains especially pronounced during quasi-static operation, where the magnetizing current must be sustained for extended periods of time. Additionally, many high–precision systems operate within challenging conditions - often requiring large bias forces in a vacuum environment. On one hand, a large a bias force worsens the effect of Joule heating as it scales quadratically with the magnetizing current. Conversely, vacuum operation prevents the dissipation of heat through convection - making it even more difficult to achieve thermal stability. Three major contributing factors can therefore be attributed to component deformation:

- Quasi-static operation, which requires extended periods of magnetizing current
- A large bias force, which quadratically increases the required magnetizing current
- Vacuum operation, which severely limits heat dissipation

Adaptive optical systems used in deformable space mirrors can be considered as an application area that suffers from some of the limitations summarized before [14]. For the system shown in figure 1.1a, sampling periods can range from seconds to months. During this time, it is paramount that actuator position is held in the range of several nanometers of precision. Clearly, this constitutes as a quasi-static operating principle - and the fact that it operates in the vacuum of space prohibits convective cooling opportunities.

Another area of application can be found in EUV lithography machines [1], depicted in figure 1.1b. Here, the alignment of optical components that guide a beam of extreme ultraviolet light is considered. The light originates from the source, and is guided using a series of mirrors towards the reticle pattern - after which it hits a silicon wafer. Especially during exposure, mirror alignment must be guaranteed to be within sub-nanometer range - placing great importance on mirror accuracy and stability. The latter can be difficult to accomplish, because the mirror set operates in a vacuum - possibly causing component deformation due to quasi-static Joule heating.

(a) (b)

Figure 1.1: Applications for TM control: the deformable space mirror by [14] in (a). An EUV lithography machine - manufactured by [1] - shown in (b).

Within the same machine, a Magnetic Gravity Compensator (MGC) ensures that external vibrations do not cause disturbances to the sensitive mechanical components [8, 10, 28]. MGC's are characterized by enabling quasi-zero stiffness in the direction of the compensator - an example of which is shown in figure 1.2. Permanent magnets are often used to provide a large counter-gravity bias force - but incoming disturbance frequencies must be mitigated by the magnetizing coils. Especially for low-frequency high-amplitude disturbances, these magnetizing currents must be applied for extended time periods - heating up a subsystem that is also placed in a vacuum. Therefore, this application suffers from all of the three previously introduced design challenges.

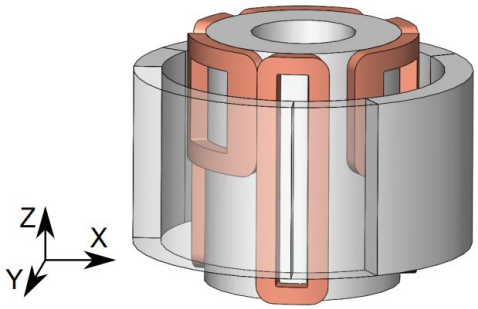

Figure 1.2: Magnetic Gravity Compensator module developed by [8]. The inner ring can remains stationary, consisting of a permanent magnet ring and six magnetizing coils. The the outer ring acts like a mover.

In order to improve total system accuracy and repeatibility, we must therefore find a method to minimize the energy loss of the magnetizing coil at low operating frequencies and for large displacements.

1.2. Prior Art

Prior research has attempted to find methods that improve actuator efficiency for quasi-static operation. Typically, the methods propose a variation of a hybrid reluctance actuator topology - using low-coercivity AlNiCo permanent magnet materials to make use of its nonlinear hysteresis curve. The AlNiCo magnet can be more easily (de-) magnetized when compared to hard NdFeB magnets typically found in hybrid reluctance actuators[3, 20, 22]. This way, by precisely 'tuning' the magnet to the desired magnetization state with a series of short current pulses, the magnet sustains the magnetized state after tuning - even after all current has subsided. During stationary periods, little to no additional energy loss is expected, which makes this method especially efficient for quasi-static operation.

A.N. Knaian was first to introduce the concept of in-situ magnetization adjustment of AlNiCo, with the switchable Electropermanent Magnet (EMP) actuator as shown in figure 1.3a [13]. In parallel with the soft AlNiCo magnet, a hard NdFeB magnet is placed - both surrounded by a single magnetizing coil. The magnets have approximately the same remanent flux density, causing the two magnets to directly oppose each other in the 'off'-state. When current is sent through the coil, the low-coercivity AlNiCo is saturated while the NdFeB magnet is not. After the current has subsided, magnetic domains in the AlNiCo magnet have switched

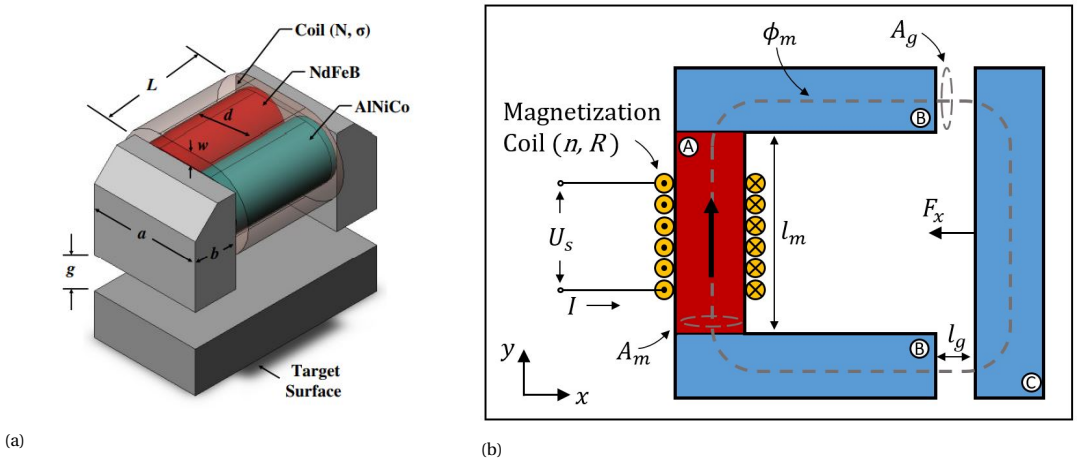

Figure 1.3: Two in-situ magnetization concepts. Knaian's EPM actuator (a) allows for a switching behavior, whilst Viëtor's TM actuator allows for intermediate tuning steps.

around, and are now sustained in the same direction as the NdFeB magnet. This way, the circuit is switched 'on' - pulling the mover towards the stator indefinitely.

In 2018, S.G. Viëtor introduced a method to accurately tune an AlNiCo magnet to a set of user-predefined magnetization states [26]. Contrary to Knaian's 'on'- and off-state, this novel method allows for a selection of intermediate states - allowing the user to set the circuit air-gap flux density level with 25 mT increments. The three largest contributions from the work can be summarized as the development of the novel Saturation Magnetization State Tuning (SMST) algorithm, experimental validation of TM performance on a practical static-gap setup - shown in figure 1.3b - and the introduction of the Break-even Tuning Interval (BTI) metric - which allows for an efficiency comparison between novel TM and conventional EM actuators.

1.3. Problem Definition

This research is a continuation of the work performed by [26], and part of an ongoing research program investigating the application of in-situ magnetization adjustment of AlNiCo magnets. While the work performed prior to this research establishes a robust method of TM control for reluctance actuators, it is not yet mature enough to be implemented in practice. Part of the limitations originate from the setup used - which only allows a change of the air-gap length inbetween tuning cycles. During each cycle, the gap length is fixed - contrary to the movement that makes a reluctance actuator functional. In order to represent proper actuator dynamics, the setup must be expanded in order to allow for these movements during the tuning cycle.

Experimental results from [26] also reflect this discrepancy: for a known air-gap length of 1 mm, accuracy and repeatibility are excellent - with below 3 mT Mean Average Error (MAE) and sub-1 mT 3σ repeatibility performance. However, an air-gap of 1.5 mm already causes these performance metrics to worsen, with accuracy declining to at least $MAE = 7mT$ - even with a static air-gap during the tuning process. It is believed that these discrepancies originate from improper corner-point predictions of the tuning algorithm, which can be illustrated by figure 1.4 and equation (1.1).

$$B_m = -\mu_0 \cdot \frac{k_1}{k_2} \frac{A_g l_m}{2 A_m l_g} \cdot \left(H_m - \frac{nI}{l_m} \right) \tag{1.1}$$

Equation (1.1) describes the load-line as illustrated by figure 1.4. The slope is determined by two variables that are non-constant in a dynamic system: air-gap length l_g and corresponding fringe flux-loss factor k_1. Moreover, recoil-line slopes have been shown by [26] to be of non-constant value as well. If these complications are not properly accounted for, we obtain the wrong the corner-point estimation - translating to a reduction in accuracy and thus increase in MAE. For this reason, increased variable-gap robustness and prediction accuracy is required in order to make the TM method suitable for dynamic operation.

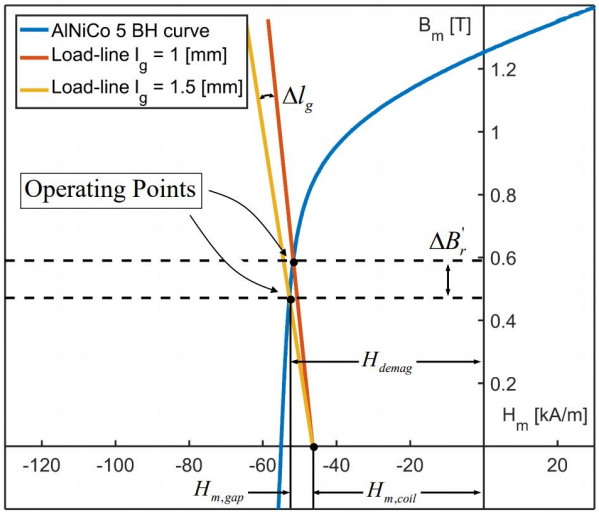

Figure 1.4: The magnetizing error - $\Delta B_r'$ - results from insufficient corner-point prediction accuracy.

Additionally, prior research has voiced concerns over the saturation step of the TM tuning cycle [26]. Performing this step requires large magnetizing currents, which in turn can cause excessive pulling forces between the actuator stator and mover. This issues no concern in a static-gap setup, but when the actuator is allowed to move, this force can cause large initial deflections - possibly resulting in long settling times and increased component stress. Furthermore, the large power draw during saturation means that although short in comparison to demagnetizing, this tuning step accounts for at least half of the energy losses of a TM tuning cycle - therefore limiting efficiency and worsening estimated BTI [26].

The BTI metric, however, up to this point remains invalidated. Experimentally validating this metric would allow for a more confident extrapolation of the observed results. This way, a prediction of achievable TM actuator performance for improved tuning times can be made - which will yield greater insight into the possible areas of TM actuator application and performance limitations.

To summarize, the limitations of prior research span two categories. The first concerns dynamic-gap performance, which cannot be evaluated due to the incompatible experimental setup and predictor inaccuracies. The second revolves around energy-loss performance, where the BTI estimator remains invalidated and the saturation step of the TM magnetization algorithm is believed to limit both actuator efficiency as well as dynamic performance.

1.4. Research Goal and Objectives

Taking into account the limitations listed above, this research will offer the next contribution to the original goal set back in 2018 - in the pursuit of efficient quasi-static actuator operation:

Develop a Tunable Magnet that can be robustly tuned in the presence of a dynamically varying air-gap and investigate its use in precision actuation systems.

We will contribute to this goal by realizing the following objectives:

1. **To increase robustness and performance of the magnetization state tuning algorithm.** This will be achieved by using a series of compensation methods: Dynamic Recoil-line Slope (DRS), Dynamic Air-gap (DA), Fringe Flux-loss (FF) and Parallel PI (PPI) flux-feedback control. Using the analytical compensators combined with feedback control will allow for more precise magnetization state tuning, even for extreme and dynamically changing air-gap lengths - in turn improving robustness, accuracy and repeatibility.

2. **To design and build a demonstrator capturing the motions of a moving TM actuator.** Using a compliant flexure system, the existing setup will be expanded with a modular subassembly that allows for

experimentation under changing air-gap conditions. This will allow the user to investigate dynamic effects of different tuning methods and unlocks the validation of the BTI metric.

3. **To perform an experimental validation of the Break-even Tuning Interval.** For a range of tuning times and gap magnetization levels, the BTI calculations as introduced in 2018 will be experimentally validated. Using this, projections for energy loss and BTI performance at short tuning times will be performed - allowing for better understanding of possible future areas of application.

4. **To introduce a novel Minor-loop Magnetization State Tuning (MMST) method in order to increase the energy efficiency and dynamic behaviour of the TM actuator.** By proposing a new magnetization state tuning algorithm making use of minor hysteresis loops, the amount of energy loss can be significantly decreased. This reduces BTI values, making the TM actuator more widely applicable. Simultaneously, the new method will provide improvements in dynamic system movements and tuning times.

1.5. Thesis Outline

Chapter 2 contains the foundation upon which the TM state-magnetization methods presented by [26] and this research are built. Subject experts may wish to skip this chapter, but for the reader that wishes to see the basics of these principles shortly summarized, this might provide an appropriate introduction to the subject. The contributions presented by this research are written in scientific paper-format within chapters 3 and 4. In chapter 3: *Tunable Magnets: Design and Control of a Gap-closing Reluctance Actuator using Dynamic Flux-feedback Compensation Methods*, objectives 1 and 2 are realized. Objectives 3 and 4 are elaborated in chapter 4: *Tunable Magnets: Validation and Reduction of the Break-even Tuning Interval using Minor-loop Magnetization State Tuning*.
In chapter 5, conclusions are drawn from the research as a whole. Additionally, recommendations are provided in order to advance the development of TM actuators in future research.

Supplementary materials are attached within four appendices. Appendix A provides a detailed overview of the pre-existing setup, along with the new hardware components introduced by this research. Appendix B details the programs and scripts used in the state-tuning algorithm software. To complete the experimental setup, datasheets of newly introduced components are provided in appendix C. Lastly, an overview of recommended literature is placed in appendix D, for readers interested to learn more about magnetism and TM actuators.

2

Preliminary: An Introduction to Tunable Magnet Control

2.1. Fundamentals of Permanent Magnetism

This section covers the basics of permanent magnetism and its importance to Tuneable Magnet (TM) applications. The theory of basic magnetics in this section is mostly derived from the books by P. Campbell, H.C. Roters and R.J. Parker [3, 20, 22], whereas TM state-of-the-art has been adapted from the work of S.G. Viëtor and A.N. Knaian [13, 26].

2.1.1. Magnetizing Force and Magnetic Domains

A material can be permanently magnetized when it is susceptible to an applied magnetic field and capable of sustaining its own magnetic flux in the absence of said external field. Magnetic susceptibility - often denoted as χ_v - is a dimensionless material property, and can vary with the ratio and type of materials used in the permanent magnet (PM) alloy. A material that is susceptible to magnetization can be magnetized by the following sequence of events, which are also shown in figure 2.1.

1. A coil is wound around a piece of demagnetized material. The direction of magnetization in the small material domains - M - is at this stage randomly distributed, and results in a net magnetic flux over the material of $B \approx 0$.

2. The coil is connected to a voltage source. The wire has an arbitrary resistance R - dependent on material properties and geometry. Because of this, the applied voltage U_s corresponds with a current density J over the coil. This causes a magnetizing force H, which rotates the magnetization of the inner domains - M - along the direction of said magnetizing force. When the applied current density is large enough, the magnetic material can be driven to the saturation point - (H_{sat},B_{sat}). Here, almost all inner domains are aligned in the direction of H, and saturation flux density B_{sat} can be measured within the magnetic circuit.

3. The voltage is cut off and the current subsides. Because of this, the magnetized inner domains will slightly misalign again, but remain pointed in approximately the same direction. The sustained flux is called the remanent flux density - B_r, and remains even when no additional current is supplied to the coil. The material is now permanently magnetized.

The relationship between the applied voltage and magnetizing current can be described by Ohm's law:

$$I = \frac{U_s}{R} \tag{2.1}$$

Where I resembles the magnetizing current, U_s the supply voltage and R the resistance of the copper wire wound around the PM material. In turn, R can be determined by using:

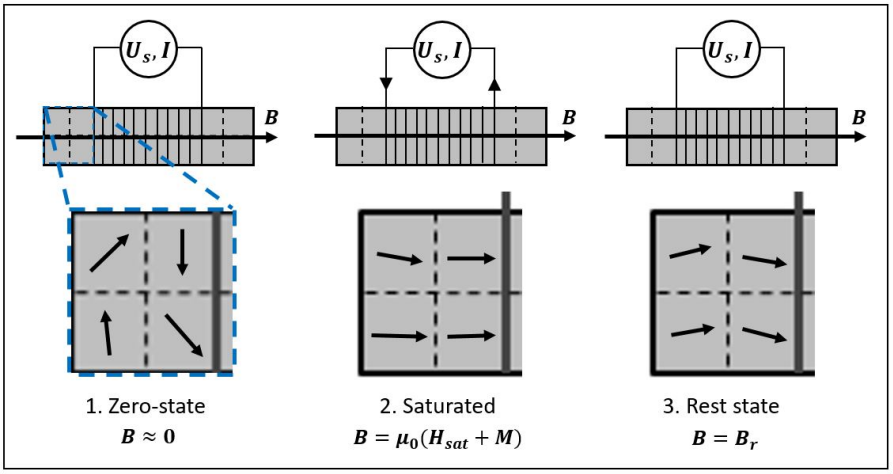

Figure 2.1: Three steps of permanent magnet (PM) magnetization. From the zero-state (left) to the saturated state (middle) and resting state (right).

$$R = \rho_c \frac{l_w}{A_w} \tag{2.2}$$

In equation (2.2), ρ_c resembles the electrical resistivity of copper, whereas l_w and A_w respectively describe the total coil wire length and wire cross-sectional area. The applied magnetic field H_m - otherwise known as the Magnetomotive Force (MMF) - can be written as:

$$H_m = \frac{nI}{l_m} \tag{2.3}$$

Where H_m is in $[Am^{-1}]$, with n as the amount of coil windings and l_m as the magnet length. Finally, magnet flux density B_m in $[T]$ can be expressed as:

$$B_m = \mu_0(H_m + M) \tag{2.4}$$

It can be seen that B_m is the product of the constant μ_0 - which represents the magnetic permeability of free space - and the sum of H_m and M, which describe the applied and intrinsic magnetic field of the PM material respectively. Once the current has subsided, H_m reverts to zero and the only remaining contribution to B_m is M. As mentioned before, this remaining magnetic field is called the remanent flux density - B_r. Together with coercivity, the basis for magnetic hysteresis can be explored in the next section.

2.1.2. Magnetic Hysteresis Curves, Coercivity and Remanent Flux Density

In this section, two important magnetic material properties - remanent flux density and coercivity - are discussed and translated to a magnetic hysteresis curve.

The magnetizing steps described in section 2.1.1 can be translated to an x-y graph in order to make the magnetization process more intuitive - as will be later shown in figure 2.2. On the x-axis, we plot the applied magnetic field (H_m), while the y-axis will represent the magnetic flux density of the permanent magnet (B_m). The resulting major hysteresis curve - from now on called BH-curve - relates the flux density that can be expected from the PM material for different applied magnetic field values. In figure 2.2, we consider the BH-curve of the magnetic material AlNiCo 5. Notice the arrows pointing in anticlockwise direction along the blue curve, indicating that the new magnetization state is dependent on what happened in the previous step. This means that we can only traverse the curve in the indicated direction towards saturation points ($\pm H_{sat}$,$\pm B_{sat}$)- which are positioned at at the tail-ends.

The blue curve shown in figure 2.2 originates from measurements [26], whereas the dotted black curve follows from literature [4]. The intersections between the major curve - in blue - and the H_m-axis are determined by a property called the coercivity of the magnetic material.

Magnetic coercivity refers to the ability of a permanent magnet material to withstand (de-)magnetization due to an externally applied magnetic field, measured in $[Am^{-1}]$. For instance, magnetizing materials with

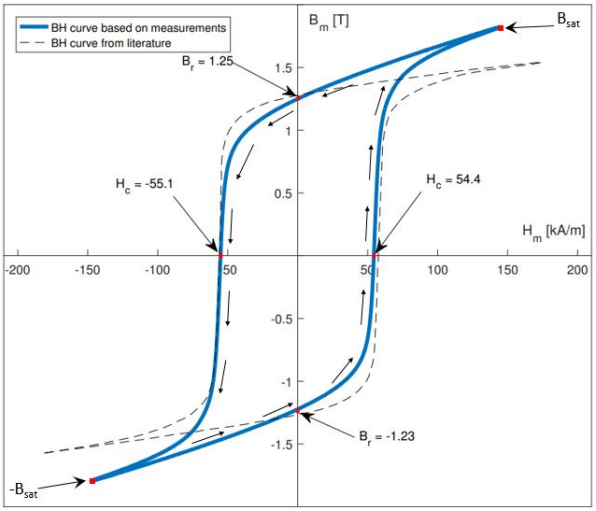

Figure 2.2: BH-curve of AlNiCo 5 based on both measurements [26] and literature [4]. H_m-axis intersections caused by the intrinsic coercivity denoted as H_c, B_m-axis intersections caused by remanent flux density B_r

a large magnetic coercivity - such as NdFeB - will require a large current density to be applied, thus making them more difficult to (de-)magnetize. Materials of this type are classified as hard PM materials [3, 20].

On the other hand, soft magnets such as AlNiCo can more easily be (de-)magnetized [3, 20]. For AlNiCo 5, values close to 150 $[kAm^{-1}]$ are often enough to fully saturate the magnet [9], with an intrinsic coercivity $H_{c,i}$ of 50 $[kAm^{-1}]$. Hard PM materials such as NdFeB and SmCo can have intrinsic coercivities that are orders of magnitude larger than this [5]. We can translate coercivity to BH-curve characteristics: a hard magnetic material yields a wide BH-curve, whereas a soft material yields a narrow curve.

The remanent flux density that sustains after the magnet has been saturated - otherwise known as saturation remanence - determines the largest value of B_r the magnet can keep at zero applied current. Of course, the magnet can be demagnetized in order to sustain smaller B_r values. These values are related to the so-called anhysteretic remanence curves, which make up the skeleton of the magnetic hysteresis curve - a history-dependent feature that will be explored in the next section. Remanence values vary with the PM material used: previously mentioned AlNiCo 5 holds a relatively large value of $B_r = 1.25T$ - similar to NdFeB magnets. Alternatively, SmCo magnets can display values as low as 0.8 T [5]. Because remanence determines the intersections between the major curve and the B_m-axis, the BH-curve will appear more stretched-out the along the y-axis for large values of B_r.

2.1.3. BH-Curve Properties: Knee-point, Recoil lines and Virgin Curve

In addition to the basic properties previously mentioned, some BH-curve properties can be distinguished that underline the history-dependent behavior of the curve. Of these, the most important properties are elaborated below.

When a magnetically susceptible material has never been magnetized before - or has returned to a close-to-zero state - it will not immediately walk along the major BH-curve. Instead, this close-to-zero state can be plotted at the origin of the BH-axes. When a saturating magnetic field is applied to the material, it will move along a so-called virgin magnetization curve, as shown in figure 2.3.

Also depicted in figure 2.3 is the knee-point, situated within the second quadrant of the BH-curve - marking the point of irreversibility. Starting from saturation B_r and by applying a large enough negative current, we can create a magnetic field in opposite direction. This way, we follow the major curve in an anticlockwise manner into the second quadrant of the curve, which is shown in detail in figure 2.4.

After surpassing the knee-point and entering the region of irreversibility, we can let go of the demagnetizing current. By doing this, however, we cannot return towards B_r along the major BH-curve. Instead, we trace one of the orange recoil loops, depending on the magnitude of the demagnetizing current. These loops

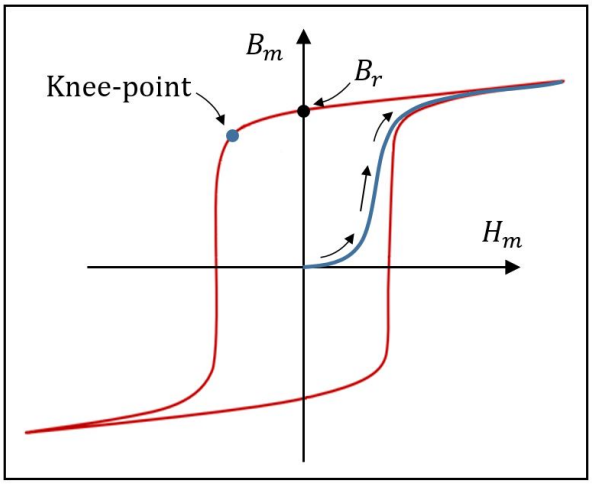

Figure 2.3: Virgin curve and second-quadrant knee-point

can be approximated by the black dotted recoil lines, and stretch the entire width of the second quadrant. The recoil lines are part of an infinite set of possible minor loops, which can be used to apply a remanent flux density to the magnet other than saturation B_r. The recoil loop and operating point reached depends on the magnetic circuit surrounding the PM material, as will become apparent in chapter 3.

2.2. Magnetic Circuit Properties and System Mechanics

As demonstrated in the thesis introduction, permanent magnets can be used in a variety of applications, such as magnetic gravity compensators (MGC) [8, 10, 11], adaptive telescopes [14] or EUV lithography mirror alignment systems [1]. Lorentz and Reluctance actuators often use permanent magnets within an electromagnetic circuit to move a mass to the desired position [17]. In this section, a variable-gap reluctance actuator with a C-shaped core is used as an example - also illustrated in figure 2.5.

The simplest magnetic circuit is achieved if all components in figure 2.5 are made of the same ferromagnetic material. Alternatively, it is possible to exchange component A for a permanent magnet material - such as highly-coercive NdFeB. This way, a hybrid reluctance actuator circuit is formed [17]. The geometry and features of an electromagnetic circuit greatly influence the system behaviour, and determine the operating point of the magnet. In order to understand this, we must find the equivalent magnetic circuit of our system - starting with the magnetic flux source.

2.2.1. Magnetic flux source

Finding the equivalent magnetic circuit is analogous to the way electrical circuits can be constructed. In an electrical system, the flow of electrons is initiated by a voltage source, which subsequently results in an electric current flowing through the circuit. In a magnetic circuit, the flux (ϕ_m) can be seen as the equivalent of electrical current.
As elaborated previously in section 2.1, magnetic flux is caused by the MMF, which in turn can be generated by applying a current density to a coil wound around a magnetically susceptible material. Suppose that all components in figure 2.5 are made of the same material - which is not a permanent magnet. In this instance, the flux generated in component A is solely dependent on coil MMF, which can be determined by using:

$$\text{MMF}_c = n \cdot I \tag{2.5}$$

If we were to replace the coil with on a pre-magnetized PM material for component A, we can find the MMF as:

$$\text{MMF}_m = \frac{B_m l_m}{\mu_0} \tag{2.6}$$

Here, B_m resembles the flux density sustained by the permanent magnet. Putting the coil back into the system - in conjunction with the permanent magnet - would result in a series of magnetic flux sources. Thus,

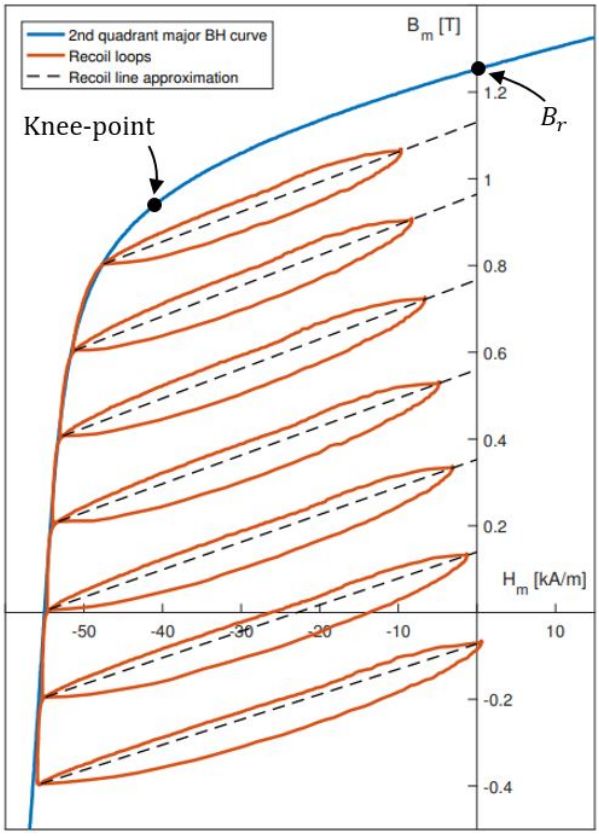

Figure 2.4: Detailed view of the second quadrant of the AlNiCo 5 BH-curve, adapted from [26]. Highlighted is an approximate location of the knee-point, orange and dotted lines indicate measured and approximated recoil curves respectively.

both MMF-contributions would add up to the total system magnetic flux density. This is further strengthened by equation (2.4), where it was shown that total system magnetic flux is equivalent to the sum of applied (coil) and sustained (PM) fields.

2.2.2. Component Reluctance

In the previous section, it was shown how we can identify the system flux source. With these equations, we can determine the flux by substituting them into equation (2.7):

$$\phi_m = \frac{\mathrm{MMF}_m + \mathrm{MMF}_c}{\mathscr{R}} \tag{2.7}$$

Here, $\mathscr{R}$ resembles the reluctance of a circuit component - which can be seen as the magnetic equivalent of electrical resistance. Reluctance is determined by the degree of magnetic susceptibility of the components within the circuit. If electrical resistance can be described as previously mentioned by equation (2.2), notice the similarities with the equation used to find component magnetic reluctance:

$$\mathscr{R}_y = \frac{l_y}{A_y \mu_0 \mu_r} \tag{2.8}$$

Equation (2.8) was written for the yoke - components B and C - of the circuit shown in figure 2.5. The length and area of the yoke (l_y and A_y) are the dimensions that influence reluctance. Similar to resistance in a wire, both increasing yoke length and decreasing the cross-sectional area will increase reluctance. Additionally, we recognize μ_0 as the magnetic permeability of free space and μ_r as the relative permeability of the material, which depends on the material chosen for the yoke.

2.2.3. Circuit Reluctance

For the circuit shown in figure 2.5, we recognize six instances of component reluctance. Three of these can be attributed to the ferromagnetic yoke: components B and C. Additionally, PM component A has its own

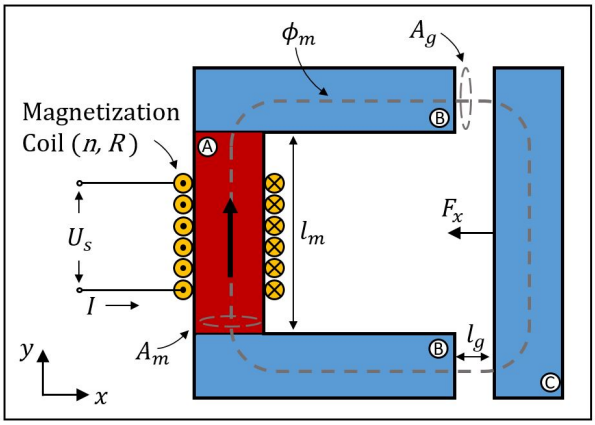

Figure 2.5: Typical layout of a gap-closing electromagnetic reluctance actuator. Component A can be a permanent magnet (hybrid actuator) or ferromagnetic yoke, and is excited by the magnetization coil with n turns and R resistance. Components B make up the ferromagnetic stator yoke. Component C is free-moving and of the same ferromagnetic material as B, closing and opening l_g as it moves from left to right. Magnetic flux is indicated with ϕ_m and moves in clockwise direction.

reluctance. Lastly, the reluctance of the two air-gaps must be taken into account when analyzing the entire circuit. We can simplify this by drawing a block diagram similar to electrical circuits, as is shown in figure 2.6.

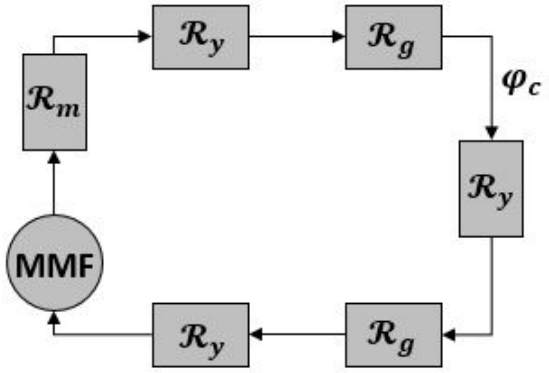

Figure 2.6: Simplified equivalent circuit, derived from figure 2.5. The MMF contributions of coil and PM are summed up as one flux source because of serial placement, $\mathcal{R}_m, \mathcal{R}_y, \mathcal{R}_g$ respectively as magnet, yoke and gap reluctance. ϕ_c as total circuit magnetic flux.

All components are placed in series, which means that the reluctances can be added up - similar to calculations within an electrical circuit. Using this feature, we can rewrite equation (2.7) to be compatible with our actuator topology:

$$\phi_c = \frac{MMF_c + MMF_m}{\mathcal{R}_m + 3 \cdot \mathcal{R}_y + 2 \cdot \mathcal{R}_g} \tag{2.9}$$

Here, it is assumed for simplicity that the mover component C and yoke components B have identical material and dimensional properties. Additionally, ferromagnetic yokes typically have very large values for μ_r. Therefore, these component reluctances become so small they can be considered negligible, which means we can eliminate them from this equation. Substituting equations (2.5), (2.6) and (2.8) into (2.10) then yields:

$$\phi_c = \frac{n \cdot I + \left(\frac{B_m l_m}{\mu_0}\right)}{\left(\frac{l_m}{A_m \mu_0 \mu_{r,m}}\right) + 2 \cdot \left(\frac{l_g}{A_g \mu_0 \mu_{r,g}}\right)} \tag{2.10}$$

As flux is the same at any point in the circuit, we can find the magnetic flux density through the magnet by realising that:

$$B_m = \frac{\phi_c}{A_m} \tag{2.11}$$

Substituting equations (2.4) and (2.10) into (2.11) then yields:

$$B_m = \frac{n \cdot I + \left(\frac{\mu_0 (H_m + M) l_m}{\mu_0}\right)}{\left[\left(\frac{l_m}{A_m \mu_0 \mu_{r,m}}\right) + 2 \cdot \left(\frac{l_g}{A_g \mu_0 \mu_{r,g}}\right)\right] \cdot A_m} \tag{2.12}$$

Some simplifications can be performed in order to make this equation more useable. First, we assume a saturating current starting at $(H_m, B_m) = (0,0)$. In this case, no sustained magnetic flux is present - eliminating M. If the magnet is being saturated, the relative permeability of the PM material approaches that of free space, setting $\mu_r = 1$. Assuming $\mu_{r,g} = \mu_{r,m} = 1$ and rewriting, we arrive at the following equation:

$$B_m = \frac{\left(\frac{\mu_0 n I}{l_m}\right) + \mu_0 H_m}{1 + \frac{2 A_m l_g}{A_g \mu_0}} \tag{2.13}$$

For values of A_m and l_g commonly found in precision actuator systems, $\frac{2 A_m l_g}{A_g \mu_0}$ can safely be assumed much larger than one due to the very small value of μ_0. In this case, using $\frac{2 A_g l_m}{A_g \mu_0 \mu_r} >> 1$, we can rewrite once more until we arrive at equation (2.14).

$$B_m = -\mu_0 \cdot \frac{A_g l_m}{2 A_m l_g} \cdot \left(H_m - \frac{n I}{l_m}\right) \tag{2.14}$$

Equation (2.14) is often called the load-line equation [3, 20], and is of great importance when determining the operating point of the permanent magnet.

2.2.4. Static Operation Load-line Construction

Looking closely at the load-line equation, we recognize again components B_m and H_m and with the BH-curve in mind, they still correspond to the y- and x-axis respectively. The equation can be subdivided into two important components: the load-line slope and H_m-axis shift. Both can be addressed with their own equation:

$$\text{slope} = -\mu_0 \cdot \frac{A_g l_m}{2 A_m l_g} \tag{2.15}$$

$$\text{shift} = \frac{n I}{l_m} \tag{2.16}$$

We can see the influence of the magnetic circuit: if - for example - we were to increase the current going through the coil, we will shift our load-line to the right. Conversely, by applying a negative current, the load-line will shift to the left. Both n and l_m cannot be changed during operation, so they do not influence the shift of the load-line.

The slope of the load-line can be altered by changing the magnet and air-gap dimensions. Of these, only the air-gap length can feasibly be changed during actuator operation, as the others depend on physical dimensions of solid circuit components *A*, *B* and *C*. For now, we assume the air-gap to be constant, so the slope of our recoil-line can be considered predetermined and of constant value. In figure 2.7a, the load-line is visualized together with a BH-curve.

For hard permanent magnet materials such as NdFeB, the BH-curve will not appear as nonlinear as depicted in figure 2.7a. In this case, the operating point never surpasses the knee-point. For soft permanent magnets with nonlinear second quadrant BH-curves - such as AlNiCo 5 - this traditionally nondesireable behaviour is characteristic. If, for example, we apply a negative current large enough to surpass the knee-point, the sequence as seen in figure 2.7b emerges. Initially, the load-line is not shifted from the origin of the BH-axis system, and intersects the BH-curve in point *a.* This is the state of the system before any current is applied to the coil. Then, a negative current is supplied. The load-line is shifted left of the origin and we end up in point *b.* From figure 2.7b, we can see that we have clearly surpassed the knee-point - the point of irreversibility.

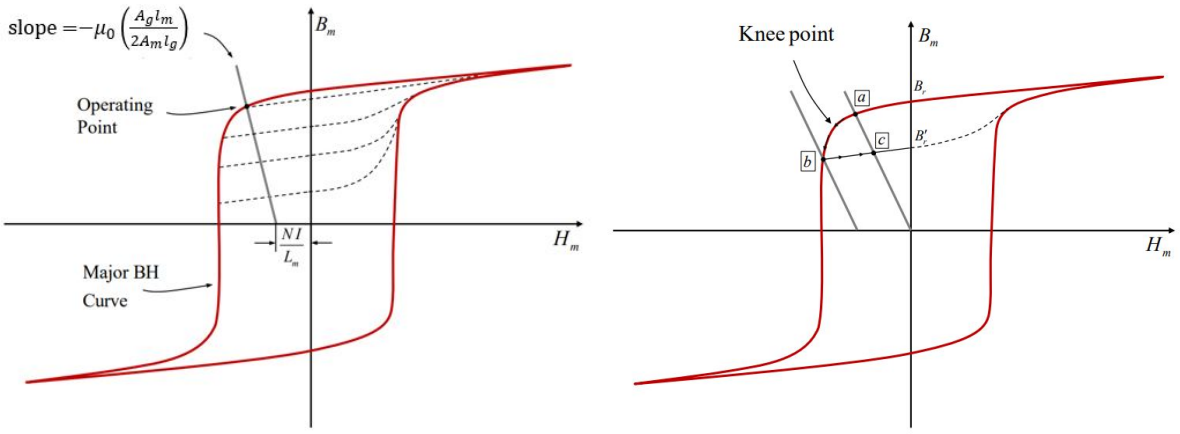

(a) Load-line and operating point

(b) Irreversible demagnetization sequence

Figure 2.7: (a): Visualization of the major BH-curve of a soft permanent magnet, together with an arbitrary load-line. Also depicted are black-dotted recoil lines and the magnet operating point. (b): Irreversible demagnetization sequence of an AlNiCo permanent magnet. From zero-state *a* to corner-point *b* when peak negative current is applied and back to new zero-state *c*. Both figures adapted from [26].

Once we let go of the current, the load-line shifts to the right, back to its original position at the origin of the BH-axis system. Only this time, the operating point has reverted along one of the recoil lines, and our operating point now lies in point *c*. In this point, magnetization B_m is less than previously in point *a*. The magnet will hold this magnetization state until we apply another current to the coil, and we end up along a different recoil line. This process of tuning a low-coercivity AlNiCo 5 magnet with a magnetizing current is called Tuneable Magnet (TM) Actuation [26].

2.3. Principles of Tuneable Magnet Actuation

This research is a continuation of the 2018 Tuneable Magnet research performed by S.G. Viëtor [26]. Up to now, the TM magnetic circuit layout was introduced and shown in figure 2.5. In this section, we state some of the advantages and possible areas of application for TM actuators. In addition, state-of-the-art research is summarized below.

2.3.1. Advantages of TM Actuator Control and Areas of Application

As established previously, high-tech machines often contain moving components that are subject to incredibly rapid and precise motions. An ASML lithography machine, for example, houses both mirror alignment systems and gravity compensators, which aim to prevent outside disturbances – such as oscillations being transmitted through the building floor. In order to ensure nanometer-precision accuracy during exposure and metrology, these vibrations must be stopped from reaching the moving parts of the wafer stage. A gravity compensator in particular must supply a relatively large constant bias force at low frequencies, which is in turn controlled by large currents, causing heat in the vacuum-chamber of the system [10].

On the other hand, satellite mirror adjustment systems in spacecraft can be tasked to hold a certain position with immaculate precision for extended amounts of time, all within a vacuum environment. A deformable space mirror developed in 2016 by TNO , for example, operates in the vacuum of space, already making it difficult to expel excess heat [14]. In addition to this, the actuators that control the mirror surface make minute adjustments, but only change their position incidentally. This means that the actuators must constantly be supplied by a controlling current and voltage, generating heat and draining the energy reserves of the satellite.

In these extreme environments, excessive heating of conventional electromagnetic actuators can cause deformations to components surrounding the coil [23] . In turn, the deformations can cause positioning errors that are too great and unpredictable to overcome with precision control or smart design, reducing the achievable performance of the precision system as a whole. This effect is especially large for systems that operate in previously mentioned extreme environments such as a vacuum, are of small scale or have to hold

a predetermined position for long periods of time - i.e. are used for quasi-static operation.

Using TM actuator control, it is proposed to replace conventional EM actuators with a low-coercivity permanent magnets - such as AlNiCo 5. From the zero-state, we can then tune the magnet to any desired value between 0 and B_r, making use of the nonlinear hysteresis and recoil line behaviour. In order to achieve this, a series of short current pulses needs to be supplied, allowing us to reach the correct operating point. After this, the magnet sustains the set magnetic field without additional tuning required - similar to the steps previously shown in figure 2.7b.

With short tuning times, we can see how this method benefits energy usage in quasi-static operation. If an actuator is used to change position only incidentally - for example at a frequency of 0.1 Hz - conventional EM actuators would require us to supply a magnetizing current at all times, changing in intensity with the change in position. As TM actuators only require the short magnetizing pulse at the start of the position change, significant efficiency gains can be obtained here.

2.3.2. State-of-the Art: Switchable Magnet Actuation by A.N. Knaian (2010)

The earliest resemblance of TM actuators can be traced back to A.N. Knaian's Electropermanent Magnet (EPM) concept [13]. The operating principle is relatively straightforward. We place a low-coercivity AlNiCo 5 (50 $kAm^{-}1$) in parallel with a high-coercivity Grae N40 NdFeB (1000 $kAm^{-}1$) magnet - with equal remanent flux densities. They are surrounded by an excitation coil, which is supplied with an electric current. The current density is too weak to cause nonlinear hysteresis behaviour in the NdFeB magnet, but large enough to saturate the AlNiCo magnet. When switched off, the magnetic flux directions of the magnets oppose each other and - because of equal remanent flux density - they cancel each other out. When the coil is activated and the circuit switched on, the AlNiCo magnet becomes saturated and both magnetic fields point in the same direction, thus creating a magnetic flux B_m that circles the magnetic circuit, as illustrated in figure 2.8.

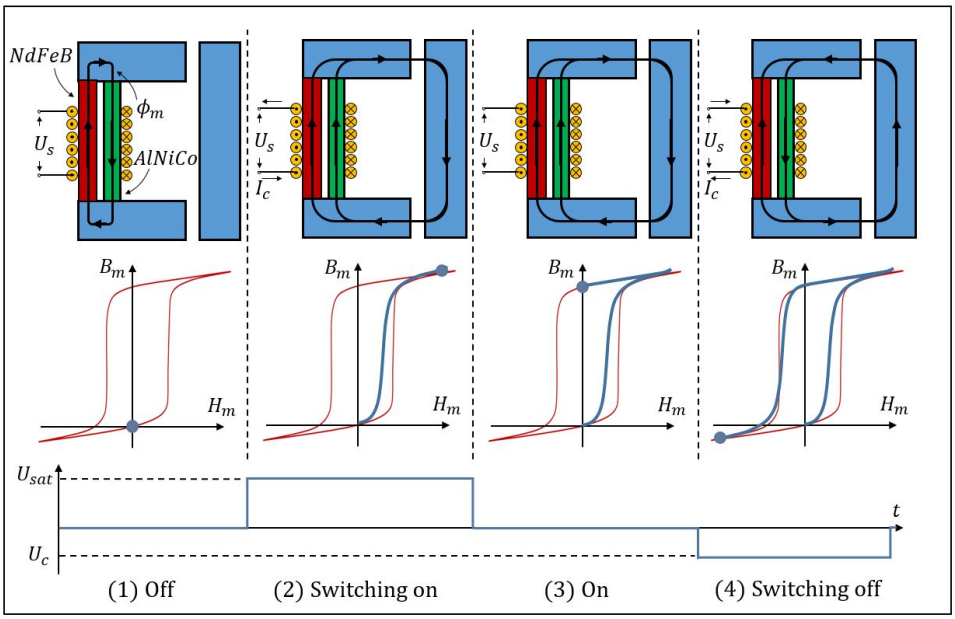

Figure 2.8: Operating sequence of an EPM actuator. During phase (1), the NdFeB and AlNiCo magnetic fields oppose each other, thus providing close to zero magnetic flux through the circuit. In (2), a saturating voltage - and thus current - is supplied to the coil, causing the AlNiCo magnet to flip direction. At time step (3), we let the current subside, causing the circuit to return to remanent flux density B_r. At last, in step (4) we apply a negative saturation current to the coil, bringing the AlNiCo magnet to the negative saturation point. Eliminating the current over the coil after this point has been reached will cause the circuit to revert to its original state of phase (1).

Instead of saturating, we can apply any amount of voltage to steps (2) and (4). This way, we can make use of the recoil line steps that were introduced in figure 2.7b to reach any remanent flux density - as long as it lies within the reach of the BH-curve. This idea was proposed by Viëtor in 2018, and is explored in the next section.

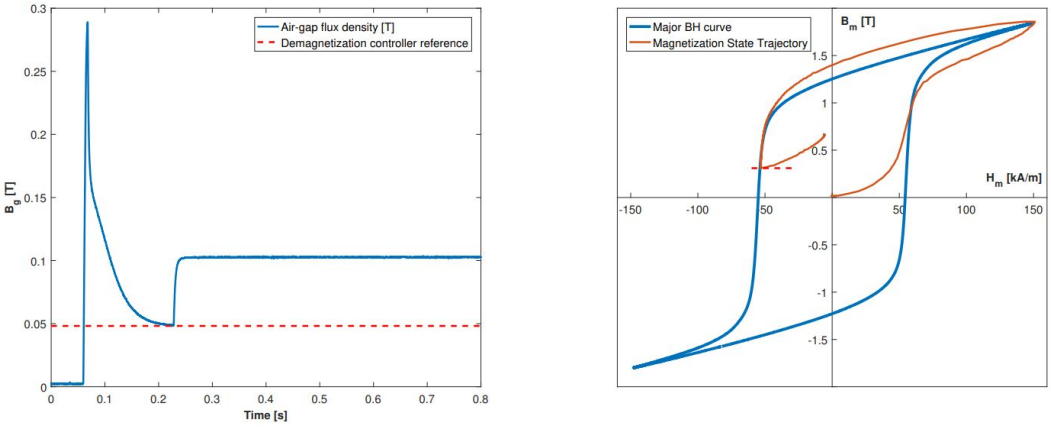

Figure 2.9: Tuning sequence for an up-step in the TM actuator, starting from the zero-state. The initial spike represents the saturation pulse, demagnetizing then occurs until the red dotted line - indicating the desired corner-point magnetization - is reached. Releasing current then causes gap flux density to increase once more to the desired value - in this case 100 mT.

2.3.3. State-of-the Art: Tuneable Magnet Actuation by S.G. Viëtor (2018)

S.G. Viëtor introduced methods to accurately tune an AlNiCo magnet to user-defined magnetization states [26]. The method provided robust tuning steps for a selection of desired gap flux densities. The three largest contributions from the work can be summarized as the development of the saturation state tuning algorithm, experimental validation on a practical setup and introduction of the Break-even Tuning Interval (BTI) metric.

In order to achieve repeatable results, the state tuning algorithm must be robust. In practice, reaching the desired gap flux density mostly comes down to correctly predicting the so-called corner point (H_c,B_c) that the controller must reach - previously illustrated as point b in figure 2.7b. Knowing the exact shape of the major BH-curve means we can make a relatively accurate prediction of the circuit operating point - given that we can correctly set up the load-line equation. To determine the slope and shift of the load-line correctly within the second quadrant, we make use of equations (2.16) and (2.15).

Entering of the second quadrant major BH-curve requires us to come down from remanent flux density B_r, which in turn warrants saturation. Therefore, the Saturation Magnetization State Tuning (SMST) method and controller were developed, with the following sequence of tuning steps: saturate → demagnetize → decay. For the demagnetization step, flux feedback control was implemented in order to determine the required coil supply voltage - U_s. The up-step trajectory is shown in figure 2.9.

An experimental setup was realized in order to validate the accuracy and repeatability of the TM control method. An overview of the setup is presented in figure 2.10a, closely resembling the circuit first introduced in figure 2.5. All components used are detailed in appendix A.

A copper wire is wound round the AlNiCo 5 permanent magnet core, serving as the magnetizing coil. The stator yoke pole pieces and mover are made of St.37 iron, and are fixed to white 3D-printed PMMA fixtures. Integrated into the circuit is an Asensor technology HE144 Hall sensor, in order to allow the user to measure the flux density (B_g) measured in the air-gap between stator and mover. The mover piece is placed on a Thorlabs manual linear stage, allowing the user to change the circuit air-gap with 10 μm resolution. Once in position, the stage cannot move, causing the dynamic effects of a moving actuator to remain unexplored.

Current is measured using a sense resistor, which measures the voltage drop over the magnetizing coil. A custom instrumentation amplifier board amplifies all sensor signals and low-pass filters them at 3 kHz in order to avoid aliasing. Sensor data is logged at 10 kHz with a dSPACE RTI1005 PPC real-time controller. The coil saturating magnetic field of 30 V and 10 A is reached by using a TI OPA549 linear-power amplifier. Dimensioning of the components and magnet characteristics are summarized in table 2.10b.

Lastly, Viëtor introduced the Break-even Tuning Interval (BTI). With this metric, the theoretical perfor-

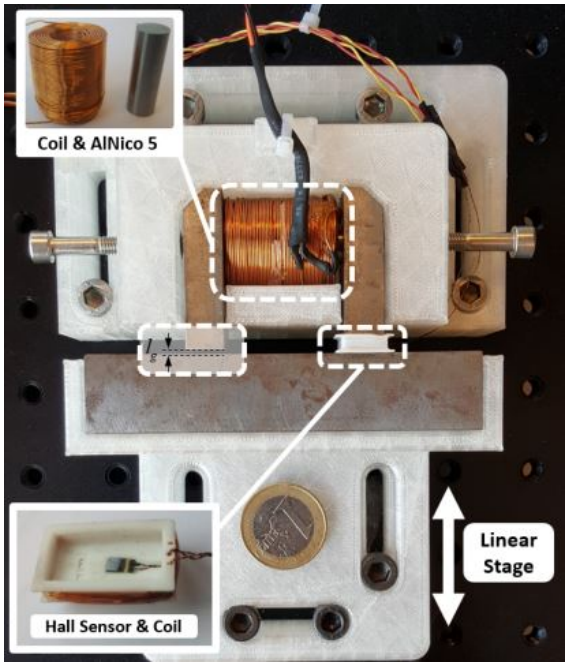

(a)

Symbol	Value	Unit	Comment	Source
AlNiCo 5 magnet (Alcomax 3 / LNG44)				
l_m	30.20	mm	Magnet length	
d_m	9.83	mm	Magnet diameter	
B_r	1.25	T	Remanent flux density	[9]
H_c	50	kAm^{-1}	Coercive force	[9]
H_{sat}	150	kAm^{-1}	Saturation field intensity	
$\mu_{r,max}$	270	-	Max. relative permeability	
ρ	$4.75 \cdot 10^{-7}$	Ωm	Electrical resistivity	[9]
Copper coil				
n	668	-	Number of coil windings	
R	3.5	Ω	Electrical resistance	
Magnetic circuit (St. 37)				
A_g	200	mm^2	Electrical resistance	
l_g	1.0	mm	Electrical resistance	
$\mu_{r,y}$	1000	-	Average relative permeability	

(b)

Figure 2.10: (a): AlNiCo 5 experimental setup. (b):Dimensions and parameters used in the TM experimental setup as introduced in 2018 by [26].

Air-gap length = 1000 μm		
$B_g[mT]$	$MAE[mT]$	$3\sigma[mT]$
175	2.87	0.42
150	2.40	0.67
125	2.52	0.61
100	2.86	1.07
75	3.12	1.17
50	3.16	1.08
25	2.88	1.12
0	2.59	1.08

(a)

Air-gap length = 1500 μm		
$B_g[mT]$	$MAE[mT]$	$3\sigma[mT]$
175	25.35	0.49
150	11.86	0.29
125	8.19	0.35
100	7.61	0.36
75	7.91	0.37
50	8.34	0.35
25	8.89	0.31
0	9.85	0.36

(b)

Figure 2.11: (a): Tuning performance achieved by [26] for 1000 μm air-gap length. (b):Tuning performance achieved by [26] for 1500 μm air-gap length.

mance of both a TM and EM actuator is compared, resulting in a figure that shows the amount of time that needs to elapse in the actuated state in order for the TM actuator to be more efficient. This calculation has only been performed theoretically, so practical results still need to be obtained for this. This metric will be explored more thoroughly in 4. The obtained MAE tuning accuracy and 3σ repeatability results for 1000 and 1500 μm air-gap lengths have been concatenated in tables 2.11a and 2.11b [26].

3

Tunable Magnets: Design and Control of a Gap-closing Reluctance Actuator

Using Dynamic Flux-feedback Compensation Methods

Tunable Magnets: Design and Control of a Gap-closing Reluctance Actuator

Using Dynamic Flux-feedback Compensation Methods

1 Introduction

In precision engineering, thermal stability is of great importance in order to keep up with the ever-increasing demand for faster and more precise positioning actuators. Most notably, actuator magnetizing coils dissipate heat to surrounding machine components as a result of Joule heating. With changing temperatures, system components expand and contract - causing unwanted structural deformations that can lead to a decline in positioning accuracy and repeatability [1, 2].

Traditionally, Lorentz actuators were favored for high-precision applications, due to their inherently linear force-current relationship - making them highly predictable [3]. This type of actuator, however, is also characterized by a low force density - which results in relatively poor efficiency [4]. In recent years, the control predictibility of modern reluctance actuators has improved significantly – allowing for up to 10 times larger force-density when compared to Lorentz actuators [4]. Larger force-density greatly reduces the actuator size and thus magnetizing current required for positioning, which in turn improves energy efficiency [5].

Still, the effect of Joule heating within EM reluctance actuators remains especially pronounced during quasi-static operation, where the magnetizing current of the EM actuator must be sustained for extended periods of time. Additionally, many high–precision systems operate within challenging conditions - often requiring large bias forces in a vacuum environment - making it difficult to expel the generated heat.

1.1 Prior art

Prior research has attempted to find methods that improve actuator efficiency for quasi-static operation. Typically, the methods propose a variation of a hybrid reluctance actuator topology to improve this. A.N. Knaian was first to introduce the concept of in-situ magnetization adjustment of AlNiCo, with the switchable Electropermanent Magnet (EMP) actuator [6]. A soft AlNiCo magnet is placed in parallel with a hard NdFeB magnet - both surrounded by a single magnetizing coil. The AlNiCo magnet can be more easily (de-) magnetized when compared to hard NdFeB magnets typically found in hybrid reluctance actuators [7–9]. This way, by switching the magnet to the 'on'-state with a single current pulse, the magnet sustains the magnetization state after tuning - even after all current has subsided. During stationary periods, little to no additional energy loss is expected, which makes this method especially efficient for quasi-static operation.

In 2018, S.G. Viëtor introduced a method to accurately tune an AlNiCo magnet to a set of user-predefined magnetization states [10]. Contrary to Knaian's 'on'- and 'off'-state, this novel method allows for a selection of intermediate states - allowing the user to set the circuit air-gap flux density level with 25 mT increments. The three largest contributions from the work can be summarized as the development of the novel Saturation Magnetization State Tuning (SMST) algorithm, experimental validation of TM performance on a practical static-gap setup and introduction of the Break-even Tuning Interval (BTI) metric - which allows for an efficiency comparison between novel TM and conventional EM actuators.

1.2 Research contributions

This research is a continuation of Viëtor's work, and part of an ongoing research program investigating the application of in-situ magnetization adjustment of AlNiCo magnets. While the work performed prior to this research establishes the robust SMST method of TM control, it is not yet mature enough to be implemented in practice. Part of the limitations originate from the setup used - which only allows a change of the air-gap length inbetween tuning cycles. During each cycle, the gap length is fixed. In order to represent proper actuator dynamics, the setup must be expanded in order to allow for these movements to occur during the tuning cycle.

Furthermore, the SMST experimental results display excellent accuracy and repeatability for a known air-gap length of 1 mm. However, an air-gap of 1.5 mm already causes these performance metrics to worsen - even with a static air-gap during the tuning process. It is believed that these discrepancies originate from improper corner-point predictions of the tuning algorithm - due to changes in the circuit air-gap length. If these complications are not properly accounted for, we obtain the wrong the corner-point estimation - translating to a reduction in accuracy and thus increase in MAE. For this reason, increased variable-gap

robustness and prediction accuracy is required in order to make the TM method suitable for dynamic operation.

In this paper, the existing setup will be expanded with a modular subassembly that allows for experimentation under changing air-gap conditions. This will allow the user to investigate dynamic effects of different tuning methods and unlocks validation of the BTI metric. Furthermore, we increase robustness and performance of the magnetization state tuning algorithm. This will be achieved by using a series of analytically derived compensators combined with feedback control, which allows for more precise magnetization state tuning - even for extreme and dynamically changing air-gap lengths.

2 Dynamic Tunable Magnet Actuator Control

In this section, we shortly elaborate the operating principle of TM actuators. For a more detailed explanation of permanent magnetism (PM) principles and magnetic circuit properties, it is recommended to consult the preliminary knowledge provided in the previous chapter.

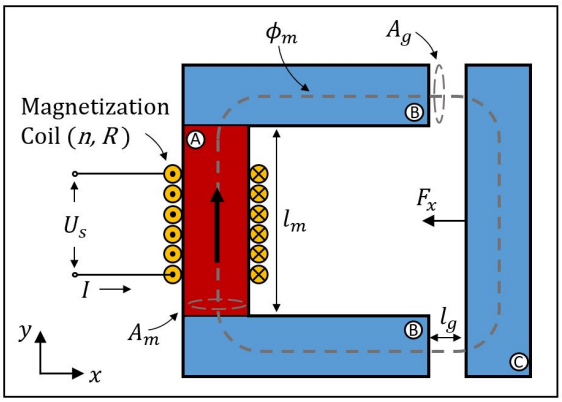

Fig. 1. Typical layout of a gap-closing electromagnetic reluctance actuator. Component A can be a permanent magnet (hybrid actuator) or ferromagnetic yoke, and is excited by the magnetization coil with n turns and R resistance. Components B make up the ferromagnetic stator yoke. Component C is free-moving and of the same ferromagnetic material as B, closing and opening l_g as it moves from left to right. Magnetic flux is indicated with ϕ_m and moves in clockwise direction.

In this research, a conventional C-shaped gap-closing reluctance actuator topology is studied, as shown in figure 1. Within TM actuators, component A consists of a low-coercivity AlNiCo 5 magnet [10]. Circuit dimensions A_g, A_m and l_m are predetermined and constant, whereas l_g can extend and contract in the direction of the arrows. For now, we assume l_g to be constant. Furthermore, supply voltage U_s can be controlled, causing a magnetizing current I over the coil.

2.1 Modelling of Magnetic Circuit

Within the circuit, we can be distinguish both a magnetic and electric subsystem. We consider first the behaviour of the permanent magnet and how it determines what happens in the circuit as a whole. After this, the electrical circuit - consisting of a power supply and the magnetizing coil - can be taken into consideration.

2.1.1 Permanent Magnet and Circuit Modelling

As mentioned before, the PM used in this particular circuit consists of AlNiCo 5 soft magnetic material. This type of magnet is distinguished by its high remanent flux density - B_r - and low coercivity - H_c. This makes it relatively easy to (de-)magnetize when compared to hard NdFeB magnets, while still being able to provide ample magnetic flux density. We remember from the preliminary that this relationship between magnet flux density B_m and the applied coil magnetic field H_m can be captured using a BH-hysteresis curve [7, 8]. Additionally, the influence of circuit dimensions and material properties yields the so-called load-line of the system, characterized by equation (1):

$$B_m = -\mu_0 \cdot \frac{A_g l_m}{2 A_m l_g} \cdot \left(H_m - \frac{nI}{l_m} \right) \tag{1}$$

A derivation of equation (1) can be found in the preliminary. The equation assumes an ideal magnetic circuit without flux losses. In practice, losses can occur both at the fringes of the air-gap and within other circuit components. Respectively, these can be described by the flux leakage coefficient - k_1 - and MMF loss factor - k_2. For now, these can be assumed to be of constant value, and are determined by using:

$$k_1 = \frac{\phi_m}{\phi_g} = \frac{A_m B_m}{A_g B_g} \tag{2}$$

$$k_2 = \frac{MMF_m}{MMF_g} = \frac{H_m l_m}{2 H_g l_g} \tag{3}$$

Incorporating these factors into equation (1) yields the loss-corrected load-line equation:

$$B_m = -\mu_0 \cdot \frac{k_1}{k_2} \frac{A_g l_m}{2 A_m l_g} \cdot \left(H_m - \frac{nI}{l_m} \right) \tag{4}$$

Breaking the equation down once more to find the load-line slope and shift along the H_m-axis yields equations (5) and (6):

$$\text{slope} = -\mu_0 \cdot \frac{k_1}{k_2} \frac{A_g l_m}{2 A_m l_g} \tag{5}$$

$$\text{shift} = \frac{nI}{l_m} \tag{6}$$

Figure 2 captures both the major AlNiCo 5 BH-curve, together with an arbitrary load-line. Additionally, the operating point and recoil lines are shown. In practice, the recoil lines span a continuous field, enclosed by the BH-curve - The importance of which is discussed in section 2.2.2.

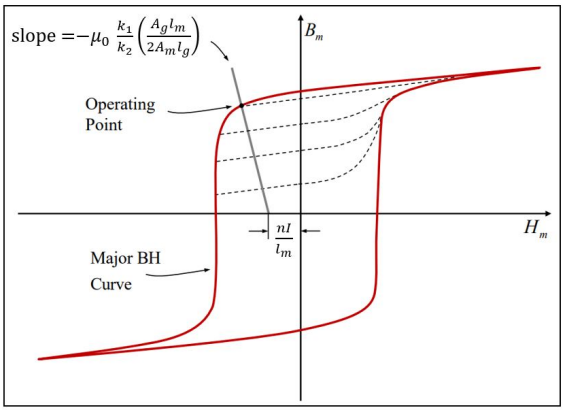

Fig. 2. Visualization of the major BH-curve of a soft permanent magnet, together with an arbitrary load-line. Also depicted are black-dotted recoil lines and the magnet operating point. Adapted from [10].

2.1.2 Electric Circuit Modelling

The model can be extended by also considering the electric circuit. In essence, it consists of only a voltage supply and magnetizing coil. Taking into account the coil resistance, the equivalent electric circuit can be modelled by placing said resistance in series with the other components, as demonstrated by figure 3.

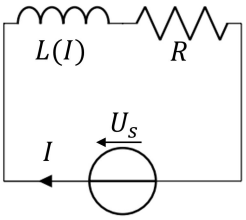

Fig. 3. Equivalent electric circuit of the magnetizing coil surrounding the AlNiCo 5 magnet, in conjunction with the voltage source.

The inductance of the coil is dependent on the level of magnetization of the AlNiCo magnet, and therefore on the supplied current I. Because both components act in series, the supply voltage can be analytically determined by using:

$$U_s = IR + A_m n \frac{dB_m}{dt} \tag{7}$$

2.2 Saturation Magnetization State Tuning Method

For low-coercivity PM materials such as AlNiCo 5, the second quadrant - in which the circuit usually operates - becomes nonlinear. On the major BH-curve, this feature is reflected by the knee-point - which indicates the point of irreversibility. This feature is illustrated in figure 4: surpassing this point starting from zero-state *a*, we can apply a demagnetizing current to the coil. As we learned in section 2.1.1, this causes the load-line of the circuit to shift towards the left. In turn, the intersection between the load-line and BH-curve also shifts, until corner-point *b* is reached. If we subsequently let go of the current, we no longer move along the major BH-curve. Instead, we follow one of the recoil lines and end up in the new zero-state *c*. This sequence of events describes a demagnetization step of the permanent magnet, making it possible to tune the circuit to any desired magnetization state with one short sequence of tuning steps. After this, the magnet sustains the magnetic field until the user decides re-tuning is desired. This nonlinearity has been used by [10] to develop the Saturation Magnetization State Tuning (SMST) method, controlling the TM actuator. The method can be subdivided into three stages: saturation, demagnetization and decay, which are also shown in figure 5.

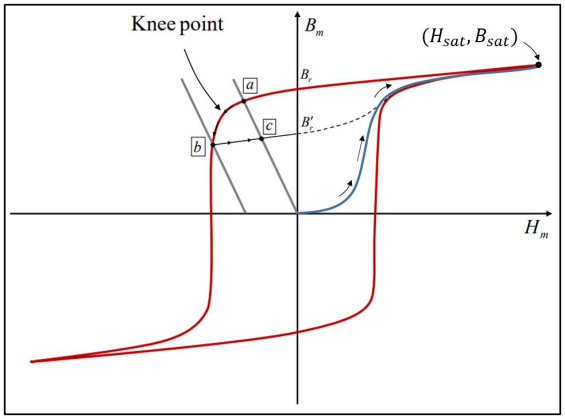

Fig. 4. Irreversible demagnetization sequence of an AlNiCo permanent magnet. From zero-state [a] to corner-point [b] and back to the new zero-state [c]. Also in blue: the *virgin magnetization curve*.

2.2.1 Saturation

Using a saturation step simplifies the tuning sequence: this way, the circuit will always traverse the major BH-curve within the second quadrant. In order to tune the entire system, only the major BH-curve needs to be experimentally validated, instead of a multitude of minor hysteresis loops. At saturation, H_m and B_m reach H_{sat} and B_{sat} respectively, which means we can rewrite equation (4). Substituting H_m with H_{sat} and B_m with $B_{sat} = B_r + \mu_0 H_{sat}$, yielding:

$$I_{sat} = \frac{l_m}{n}\left[H_{sat} + 2\left(\frac{k_2}{k_1}\right)\cdot\left(\frac{B_r}{\mu_0} + H_{sat}\right)\cdot\frac{A_m l_g}{A_g l_m}\right] \tag{8}$$

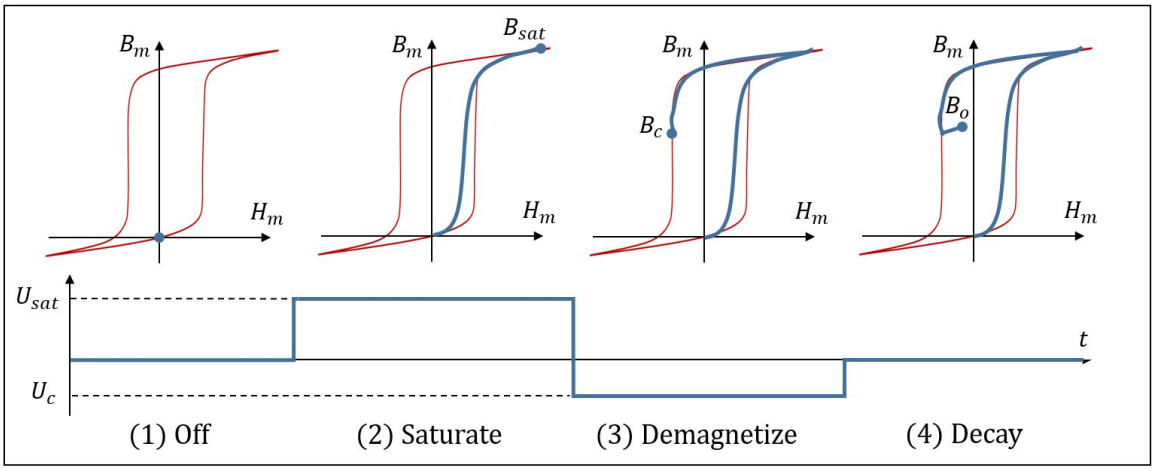

Fig. 5. Sequencing of the four-step SMST tuning method. After saturation (2), the corner-point is reached by demagnetizing the AlNiCo magnet (3). Because of irreversibility, we revert along one of the recoil lines towards the new operating point - B_o.

Saturation from (H_m,B_m) = (0,0) is represented by step 2 in figure 5. For long saturation times, with t_{tune} in the order of 100 *ms* or larger, the contribution of circuit self-inductance as shown before in equation 7 is orders of magnitude smaller than Ohmic losses. For these time-scales, the required saturation voltage can simply be determined by using Ohm's law, simplifying equation 7 to:

$$U_{sat} = I_{sat} R \tag{9}$$

For very fast saturation times in the order of 10 *ms*, the inductance contribution becomes too large to ignore, and additional supply voltage must be attributed in order to guarantee that the magnet reaches saturation. Within this research, longer tuning times are used - allowing for the above simplification.

2.2.2 Demagnetization and Decay

In order to reach the desired gap magnetization, we must apply a demagnetizing current after saturation. For this, accurate corner-point prediction is imperative. In figure 5, this demagnetization process is described by step 3: starting from saturation point (H_{sat}, B_{sat}), we traverse the major BH-curve in an anticlockwise manner until corner-point (H_c, B_c) is reached. After this, the demagnetizing current subsides to zero during the decay phase and the magnet moves back to the desired operating point (H_o, B_o) - denoted in figure 5 as step 4. A detailed view of the second quadrant is provided in figure 6 with a highlighted corner-point prediction for $B_g = 75mT$. The final objective here is to find the intersection between our recoil-line and the BH-curve - (H_c, B_c) - and use this for our demagnetizing controller.

We notice from figure 6 that the second quadrant of the BH-curve can largely be linearized - as indicated by the green line and expressed by equation (10). This simplifies the corner-point prediction by not requiring large datasets for experimentally validated major BH-curve trajectories, which in turn saves on computation time.

$$B_{max}(H_m) = \mu_0 \mu_{max} \cdot (H_m + H_{c,i}) \tag{10}$$

In equation (10), $\mu_0 \mu_{max}$ indicates the slope of the line, with $\mu_{max} = 270$ as experimentally validated by [10]. Additionally, $H_{c,i}$ can be recognized as a H_m-axis translation in order to align the linearized approximation with the coercivity of the major BH-curve. Similarly, we can express the recoil line as:

$$B_{rec}(H_m) = \mu_0 \mu_{rec} H_m + B'_r \tag{11}$$

With $\mu_0 \mu_{rec}$ as the slope of the recoil line and B'_r as recoil line B_m-axis translation, which translates to the setpoint remanent flux density of our chosen operating point. For AlNiCo 5, μ_{rec} can for now be assumed to be of constant value: $\mu_{rec} \approx 5.50$. B'_r can in turn be related to B_o by realizing that:

$$B'_r = B_o - \mu_0 \mu_{rec} H_o \tag{12}$$

We can then link the magnet operating point B_o to gap flux density B_g by using *Gauss's law* for the conservation of magnetic flux [7, 8]:

$$B_o A_m = B_g A_g \tag{13}$$

We also remember from the preliminary that $B_g = \mu_0 H_g$. Combining this with equations (2), (3) and (13) yields expressions for both H_o and B_o - only depending on the user-defined air-gap flux density B_g:

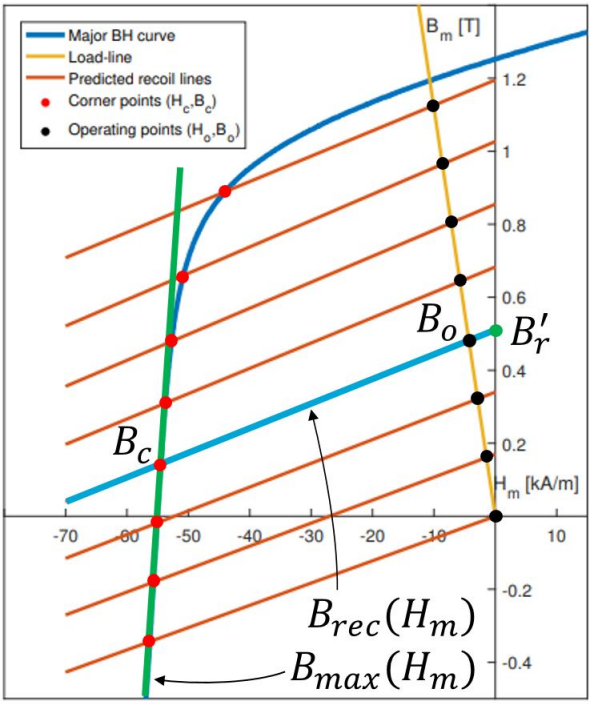

Fig. 6. Detailed view of the second quadrant. Highlighted is the desired corner-point B_c, which is characterized as the intersection between the recoil line and major BH-curve. Finding this point yields the desired operating point B_o - and thus gap flux density B_g.

$$\begin{cases} H_o = -\frac{2k_2 l_g}{l_m} \cdot \frac{B_g}{\mu_0} \\ B_o = \frac{k_1 A_g}{A_m} \cdot B_g \end{cases} \tag{14}$$

In order to complete the corner-point prediction, we equate (11) and (10). Rewriting to solve for H_c, we obtain:

$$H_c = \frac{B'_r - \mu_0 \mu_{max} H_{c,i}}{\mu_0 \cdot (\mu_{max} - \mu_{rec})} \tag{15}$$

We can now relate the desired corner-point magnetization B_c with the result of equation (15) by using:

$$B_c = \mu_0 \mu_{rec} H_c \tag{16}$$

Which - after substitution with equation (15) - finally yields an expression for the desired corner-point flux density:

$$B_c = \frac{B'_r + \mu_0 \mu_{max} H_c}{\left(\frac{\mu_{max}}{\mu_{rec}}\right) - 1} + B'_r \tag{17}$$

We use the corner-point prediction for our demagnetization controller, which will be explored in the next section.

2.2.3 Controller implementation

In order to use the TM actuator in practice, we require a robust controller that can use the analytical corner-point predictions to tune the setup to the desired magnetization state. Among other methods of control - such as feedforward and PID feedback control - the inverted flux feedback controller constructed in previous work by [10] offers a robust tuning method that remains relatively easy to implement. In order to find the inverted controller, we must first find the transfer function of our plant.

Figure 7 shows a block-diagram overview of the magnetic control circuit. Starting at the input, the user provides the desired air-gap flux density $B_{g,set}$. This gets converted by corner-point equations (12), (14) and (17) into a prediction of the desired corner-point (H_c, B_c). Flux feedback is measured at the air-gap, as will be later elaborated in section 4. Therefore, the magnet corner-point prediction must be converted to the desired corner-point gap flux density value $B_{c,g}$ - which is then compared to the measured value of B_g, resulting in an error in flux density B_e. This is then fed to the controller, which processes the error to the required coil demagnetizing voltage U_s. Because of this voltage, the AlNiCo 5 magnetization level B_m changes - which in turn causes the measured gap flux density B_g to vary. In dynamic operation, the plant is subjected to two major disturbances: a change in air-gap length l_g and corresponding fringe flux loss factor k_1. Considering static-gap operation means that for now, these disturbances are assumed to have no influence.

We can see that the transfer function of the plant is determined by input voltage U_s and output magnet flux density B_m. By combining equations (4) and (7) and rewriting for U_s, we can find a differential equation that describes the tuning voltage required for reaching the desired corner-point [10]:

$$U_s = B_m A_m \left[\frac{R}{n} \left(\frac{k_2}{k_1} \frac{2l_g}{\mu_0 A_g} + \frac{l_m}{A_m \mu_0 \mu_r} \right) + n \frac{dB_m}{dt} \right] \tag{18}$$

Taking the Laplace transform of equation (18) directly yields the plant transfer function $G(s)$, which can be written as:

$$G(s) = \frac{B_m(s)}{U_s(s)} = G_0 \frac{1}{\frac{L}{R}s + 1} \tag{19}$$

Where G_0 represents the system DC gain and L the linearized coil inductance, given respectively by:

$$G_0 = \frac{\frac{n}{A_m}}{R\left(\frac{k_2}{k_1} \frac{2l_g}{\mu_0 A_g} + \frac{l_m}{A_m \mu_0 \mu_r} \right)} \tag{20}$$

$$L = N^2 \left[\left(\frac{k_1}{k_2} \frac{A_g \mu_0}{2l_g} \right) + \left(\frac{A_m \mu_0 \mu_r}{l_m} \right) \right] \tag{21}$$

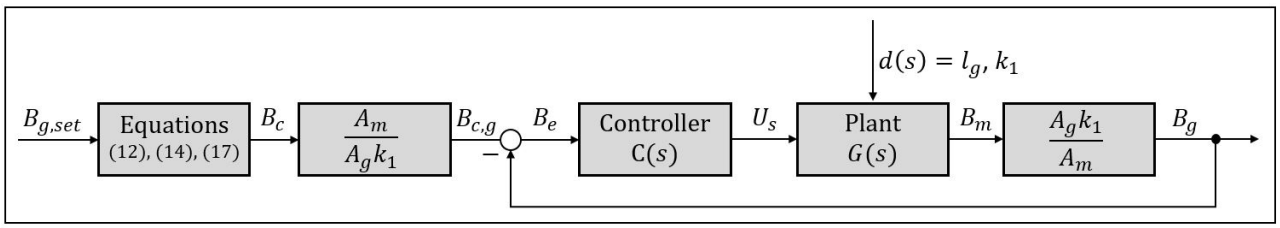

Fig. 7. Overview of the TM actuator control schematic. The gap flux density setpoint is first translated to the corresponding magnet corner-point. This can then be written as a corner-point gap flux density - which is compared in real-time with the measured gap flux-density using feedback control. This error is fed to the controller, which establishes the supply voltage required.

Using inverse control, the total loop transfer function can be written as:

$$L(s) = G(s)C(s) = \frac{\omega_c}{s} \tag{22}$$

Where ω_c describes the controller bandwidth. Controller parameters are summarized in table 1. Because of the irreversible nature of magnetization state-tuning, the controller is tuned to the worst possible tuning case, in which G_0 and L values are maximized. This way, the controller is stabilized in order to ensure zero overshoot in the step response.

Table 1. Controller parameters overview, adapted from [10]

Parameter	Value	Description
ω_c	550 $rads^{-1}$	Control bandwidth, [10]
$G_{0,max}$	0.268 TV^{-1}	Max. plant DC-gain
$L_{max}r$	48.6 mH	Max. coil inductance
R	3.5 Ω	Measured coil resistance

Using the parameters detailed in table 1, substituting equation (19) into (22) and rewriting to solve for $C(s)$, we obtain the stabilized inverted controller:

$$C(s) = \frac{\omega_c}{s} G_{0,max} \left(\frac{L_{max}}{R} s + 1 \right) \tag{23}$$

Controller step response characteristics and detailed design can be found in [10], experimental results are further elaborated in sections 4 and 5.

3 Dynamic flux-feedback compensation methods

The control scheme implemented by [10] is capable of providing accurate and repeatable results when used in conjunction with the SMST-method - as evidenced by the results shown in the preliminary. Performance, however, proved to be highly dependent on the magnetization setpoint and air-gap length: for larger air-gaps, accuracy would quickly deteriorate [10]. This can be traced back to the disturbance assumption made earlier in section 2.2.3: in his research, Viëtor performed measurements at different but constant air-gap lengths, and thus could assume l_g and k_1 to remain constant during the tuning cycle. However, equation (17) suggests that proper corner-point prediction is highly dependent on using accurate representations of variables μ_r, l_g and k_1. Therefore, four compensation methods are introduced that aim to improve controller accuracy, repeatability and robustness for a broad range of (quasi-) static and dynamic operation conditions.

Dynamic Recoil-line Slope compensation (DRS) aims to enhance corner-point estimation by accounting for continuous non-constant recoil line slopes. Dynamic Air-gap (DA) and Fringe-flux Loss (FL) compensation use real-time air-gap length measurements and enhanced k_1 estimation to improve corner-point and controller gain predictions. Lastly, Parallel PI (PPI) flux-feedback control aims to reduce steady-state B_g control errors.

3.1 Dynamic Recoil-line Slope Compensation

In section 2.2.2, we assumed the recoil-line slope to be of constant value - at $\mu_{rec} \approx 5.50$. In practice, this value is only corresponds to a remanent flux density of $B'_r \approx 0.68T$ - the recoil line slope steepens for larger B'_r values, and flattens for lower B'_r. This can cause an error in corner-point prediction, which in turn negatively impacts the accuracy of the obtained gap magnetic flux density. The discrepancy was also recognized by [10]. In the research, the relationship between the second-quadrant recoil-line slope μ_{rec} and remanent flux density B'_r was characterized by a 10th order polynomial, as shown in figure 8.

In prior work, the correct recoil-line slope was selected by using lookup table 2. In essence, the table relates the desired air-gap flux density $B_{g,set}$ with the required corner-point flux density B_c and recoil line slope μ_{rec}. Unfortunately, this requires the user to manually search the look-up table and provide the controller with the corner-point corresponding to the desired air-gap flux sensity. Furthermore, this method is limited to the setpoints for which these relationships are experimentally determined - with increments of 25 mT. The efforts of analytically determining the corner-point - as derived in section 2.2.2 - overcome this issue and allow for any air-gap flux density to be selected. Therefore, it makes sense to also use a continuous recoil line slope equation, instead of the lookup-table format used before.

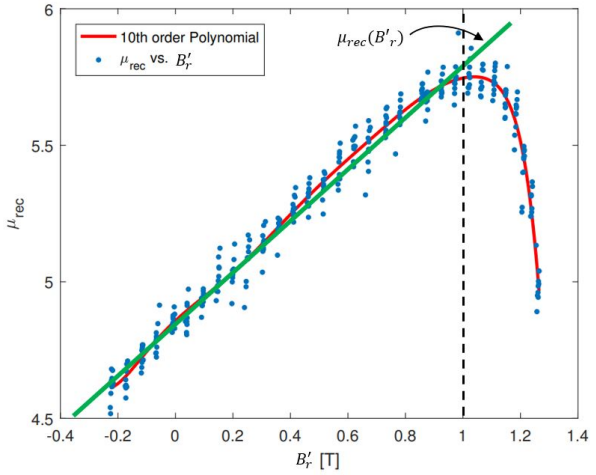

Fig. 8. Nonlinear recoil-line slope relationship approximated with a 10^{th} order polynomial, adapted from [10].

Table 2. Recoil-line slope incremental lookup table, adapted from [10]

$B_g[T]$	$B_c[T]$	$\mu_{rec}[-]$	$B'_r[T]$
0.175	0.889	5.537	1.195
0.150	0.659	5.750	1.027
0.125	0.479	5.674	0.855
0.100	0.310	5.526	0.683
0.075	0.144	5.363	0.511
0.050	-0.018	5.180	0.340
0.025	-0.181	5.006	0.170
0.000	-0.343	4.857	0.000

As shown in figure 8, the recoil-line slope can be approached by linearizing the 10th order polynomial in the range $0\ T \leq B'_r \leq 1\ T$, as also reflected by table 2. Linearizing the recoil line slope yields the equation:

$$\begin{cases} \mu_{rec} = 0.955B'_r + 4.69 \\ \text{for:} \quad 0 \leq B'_r \leq 1 \end{cases} \tag{24}$$

This compensation factor can be easily applied to the corner-point calculations of section 2.2.2, by substituting equation (24) back into equation (11), which after rewriting now yields:

$$B'_r = \frac{B_o - 4.69H_o\mu_0}{1 + 0.955H_o\mu_0} \tag{25}$$

This value for B'_r can then be used to determine the correct recoil line slope, using equation (24). Finally, this allows us to determine the corner-point (H_c, B_c) with equations (15) and (17), taking into account a non-constant recoil line slope. Experimental validation of DRS performance is summarized in sections 4 and 5.

3.2 Dynamic Air-gap compensation

In a gap-closing reluctance actuator circuit, most of the circuit dimensions are predetermined and of constant value. Examples of this are the length of the permanent magnet, area of the air-gap and amount of coil windings (respectively - l_m, A_g and n). Air-gap length l_g, however, changes in practice when air-gap magnetization B_g is altered: an increase in B_g causes an increased attraction force between the stator and mover. Even if we assume the air-gap length to be static, it can be seen from equations (14), (20) and (21) that choosing a slightly different air-gap length - e.g. 1.5 *mm* instead of 1 *mm* - can cause a discrepancy in both corner-point and demagnetizing voltage predictions. This was evidenced by the results obtained by [10], as shown in chapter 2.
A change in air-gap length namely causes the load-line slope to change as well - in accordance with equation (5). This in turn means that the intersection between the load-line and major BH-curve changes, causing a shift in remanent flux density $\Delta B'_r$, as illustrated in figure 9. Resulting from this, the prediction of corner-point flux density B_c will start to overshoot for larger air-gaps, causing the steady-state error to increase.

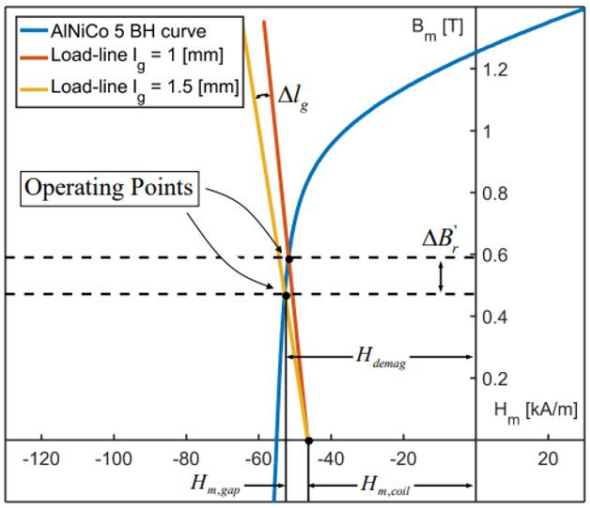

Fig. 9. Change in load-line slope as a result of changing air-gap length, adapted from [10]

The influence of changing air-gap length is, however, two-fold. Not only does it influence the corner-point prediction, but it also influences the initial estimate of demagnetizing voltage that will be supplied by the controller. This is illustrated by equations (20) and (21). An increase in air-gap length causes both the plant DC-gain and inductance estimate to decrease, which in turn means that the demagnetizing voltage error increases - slowing down the tuning sequence. This phenomenon can be compensated by measuring l_g in real-time, and feeding back these measurements into B_c and U_s calculations. How this measurement is achieved and what changes in performance is demonstrated in sections 4 and 5.

3.3 Fringe Flux-loss compensation

Similar to the dynamically changing l_g, flux leakage coefficient k_1 and magnetomotive force loss factor k_2 also change with the magnetic circuit dimensions. Similarly, they both influence the corner-point and demagnetizing voltage predictions - in accordance with equations (16), (20) and (21).

Up to now, loss factors k_1 and k_2 were assumed to be of constant values: 2.44 and 1.09 respectively. Sensitivity analysis using COMSOL simulation suggests that both loss factors are relatively insensitive to most changes in circuit parameters, except for air-gap length [10]. The same analysis suggests, however, that k_1 is very sensitive to a change in air-gap length, and cannot be assumed constant, whereas loss factor k_2 only appears to be sensitive to this for very small l_g values - which exist outside of the movement range studied in this research. Within the movement range, k_2 sensitivity never deviates more than $\pm 2\%$ from the assumed value, and will therefore - unlike k_1 - still be regarded as a constant loss factor of value 1.09 [10]. The sensitivity of k_1 is illustrated in figure 10.

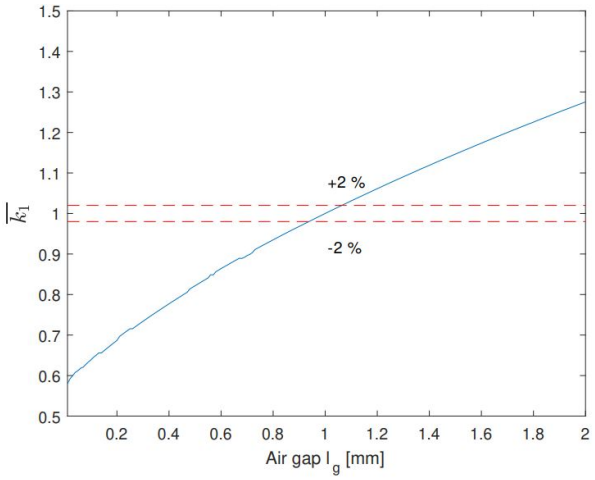

Fig. 10. COMSOL sensitivity of flux leakage coefficient k_1 for changing air-gap length l_g, adapted from [10].

Using the sensitivity of k_1 to l_g, we can write k_1 by using an emperically approximated quadratic equation:

$$k_1 = 2.44 \cdot (-6.79 \cdot 10^4 l_g^2 + 4.76 \cdot 10^2 l_g + 0.59) \qquad (26)$$

Substituting the quadratic approximation of k_1 into equations (16), (20) and (21) using the fed-back l_g measurements, a more accurate estimation can be performed for a wider range of changing air-gap lengths.

3.4 Parallel PI flux-feedback control

Up to this point, only inverse flux feedback control has been considered as a demagnetizing strategy. While the method is - in theory - capable of slowly approaching the predicted corner-point, any errors in this prediction will yield a constant steady-state error due to the absence of a control integrator. In PI control, the integrator allows for faster rise times and a reduction in steady state error [5]. Adding this type of control in parallel to the inverse controller - while using the same flux feedback mechanism as before - could potentially iron out some of the remaining steady-state error in gap flux density B_g. This way, the control schematic can now be described by figure 11.

The transfer function of the parallel PI flux feedback controller can be described by:

$$C_{PI}(s) = k_p + \frac{k_i}{s} \qquad (27)$$

After experimenting with the controller, a balanced controller setup that provided adequate performance and stability was found, yielding $k_p = 0.05$ and $k_i = \frac{k_p}{7}$ - following from the rules of thumb proposed by [5].

4 Static-gap experimental validation of compensation method performance

In this research, four methods of disturbance compensation are identified in both static- and dynamic-gap operation. For tuning performance, we consider Mean Average Error (*MAE*) accuracy and 3σ repeatability. Static air-gap performance of each of the compensation methods is detailed in this section, whereas dynamic performance is evaluated in section 5. First, we introduce the static air-gap setup used for the experiments.

4.1 Static air-gap experimental setup overview

The largest part of the static air-gap experimental setup shown in figure 12 was previously built by [10]. The entire setup is mounted to a Thorlabs optical breadboard [11]. The mover yoke is glued into to a 3D-printed PMMA bracket which in turn is bolted on a Thorlabs manual linear stage, allowing the user to precisely vary the air-gap length inbetween experiments [12]. During a tuning cycle, however, the stage does not move, keeping the air-gap at a constant value. Added for this research is a Micro Epsilon OptoNCDT laser triangulation distance sensor, with a motion range of 10 *mm* and resolution of 0.5 μm - measuring variations in air-gap length l_g [13]. The sensor is mounted on a sturdy aluminium bracket, suspended above the moving stage. Two slots milled from the base of the brackets allow for coarse alignment of the distance sensor respective to the moving stage. Gap magnetic flux density B_g is measured using an Asensor Technology HE144 hall sensor, details of which are provided in appendix C. The sensor is placed within a 3D-printed PMMA

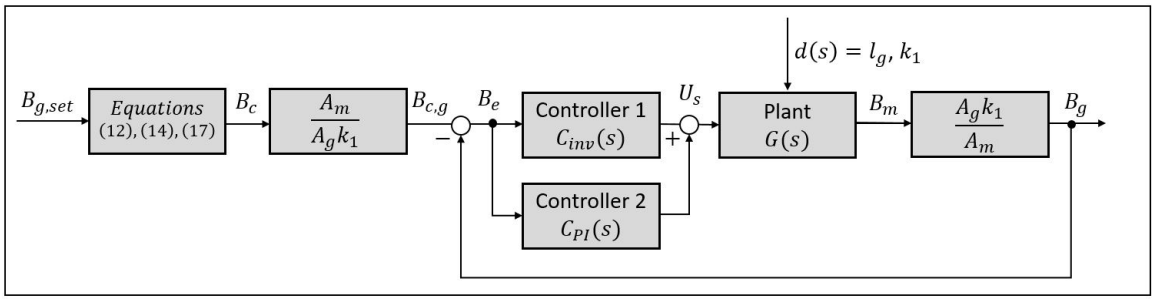

Fig. 11. Adding PPI flux-feedback control does not change much in terms of the control schematic. It appears - as the name suggests - in parallel with the original inverted controller.

fixture, and can be slid over one of the machined St. 37 stator pole pieces. The thickness of the fixture was determined to be approximately 935 μm, which limits gap measurements to values larger than this.

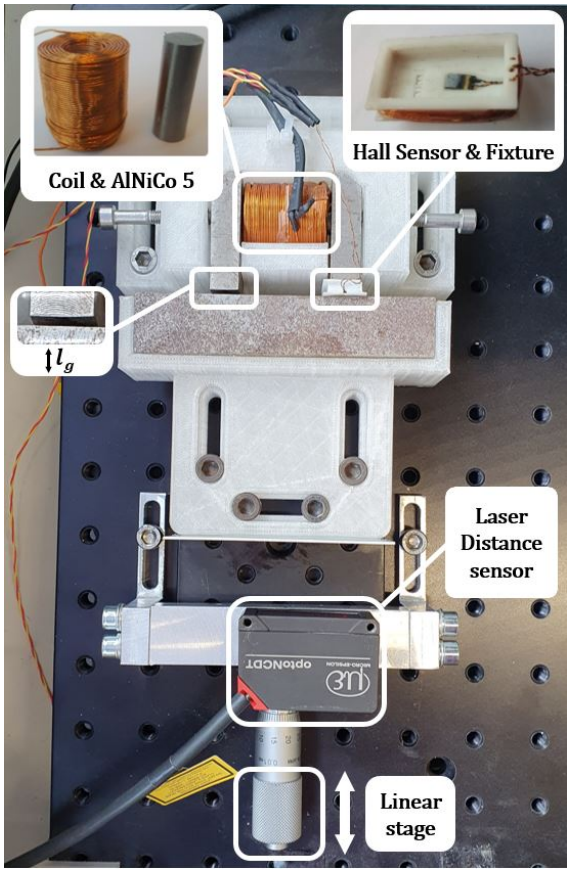

Fig. 12. Overview of the pre-existing static-gap experimental setup. Added are the laser triangulation distance sensor and its mounting bracket.

The AlNiCo 5 PM material is clamped between the two pole pieces, and is surrounded by the copper excitation coil with n turns. This C-shaped stator assembly is in turn clamped into a 3D-printed PMMA bracket, bolted to the optical breadboard. Current is measured using a sense resistor on a custom signal conditioning board, which measures the voltage drop over the magnetizing coil. An instrumentation amplifier board amplifies all sensor signals and low-pass filters them at 3 kHz in order to avoid aliasing. Sensor data is logged at 10 kHz with an NI 6351 USB X-series DAQmx I/O device [14]. DAQ output control signals are generated using the controller specified in section 2.2.3, programmed in NI LabVIEW and running on a laptop. The coil saturating magnetic field is limited at 30 V and 10 A, provided by a TI OPA549 linear-power amplifier and two Delta Elektronika ES 030-10 constant voltage power supplies [15]. Dimensioning and component specifications are summarized in table 3. For extended equipment and LabVIEW details, please refer to appendices A, B and C. Now, the influence of DRS, DA, FF and PPL compensation methods on static-gap tuning performance will be identified.

Table 3. Measured and obtained test setup parameters

Symbol	Value	Comment	Source
AlNiCo 5 magnet (Alcomax 3 / LNG44)			
l_m	30.20 mm	Magnet length	
d_m	9.83 mm	Magnet diameter	
B_r	1.25 T	Remanent flux density	[16]
H_c	50 kAm^{-1}	Coercive force	[16]
H_{sat}	150 kAm^{-1}	Saturation field intensity	
$\mu_{r,max}$	270	Max. relative permeability	
ρ	$4.75 \cdot 10^{-7}$ Ωm	Electrical resistivity	[16]
Copper coil			
n	668	Number of coil windings	
R	3.5 Ω	Electrical resistance	
Magnetic circuit (St. 37)			
A_g	200 mm^2	Air-gap surface area	
l_g	1.0 mm	Air-gap length	
$\mu_{r,avg}$	1000	Average relative permeability	

4.2 Experimental performance of Dynamic Recoil-line Compensation

In the practical experiments, air-gap magnetization levels of 25, 75 and 125 mT are evaluated in order to cover a large section of the feasible magnetization region - which

ranges between $0mT < B_g < 175mT$. For each set of test runs, we denote the Mean Average Error - *MAE* - and calculate the repeatability 3σ and predicted recoil line slope μ_{rec} from measurements. These values are determined after performing 25 measurement runs for every evaluated B_g. A constant air-gap length of $1000\mu m$ and tuning time of $500ms$ are used for each test run. Results are summarized in table 4.

Table 4. Measured air-gap flux density tuning performance of the DRS compensation method. All figures obtained with $N = 25$ measurement runs, for $l_g = 1000\mu m$ and $t_{tune} = 500ms$.

$B_g[mT]$	$\mu_{rec}[-]$	$MAE[mT]$	$3\sigma[mT]$
No compensation			
125	5.53	2.50	0.34
75	5.53	5.71	0.94
25	5.53	9.25	1.31
DRS Compensation			
125	5.51	2.28	0.34
75	5.18	2.17	0.78
25	4.85	1.99	0.87

When switched off, μ_{rec} was assumed constant for all values of B_g, and equal to 5.53 - corresponding to the assumption made in section 2.2.2. From table 4, we can see that *MAE* and 3σ values worsen for smaller air-gap magnetization levels when DRS compensation is switched off.
We can see that accounting for non-constant recoil line slope by switching on DRS compensation significantly decreases the observed *MAE* across all measured B_g states - with improvements ranging from 8.8% at $B_g = 125mT$ to 78.5% at $B_g = 25mT$. Furthermore, the *MAE* values become similar for all magnetization states, and repeatability also improves for each value of B_g - with up to 33.6% at $B_g = 25mT$. In general, it appears that DRS compensation offers a significant improvement both in tuning accuracy and repeatability during constant air-gap operation.

4.3 Experimental performance of Dynamic Air-gap Compensation

For the DA compensator, the performance is evaluated for a range of air-gap lengths l_g - instead of varying B_g. The air-gap flux density setpoint is fixed for all test runs - determined at $B_g = 75mT$ - and tuning time is set at 500 *ms*. Similar to the DRS method, measurements are performed 25 times. DA compensation is activated on top of the DRS compensation method. Results are summarized in table 5.

Investigating the influence of DA compensation on MAE, we can see that performance does not necessarily improve for all values of l_g. At small deviations from the benchmark $1000\mu m$ value, MAE performance seems to improve slightly. The largest improvement in accuracy can be observed for the smaller gap size of $l_g = 950\mu m$ - gaining just over 50% performance when compared to the off-case. However, for large deviations such as $1500\mu m$, the DA compensator appears to overshoot, causing the MAE value to worsen when compared to not using the compensator. In the worst case, this decline in performance approaches 7.5 % - at $l_g = 1500\mu m$. By only using DA compensation, equations (20), (21) and (16) overshoot, providing too much controller gain for an inaccurate B_c prediction. This issue can possibly be circumvented by using FF compensation in conjunction to DA compensation - as will be discussed in the next section.
On the other hand, enabling DA compensation appears to improve 3σ repeatability across the entire range of measured l_g-values. These improvements range from 37.1 % at $l_g = 1200\mu m$ to 77.2% at $l_g = 1500\mu m$ when compared to not using air-gap compensation.

Table 5. Measured air-gap flux density tuning performance of DA Compensation. All figures obtained with $N = 25$ measurement runs, for $B_g = 75mT$ and $t_{tune} = 500ms$. DRS compensation on.

$l_g[\mu m]$	$MAE[mT]$	$3\sigma[mT]$
DRS compensation		
950	2.78	7.73
1000	2.23	0.66
1200	7.13	0.70
1500	10.27	1.45
DRS + DA compensation		
950	1.36	1.95
1000	2.23	0.66
1200	6.39	0.44
1500	11.04	0.33

4.4 Experimental performance of Fringe Flux-loss Compensation

The experiments performed for DA compensation are repeated once more, but this time Fringe Flux-loss (FF) compensation is enabled along with the previously discussed DRS and DA compensation methods. The MAE and 3σ repeatability performance was gathered for both the on- and off-case. Furthermore, the system is again tuned 25 times to 75 mT for each instance of l_g, with a tuning time of 500 *ms*. The results are summarized in table 6.

Table 6. Measured air-gap flux density tuning performance of the FF compensation method. All figures obtained with $N = 25$ measurement runs, for $B_g = 75mT$ and $t_{tune} = 500ms$. DRS and DA compensation on.

$l_g[\mu m]$	$k_1[-]$	$MAE[mT]$	$3\sigma[mT]$
DRS compensation			
950	2.44	2.78	7.73
1000	2.44	2.23	0.66
1200	2.44	7.13	0.70
1500	2.44	10.27	1.45
DRS + DA + FF compensation			
950	2.40	2.18	0.86
1000	2.44	2.44	0.59
1200	2.60	3.68	0.83
1500	2.81	4.70	0.60

FF compensation - when used in combination with DRS and DA compensation - appears to have a positive influence on both MAE and 3σ repeatability for most of the measured air-gap range. The MAE values from $l_g = 950\mu m$ to $l_g = 1500\mu m$ no longer exceed 5 mT with FF compensation enabled - suggesting improved B_c - estimator robustness. Especially for larger air-gap sizes, MAE performance improves significantly - up to 54.2% at $l_g = 1500\mu m$. Furthermore, the compensator appears to improve the stability of 3σ: across the measurement range repeatability becomes more predictable and within a range of 1 mT. Because of these improvements, FF compensation in conjunction with DRS and DA compensation appears to result in a more stable and robust controller.

4.5 Experimental performance of Parallel PI Flux-feedback Control

Lastly, a Parallel PI (PPI) Flux-feedback controller is used in conjunction with the previously described DRS, DA and FF compensators. When disabled, only the benchmark inverted controller is used. When the parallel PI flux control is switched on, both inverted and PPI control are used as per figure 11. We revert to a constant air-gap length of $l_g = 1000\mu m$, with tuning times of 500 ms and B_g set to 25, 75 and 125 mT. Performance is summarized in table 7.

Table 7. Measured air-gap flux density tuning performance of the PPI Flux control method. All figures obtained with $N = 25$ measurement runs, for $l_g = 1000\mu m$ and $t_{tune} = 500ms$. DRS, DA and FF compensation on.

$B_g[mT]$	$MAE[mT]$	$3\sigma[mT]$
DRS + DA + FF compensation		
125	2.28	0.34
75	2.17	0.78
25	2.28	0.87
DRS + DA + FF + PPI compensation		
125	2.01	0.90
75	0.91	1.54
25	0.52	1.66

From table 7, we can deduct that parallel PI control improves MAE performance across the gap flux density measurement range, with improvements being the largest for lower magnetization levels - gaining up to 76.1% at $B_g = 25mT$. This effect can be attributed to the steady-state error reduction that can usually be expected from using an integrator in a controller.
On the other hand, 3σ repeatability appears to worsen across the entire range - almost doubling for 25 and 75 mT, and even tripling at 125 mT. Still, repeatability remains below an acceptable 2 mT, but in applications where repeatability is paramount, it might be beneficial to disable PPI control and settle for a larger MAE. Improved repeatability mat be achieved by investing more time in fine-tuning, which will ultimately result in a more stable controller.

5 Dynamic gap magnetization state tuning

Up to this point, a variation in l_g has been investigated for the different compensation methods. During the tuning process, however, all experiments have been performed with static air-gaps. In practical actuators, the air-gap length changes when a current is applied to the magnetizing coil [5]. Therefore, a hardware addition to the experimental setup is presented below, which allows the user to emulate motions that would occur in a practical actuator system.

5.1 Experimental setup overview

In order to allow for a change in air-gap length during magnet tuning, we must ensure that the mover is capable of providing linear motion relative to the Thorlabs precision stage presented in section 4. This allows the user to set the initial air-gap precisely before tuning, while simultaneously ensuring dynamic actuator movements during the magnetization process. In order to achieve this, a 4-member compliant flexure topology was designed - as shown in figure 13.

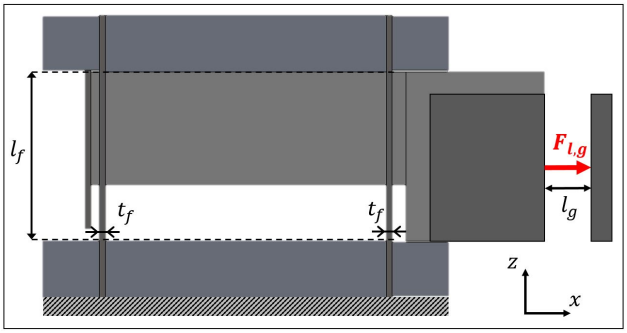

Fig. 13. Side view of the compliant 4-member flexure module. The bottom plate is mounted on the linear precision stage, while the mover yoke is connected to the free-moving top plate. Four parallel flexures with length l_f and thickness t_f connect the two plates, while the force F_g is exerted between stator (right) and mover (left) yokes, causing l_g to contract and extend.

Mover components are milled from 6068-grade Aluminium, with the flexures laser-cut from hardened spring steel. The finished module is shown in figure 14. Similar to the static-gap setup, a laser distance sensor is used to measure the dynamic response of the system. Magnetic circuit parameters remain unchanged, except the air-gap length l_g - which has been changed from 1 to 2 mm. Flexure dimensions are summarized in table 8. The magnet attraction force F_g is caused by the controllable gap magnetic flux density B_g, and can be written as equation (28) [10]:

$$F_g = \frac{2B_g^2 A_g}{\mu_0} \tag{28}$$

The force is multiplied by two, because we have two air-gaps of the same dimensions within the C-core circuit. In the

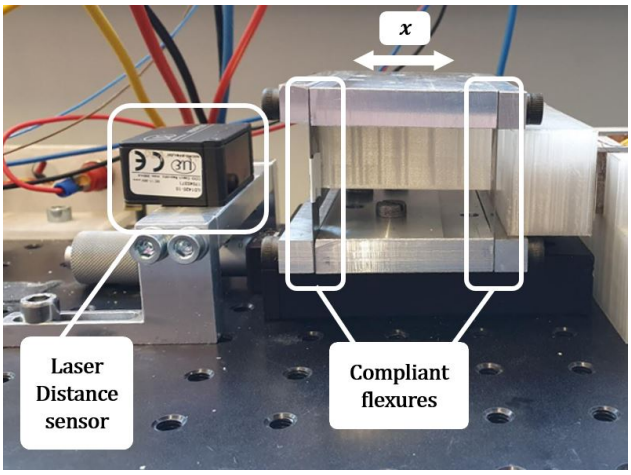

Fig. 14. The dynamic module is mounted on top of the pre-existing precision stage, combining accurate initial gap setting with dynamic motion capabilities.

Table 8. Measured and obtained test setup parameters

Symbol	Value	SI unit	Comment
Flexures (Hardened spring steel)			
n_f	4	[-]	Number of flexures
l_f	30	$[mm]$	Free-moving length
t	0.4	$[mm]$	Thickness
b	12.7	$[mm]$	In-plane width
E	180	$[GPa]$	Young's modulus

dynamic system, the pulling force of the actuator is opposed by spring force F_s: the product of x-direction flexure spring stiffness K_x and x-axis displacement s_x. Using linear beam equations, this can be written as [17]:

$$F_s = K_x \cdot s_x = \frac{4Eb_f t_f^3}{l_f^3} \cdot (l_{g,0} - l_g) \tag{29}$$

Here, b_f represents the in-plane width of the flexures, which is multiplied by four because of parallel placement of the four leaf springs. Spring displacement in x-direction s_x can be described by the difference in initial gap length - $l_{g,0}$ - and final gap length l_g. For large accelerations, the actuator drive force is also opposed by the mass of the mover system, in accordance with $F = m \cdot a$. In order to simplify initial stiffness calculations, accelerations are assumed to be small - eliminating this term from the equation, yielding:

$$F_{l,g} = F_{flex} \rightarrow \frac{2B_g^2 A_g}{\mu_0} = \frac{4Eb_f t_f^3}{l_f^3} \cdot (l_{g,0} - l_g) \tag{30}$$

Rewriting equation (30), we can find the stroke length by solving for $l_{g,0} - l_g$:

$$\text{stroke} = (l_{g,0} - l_g) = \frac{B_g^2 A_g}{\mu_0} \frac{l_f^3}{2Eb_f t_f^3} \tag{31}$$

We can see that the stroke is dependent on magnetic circuit as well as flexure parameters. B_g is completely tunable, l_f is fixed in order to ensure centered alignment between mover and stator yokes and t_f the easiest to alter by replacing the flexures for ones with different thickness. Using Matlab, we can predict s_x for different flexure thickness. Additionally, we investigate the displacement at saturation, maximum achievable B_g and at nominal $B_g = 50mT$. Simulation results are shown in figure 15.

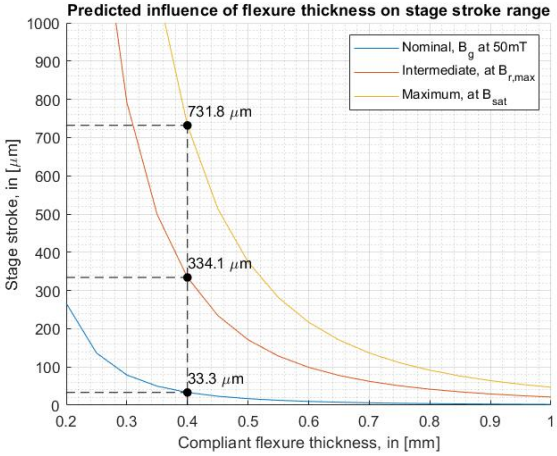

Fig. 15. Predicted mover displacements for a broad range of flexure thicknesses. Saturation B_g, maximum achievable B_g and nominal 50 mT B_g evaluated. Performed at 2000 μm gap length and circuit dimensions in accordance with table 3.

We can see that at different points of the tuning cycle, the maximum achievable stroke varies significantly. For example, using 0.4 mm thick flexures is predicted to yield a maximum deflection of 731 μm at saturation, falling back to 334 μm when we let go of the saturation current. This value is therefore the theoretical maximum stroke range of the actuator at rest. Demagnetizing to a nominal value of $B_g = 50mT$ yields a step of only 33 μm - twenty times less than at saturation. In the next section, we compare the measured compensator perormance for dynamic air-gap operation.

5.2 Dynamic Air-gap Compensator Performance

Similar to the static gap experiments, tests were performed 25 times for each magnetization level, with tuning times of 500 ms for all rounds. Using the MAE and 3σ, we can calculate the position accuracy and repeatability of the mover by rewriting equation (31) to:

$$\begin{cases} \Delta x_{MAE} = \frac{(MAE)^2 A_g}{\mu_0} \frac{l_f^3}{2Eb_f t_f^3} \\ \Delta x_{3\sigma} = \frac{(3\sigma)^2 A_g}{\mu_0} \frac{l_f^3}{2Eb_f t_f^3} \end{cases} \quad (32)$$

We first compare the dynamic performance for two instances: tuning without any compensators as opposed to tuning with DRS, ED, FF and PPI all enabled. The results of these experiments are summarized in table 9.

Table 9. Measured dynamic air-gap flux density tuning performance. All figures obtained with $N = 25$ measurement runs, for $l_g = 2000\mu m$ and $t_{tune} = 500ms$.

B_g $[mT]$	MAE $[mT]$	Δx_{MAE} $[\mu m]$	3σ $[mT]$	$\Delta x_{3\sigma}$ $[nm]$
No compensation				
50	19.18	5.58	2.38	85.89
25	19.35	5.68	3.49	184.69
0	7.33	0.81	3.76	214.37
DRS, ED, FF and PPI on				
50	6.75	0.69	0.75	8.53
25	7.39	0.83	0.70	7.43
0	3.15	0.15	1.93	56.48

From table 9, we can clearly see that - similar to the static-gap experiments - the performance improves across the board when the compensation methods are switched on. Depending on the level of magnetization, MAE and 3σ can both be reduced by two to three times. Additionally, the position error has been reduced from a maximum of 5 μm to full-range sub-1 μm precision. Lastly, position repeatability has been improved significantly from approximately 80-200 nm to 8-50 nm. Analyzing the individual contribution of the compensation methods, we obtain table 10.

Table 10. Measured dynamic air-gap flux density tuning performance improvements for invividual compensators. All figures obtained with $N = 25$ measurement runs, for $B_g = 50mT$ and $t_{tune} = 500ms$.

Compensation method	MAE $[mT]$	MAE gain $[\%]$	3σ $[mT]$	3σ gain $[\%]$
None (reference)	19.18	-	2.38	-
DRS	8.72	55	1.92	19
DRS, ED & FF	7.55	61	0.78	67
DRS, ED, FF & PPI	6.75	65	0.75	68

The biggest improvement in MAE accuracy can be attributed to the DRS compensation method, which reduces MAE with 55% when compared to the reference value. Enabling the other compensators seems to be worthwile for MAE reduction, as an additional 10% reduction in B_g MAE translates to approximately 40% reduction in position error.

Looking at 3σ repeatability, we can see that DRS compensation again provides a decent 19% performance improvement. This time, however, the largest contribution comes from enabling ED and FF compensation on top of this, which improves the repeatability by an additional 48% - translating to 84 % reduction in repeatability position error. Of all compensators, parallel PI flux control appears to contribute the least in this category.

6 Conclusion

In order to emulate the dynamic behaviour of a gap-closing reluctance actuator, a 4-member compliant flexure topology was designed and built. Although this research used hardened spring steel flexures with a thickness of 0.4 mm, the components can be interchanged - allowing for more extensive future experimentation. The initial air-gap length can be precisely set by utilizing the pre-existing manual linear precision stage, while the modular flexure stage adds dynamic motion during actuator operation.

In conjunction with the stage, the integration of a laser triangulation distance sensor now allows the user to read out motion stage displacements. This made it possible to study the dynamic behaviour of the motion system when subjected to a TM actuator tuning cycle. Lastly, because displacements can now be measured, the position and flux feedback data can be used in parallel to refine the calculations of the proposed compensating techniques - improving robustness, accuracy and repeatability of the tuning method. The four compensation methods provide major performance improvements - both in static and dynamic operation.

Rewriting the existing DRS compensation method to a continuous, analytical equation allowed for easy substitution into the corner-point magnetization algorithm. In turn, the user no longer needs to use a look-up table in order to find the corner-point magnetization corresponding to the desired air-gap magnetization. The DRS method significantly increases tuning performance, displaying between 8.8 to 78.5 % reduction in MAE - improving accuracy - and up to 33.6 % gains in 3σ repeatability. Because of this, MAE and 3σ remain below 2.3 and 0.9 mT respectively at baseline 1000 μm air-gap length.

Using the air-gap measurements of the laser triangulation distance sensor, DA compensation continuously updates the values for l_g in corner-point and gain computations. Adding DA to the DRS compensation method enabled up to 50 % MAE reduction for air-gap lengths smaller than the 1000 μm baseline value. For large values of l_g, the compensator appeared to overshoot - causing an increase in MAE of up to 7.5 % at 1500 μm. Conversely, repeatability 3σ appeared to improve across the board - ranging from 37.1% at 1200 μm to 77.2% at 1500 μm.

Introducing FF to DA and DRS compensation, the tuning performance stabilizes for all gap lenths considered in this research. The combination of FF and DA compensation more dan halves the *MAE* error at 1500 μm, and across the entire range *MAE* no longer exceeds 5 mT - making the system very stable. repeatability performance also sees great improvements, with 3σ values never exceeding 1 mT - for all air-gap lengths. In conclusion, DA and FF need to be used in tandem in order to ensure stabilized tuning control.

Placing a PI flux-feedback controller in parallel with the inverted controller yields some mixed results. On one hand, *MAE* can be reduced significantly - with up to 75% improvement recorded for 25 mT gap magnetization at $l_g = 1000\mu m$. On the other hand, 3σ appears to worsen across the entire range of magnetization levels - almost doubling for values of 25 and 75 mT. Still, repeatability remains within 2 mT at all times, so some aplications the potential *MAE* error reduction might outweigh the reduction in 3σ repeatability.

At a large dynamic air-gap length of 2000 μm, the actuator cannot be used without compensation methods, as demonstrated by table 9. The problem with accuracy can be easily solved by adding DRS compensation on top. This way, Δx_{MAE} is reduced by almost five times to just over 1 μm, with a third reduction in $\Delta x_{3\sigma}$ - down to 56 nm. Similar to static gap experiments, adding ED and FF compensation on top significantly imroves stability and thus position repeatability - which is now improved by almost ten times to less than 10 nm. The introduction of PPI control in dynamic operation yields a slight improvement in both *MAE* and 3σ performance, but not enough to warrant full implementation. Perhaps with improved controller tuning, this contribution can be improved.

Future work therefore includes improving the tuning speed of the magnet, in order to allow for more versatile applications. This can be achieved by in-depth design of a proper PPI flux-feedback controller, yielding better rise times and possibly even improved stability and accuracy. Additionally, a switch from DAQ-based signal acquisition to an FPGA-based approach will already increase computational power, which as a result reduces tuning times significantly.

References

[1] Lomonova, E. A., 2010. "Advanced actuation systems - State of the art: Fundamental and applied research". *2010 International Conference on Electrical Machines and Systems, ICEMS2010*, pp. 13–24.

[2] Hüfner, T., Radler, O., Ströhla, T., Sattel, T., Wesselingh, J., Vogler, A., and Eicher, D., 2017. "A note on electromagnetic gravity compensation actuators based on soft electro-permanent magnets for adjustable reluctance force". *Proceedings of the 17th International Conference of the European Society for Precision Engineering and Nanotechnology, EUSPEN 2017*(May), pp. 149–150.

[3] Philips Innovation Services, 2016. "Comparative evaluation of Lorentz and reluctance actuators". pp. 1–3.

[4] Vrijsen, N. H., Jansen, J. W., and Lomonova, E. A., 2010. "Comparison of linear voice coil and reluctance actuators for high-precision applications". *Proceedings of EPE-PEMC 2010 - 14th International Power Electronics and Motion Control Conference*(October).

[5] Munnig Schmidt, R., Schitter, G., Rankers, A., and Van Eijk, J., 2014. *The Design of High Performance Mechatronics*, 2nd revise ed. Delft University Press - IOS Press BV, Amsterdam.

[6] Knaian, A., 2010. "Electropermanent magnetic connectors and actuators : devices and their application in programmable matter". PhD thesis, Massachusetts Institute of Technology.

[7] Campbell, P., 1994. *Permanent Magnet Materials and their Application*. Cambridge University Press.

[8] Parker, R., 1990. *Advances in Permanent Magnetism*. John Wiley and Sons, Inc.

[9] Roters, H., 1941. *Electromagnetic Devices*, first edit ed. John Wiley and Sons, Inc., New York.

[10] Viëtor, S. G., 2018. "Tunable Magnets: Modeling and Validation for Dynamic and Precision Applications". PhD thesis.

[11] Thorlabs, 2021. "Optical Breadboard". *url: https://www.thorlabs.com/newgrouppage9.cfm?objectgroup_id=159*(accessed: 29-07-2021).

[12] Thorlabs, 2021. "Manual Linear Stage". *url: https://www.thorlabs.com/newgrouppage9.cfm?objectgroup_id=706*(accessed: 29-07-2021).

[13] Micro Epsilon, 2021. "optoNCDT ILD1420-10 sensor". *url: https://www.micro-epsilon.com/displacement-position-sensors/laser-sensor/optoNCDT_1420_CL1/*(accessed: 29-07-2021).

[14] National Instruments, 2021. "USB-6351X DAQmx module". *url: https://www.ni.com/nl-nl/shop/hardware/products/multifunction-io-device.html?modelId=124936*(accessed: 29-07-2021).

[15] Delta Elektronika, 2021. "ES 030-10 specifications". *url: https://www.delta-elektronika.nl/en/products/dc-power-supplies-300w-es300-series.html*(accessed: 29-07-2021).

[16] Eclipse Magnets, 2017. "Alnico Magnets Datasheet". pp. 5–8.

[17] JPE Innovations, 2021. "Compliant Mechanism Design". *url: https://www.jpe-innovations.com/precision-point/2-leaf-springs-parallel/*(accessed: 29-07-2021).

4

Tunable Magnets: Validation and Reduction of the Break-even Tuning Interval

Using Minor-loop Magnetization State Tuning

Tunable Magnets: Validation and Reduction of the Break-even Tuning Interval

Using Minor-loop Magnetization State Tuning

1 Introduction

In precision engineering, thermal stability is of great importance in order to keep up with the ever-increasing demand for faster and more precise positioning actuators. Most notably, actuator magnetizing coils dissipate heat to surrounding machine components as a result of Joule heating. With changing temperatures, system components expand and contract - causing unwanted structural deformations that can lead to a decline in positioning accuracy and repeatibility [1,2]. Traditionally, Lorentz actuators were favored for high-precision applications, due to their inherently linear force-current relationship - making them highly predictable [3]. This type of actuator, however, is also characterized by a low force density - which results in relatively poor efficiency [4]. In recent years, the control predictibility of modern reluctance actuators has improved significantly – allowing for up to 10 times larger force-density when compared to Lorentz actuators [4]. Larger force-density greatly reduces the actuator size and thus magnetizing current required for positioning, which in turn improves energy efficiency [5]. Still, the effect of Joule heating within EM reluctance actuators remains especially pronounced during quasi-static operation, where the magnetizing current of the EM actuator must be sustained for extended periods of time. Additionally, many high–precision systems operate within challenging conditions - often requiring large bias forces in a vacuum environment.

1.1 Prior art

Prior research has attempted to find methods that improve actuator efficiency for quasi-static operation. Typically, the methods propose a variation of a hybrid reluctance actuator topology to improve this. A.N. Knaian was first to introduce the concept of in-situ magnetization adjustment of AlNiCo, with the switchable Electropermanent Magnet (EMP) actuator [6]. In parallel with a soft AlNiCo magnet, a hard NdFeB magnet is placed - both surrounded by a single magnetizing coil. The AlNiCo magnet can be more easily (de-) magnetized when compared to hard NdFeB magnets typically found in hybrid reluctance actuators [7–9]. This way, by switching the magnet to the 'on'-state with a single current pulse, the magnet sustains the magnetization state after tuning - even after all current has subsided. During stationary periods, little to no additional energy loss is expected, which makes this method especially efficient for quasi-static operation.

In 2018, S.G. Viëtor introduced a method to accurately tune an AlNiCo magnet to a set of user-predefined magnetization states [10]. Contrary to Knaian's 'on'- and 'off'-state, this novel method allows for a selection of intermediate states - allowing the user to set the circuit air-gap flux density level with 25 mT increments. The three largest contributions from the work can be summarized as the development of the novel Saturation Magnetization State Tuning (SMST) algorithm, experimental validation of TM performance on a practical static-gap setup and introduction of the Break-even Tuning Interval (BTI) metric - which allows for an efficiency comparison between novel TM and conventional EM actuators. The setup is shown in figure 10, with component dimensions summarized in table 1.

1.2 Research contributions

This research is a continuation of Viëtor's work, and part of an ongoing research program investigating the application of in-situ magnetization adjustment of AlNiCo magnets. While the work performed prior to this research establishes the BTI metric using analytical predictions, it has remained invalidated until now. Experimentally validating this metric would allow for extrapolation of observed results: offering a prediction of achievable TM actuator performance for improved tuning times. This will yield greater insight into the possible areas of TM actuator application and performance limitations.

Additionally, prior research has voiced concerns over the saturation step of the TM tuning cycle [10]. Performing this step requires large magnetizing currents, which in turn can cause excessive pulling forces between the actuator stator and mover. This issues no concern in a static-gap setup, but when the actuator is allowed to move, this force can cause large initial deflections - possibly resulting in long settling times and increased component stress. Moreover, the large power draw during saturation means that although short in comparison to demagnetizing, this tuning step accounts for at least half of the energy losses of a TM tuning cycle - therefore limiting efficiency and worsening estimated BTI [10].

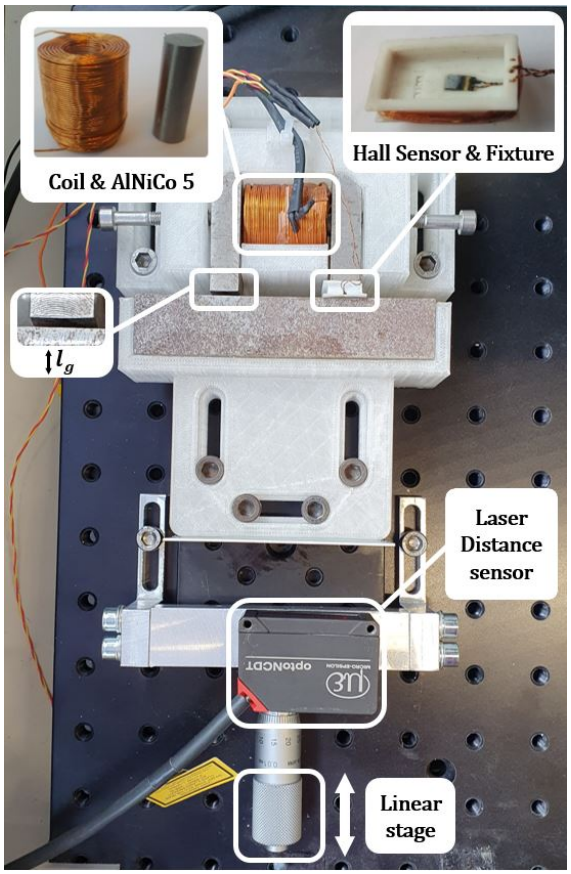

Fig. 1. Overview of the pre-existing static-gap experimental setup. Introduced by this research are the laser triangulation distance sensor and its mounting bracket.

In this paper, a novel Minor-loop Magnetization State Tuning (MMST) method is proposed - making use of the minor BH-curve hysteresis loops. By excluding the saturation step from the tuning sequence, the amount of energy loss can potentially be significantly decreased. This reduces BTI values, making the TM actuator more widely applicable. Simultaneously, the new method is provides improvements in dynamic system movements and tuning times due to reduced peak pulling forces.

Additionally, the existing setup - as referenced in figure 1 and table 1 - will be subjected to experimental BTI validation for a broad range of tuning times and gap magnetization levels. Projections for energy loss and BTI performance at short tuning times have also been performed - allowing for better understanding of possible future areas of application.

2 Limitations of Saturation TM Control

Up to this point, only the Saturation Magnetization State Tuning (SMST) method has been considered for TM state tuning. The compensator developments of chapter 3 contribute to corner-point prediction accuracy and repeatibility,

Table 1. Measured and obtained test setup parameters

Symbol	Value	Comment	Source
AlNiCo 5 magnet (Alcomax 3 / LNG44)			
l_m	30.20 mm	Magnet length	
d_m	9.83 mm	Magnet diameter	
B_r	1.25 T	Remanent flux density	[11]
H_c	50 kAm^{-1}	Coercive force	[11]
H_{sat}	150 kAm^{-1}	Saturation field intensity	
$\mu_{r,max}$	270	Max. relative permeability	
ρ	$4.75 \cdot 10^{-7}$ Ωm	Electrical resistivity	[11]
Copper coil			
n	668	Number of coil windings	
R	3.5 Ω	Electrical resistance	
Magnetic circuit (St. 37)			
A_g	200 mm^2	Air-gap surface area	
l_g	1.0 mm	Air-gap length	
$\mu_{r,avg}$	1000	Average relative permeability	

whilst still using the SMST method. This chapter focuses on the limitations of the SMST method, and a novel tuning method - Minor-loop Magnetization State Tuning (MMST) is proposed to overcome these issues. We recognize three aspects of performance: mover dynamics, tuning time and energy consumption. The latter is closely related to the Break-even Tuning Interval (BTI) metric, which is introduced in section 6.1.

2.1 Mover dynamics

Ensuring relatively simple implementation and providing adequate robustness, a TM actuator can be controlled by using the SMST control method - as introduced by [10]. Recalling from chapter 3, we consider three consecutive tuning steps: $Saturate \rightarrow Demagnetize \rightarrow Decay$, which are also shown once more in figure 2. It was previously shown that saturation of the magnetic circuit can be determined by using:

$$I_{sat} = \frac{l_m}{n}\left[H_{sat} + 2\left(\frac{k_2}{k_1}\right)\cdot\left(\frac{B_r}{\mu_0} + H_{sat}\right)\cdot\frac{A_m l_g}{A_g l_m}\right] \quad (1)$$

Using the dimensions of the experimental setup as denoted in table 1 - the required saturation current for an air-gap length of $l_g = 1000\mu m$ amounts to $I_{sat} = 7.34A$. This can even approach $I_{sat} = 9.0A$ for values closer to $l_g = 2000\mu m$. Using Ohm's law and the measured coil resistance of $R = 3.5\Omega$, the required saturation voltage can be determined to be approximately $U_{sat} = 25.7V$. As mentioned before, a large advantage of this method is that only the major BH-curve must be measured beforehand in order to accurately predict the demagnetization corner-point B_c - instead of requiring measurement data of many minor demagnetization loops. The method, however, also has some limitations. In a moving-gap actuator system, for example, the gap flux density at saturation can be multiple times larger than when tuned to a new magnetization state, as shown in figure 3.

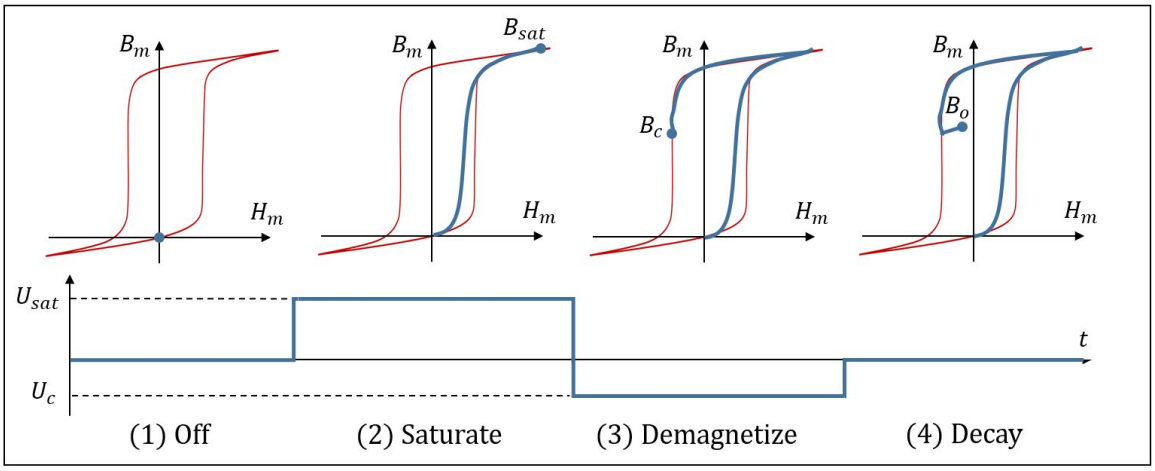

Fig. 2. Sequencing of the four-step SMST tuning method. After saturation (2), the corner-point is reached by demagnetizing the AlNiCo magnet (3). Because of irreversibility, we revert along one of the recoil lines towards the new operating point - B_o.

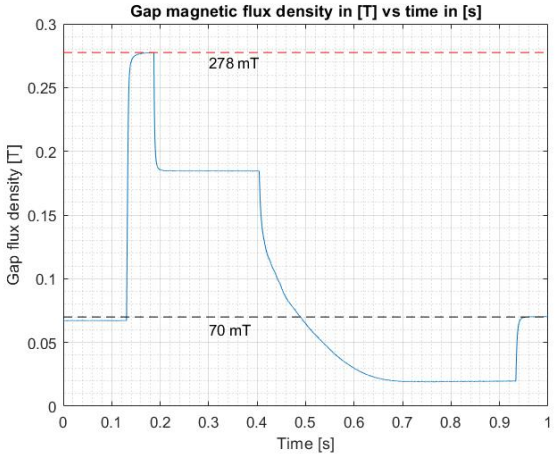

Fig. 3. Using SMST, gap magnetic flux density at saturation approaches 278 mT - almost four times as much as the rest state.

At saturation, we can see that gap magnetic flux density can reach values close to $B_{sat} = 278mT$, which turns out to be almost four times as much as the desired magnetization state of $B_g = 75mT$. We can calculate the force generated by the magnetic circuit by using:

$$F_g = \frac{2B_g^2 A_g}{\mu_0} \tag{2}$$

Using equation (2) with gap flux densities B_{sat} and B_g, we find that at peak magnetization B_{sat} the pulling force can be estimated at 24.6 N, compared to just 1.8 N at $B_g = 75mT$. This peak force is more than ten times larger than the force in the desired state. For a static air-gap approach, this is not an issue as the gap is physically restricted from changing in length. However, when the four-member compliant flexure setup demonstrated in chapter 3 is attached, this amount of force difference can cause large undesired deflections at saturation. We revisit the force equilibrium equation as proposed before in chapter 3:

$$F_{l,g} = F_{flex} \rightarrow \frac{2B_g^2 A_g}{\mu_0} = \frac{4Eb_f t_f^3}{l_f^3} \cdot (l_{g,0} - l_g) \tag{3}$$

Which was rewritten to find the setup stroke:

$$\text{stroke} = (l_{g,0} - l_g) = \frac{B_g^2 A_g}{\mu_0} \frac{l_f^3}{2Eb_f t_f^3} \tag{4}$$

Solving for B_{sat} and B_g, we find a maximum estimated deflection of 1135 μm for an intial air-gap length of 1000 μm - meaning that the actuator would shut completely, causing wear and tear. Simultaneously, the $B_g = 75mT$ gap flux density would only cause 83 μm of stroke.
To avoid shutting of the circuit, we recalculate deflection for an increased initial air-gap length of $l_g = 2000\mu m$. With these conditions, maximum estimated deflection at saturation would reach 832 μm - which avoids shutting completely but is still significant. Experimental validation of these calculations is provided in section 5.5.

2.2 Tuning time

With the SMST method, LabView tuning controller and DAQmx hardware, total tuning time for each of the three tuning steps can be subdivided as:

1. **Saturation:** 50 ms
2. **Demagnetizing:** 500 ms
3. **Decay:** 25 ms

We can see that with almost 90 % of total tuning time, the largest contributor remains the demagnetizing step. This

can be attributed to the limitations of the control hardware and software - which runs LabView on the NI 6351 USB X-series DAQmx I/O device [12]. Replacing this approach for an FPGA-based application will greatly improve control bandwidth - allowing tuning times to be significantly reduced [13]. At small time-scales, we can approach the magnetizing currents as exponemintial curves - as illustrated by figure 4 and equations (5), (6) and (7) [10].

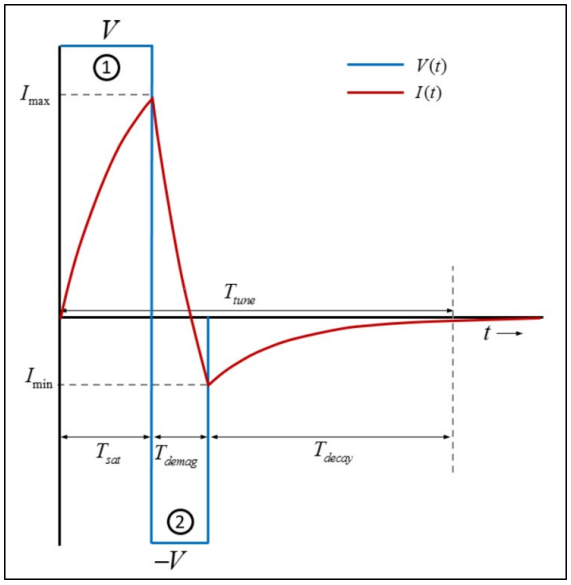

Fig. 4. Small time-scale tuning steps as approximated with exponential current curves. Adapted from [10].

$$I_{sat}(t) = \frac{U_{sat}}{R}\left(1 - e^{-\frac{tR}{L}}\right) \tag{5}$$

$$I_{demag}(t) = I_{sat}e^{-\frac{tR}{L}} - \frac{U_{sat}}{R}\left(1 - e^{-\frac{tR}{L}}\right) \tag{6}$$

$$I_{decay} = I_{min}e^{-\frac{tR}{L}} \tag{7}$$

Where L and R are the coil self-inductance and resistance. I_{sat} was previously defined as saturation current using equation (1). I_{min} indicates the current required for the largest possible demagnetizing step: from B_r down to 0 mT - and can be determined using equation 8 [10]:

$$I_{min} = -\frac{l_m}{n}H_{c,i} \tag{8}$$

Rewriting equations (5 - 7) explicit for elapsed time yields a prediction for the minimum amount of time needed for each of the tuning steps [10]:

$$T_{sat} = \frac{L}{R}ln\left(\frac{U_{sat}}{U_{sat} - I_{sat}R}\right) \tag{9}$$

$$T_{demag} = \frac{L}{R}ln\left(\frac{U_{demag} + I_{sat}R}{U_{demag} - I_{min}R}\right) \tag{10}$$

$$T_{decay} = \frac{L}{R}ln\left(\frac{I_{min}}{I_{zero}}\right) \tag{11}$$

The value of I_{zero} is chosen close to zero, in order to mark the end of the exponential current decay. Using the circuit dimensions detailed in table 1, minimum achievable tuning times become:

1. **Saturation:** 24 *ms*
2. **Demagnetizing:** 12 *ms*
3. **Decay:** 20 *ms*

So, when the system is not limited by control hardware, the distribution of required tuning step times changes significantly. In this case, demagnetizing only accounts for just over 20% of total tuning time. Eliminating the saturation step would almost halve the total required tuning time, which has another advantage: a decrease in energy consumption.

2.3 Energy loss

Apart from tuning time and system dynamics, we can also analyze the energy consumed by the system. In a TM actuator layout, energy loss can be subdivided into two components: hysteresis loss of the PM material and Joule heating of the magnetizing coil.

2.3.1 AlNiCo 5 Hysteresis Loss

Hysteresis loss is proportional to the volume of magnetic material - $A_m l_m$ - and the surface beneath the hysteresis curve - which depends on the traversed tuning path. The worst-case tuning loop can be described by: starting at $(0,0) \rightarrow$ saturating $(H_{sat}, B_{sat}) \rightarrow$ demagnetizing to 0 mT $(-H_{c,i}, 0)$. In this case, we traverse the top half of the major BH-curve, as also shaded light-grey in the simplified BH-curve approximation shown in figure 5.

Approximating the BH-curve as a parallellogram-shaped hysteresis path simplifies the analytical calculation of hysteresis loss, which can be determined by using [10]:

$$E_{hyst} = A_m l_m \int H_m dB_m = 2 \cdot A_m l_m B_r H_{c,i} \tag{12}$$

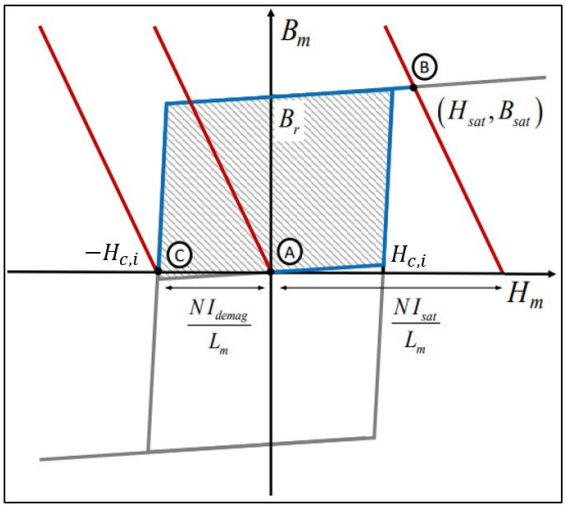

Fig. 5. Paralellogram-shaped hysteresis approximation, used to simplify hysteresis loss estimations. Adapted from [10]

For the circuit dimensions and AlNiCo 5 magnet characteristics as presented in table 1, the maximum hysteresis loss can be estimated at approximately $E_{hyst,max} = 0.29J$.

2.3.2 Magnetizing Coil Joule Heating

Because of the electrical resistance of the magnetizing coil, a power loss to occur when it is subjected to current: Joule heating. This ultimately heats up the magnetizing coil and surrounding materials - which can cause the positioning errors in high-precision machinery. Therefore, we aim to reduce the contribution of Joule heating as much as possible. The power loss for each tuning step can then be written as:

$$P_{step} = I_{step}^2 R \tag{13}$$

Where I_{step} can be substituted for equations (5 - 7). Doing so, we obtain an estimation of the power loss for each individual tuning step:

1. **Saturation:** 188.6 Js^{-1}
2. **Demagnetizing:** 17.7 Js^{-1}
3. **Decay:** 3.5 Js^{-1}

Here, we can see that the average power consumed during operation varies quite significantly with each tuning step. During saturation, for example, power loss is estimated to be at least 10 times larger when compared to demagnetization and decay. With this, we can then predict the total amount of energy used for each tuning step by integrating the step power over individual tuning step times, using equation (14):

$$E_{step} = \int P_{step} dt \tag{14}$$

Summating this for all tuning steps finally yields a prediction of the total amount of energy lost by the magnetizing coil:

$$E_{coil} = \int_0^{T_{sat}} P_{sat} dt + \int_0^{T_{demag}} P_{demag} dt + \int_0^{T_{decay}} P_{decay} dt \tag{15}$$

Using the step power estimations found previously by equation (13), we can approximate the energy loss contributions of each tuning step:

1. **Saturation:** 9.43 J
2. **Demagnetizing:** 8.85 J
3. **Decay:** 0.09 J

Using this estimate, we can see that saturating and demagnetizing have an almost equal contribution to the total amount of energy lost by Joule heating. Earlier, we established that saturation power loss is about ten times larger when compared to the demagnetizing step. However, the time required for saturation is currently ten times less than demagnetizing - causing energy losses to be roughly equal. This, however, means that cutting out the saturation step from the SMST method already halves the total amount of energy lost at long tuning times, while potentially providing even more benefit if demagnetization tuning times can be reduced to a minimum. An alternative to the SMST method is proposed in section 4. First, we introduce the performance metric that will allow us to compare TM and EM actuator performance: the Break-even Tuning Interval (BTI).

3 The Break-even Tuning Interval

Depending on the application, a TM actuator may not provide a large advantage over existing EM actuator solutions. In some cases, performance may even be worse. Comparing the losses of a TM actuator with an EM actuator, it will become apparent that the latter provides more efficiency at high operating frequencies, whereas the TM actuator excels at lower values. In order to determine whether TM actuators can serve as an alternative or even improvement to existing EM reluctance actuators, the Break-even Tuning Interval (BTI or T_{be}) was introduced [10]. The interval is defined as the time required between magnetization tuning cycles, such that a TM actuator dissipates the same amount of energy as a comparable EM actuator. For example, if we find T_{be} to be 10 ms for an application requiring tuning at frequencies of 5 Hz - corresponding to 20 ms intervals, the TM actuator will be more efficient when compared to an EM actuator. In this section, we will derive the calculation of BTI and discuss how it can be visualized.

3.1 EM-actuator layout and BTI calculation

We first consider the differences between the TM and EM magnetic circuit topologies. In figure 6, a schematic overview of an EM actuator circuit is shown, bearing great resemblance to the TM circuit introduced earlier. This time,

however, the AlNiCo 5 permanent magnet is removed, and only two components remain: stator A and mover B. Both are constructed from weak iron St. 37 core material. Dimensions are identical to the TM actuator - as introduced in table 1. Still remaining is the magnetizing coil, of which the dimensions also remain unchanged.

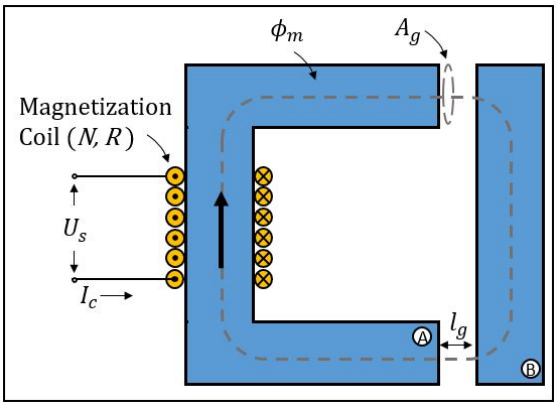

Fig. 6. Typical EM-actuator layout: the AlNiCo magnet is removed, creating a single stator yoke (A), made of the same soft iron material as mover (B). The magnetizing coil still surrounds the stator yoke.

With the AlNiCo 5 permanent magnet removed, the magnetizing current equation for this circuit can be simplified. The magnetizing coil is now the only flux source, and just the two air-gaps provide circuit reluctance. This yields the simplified circuit equation:

$$nI_{EM} = 2H_g l_g \tag{16}$$

Using $B_g = \mu_0 H_g$ to determine the gap flux density and rewriting for I, we arrive at:

$$I_{EM} = \frac{2B_g l_g}{\mu_0 n} \tag{17}$$

An EM actuator is only capable of sustaining a constant air-gap flux density when it is supplied with a continuous magnetizing current. Contrary to a TM actuator - where the magnetizing pulse train allows the circuit to sustain the desired magnetic flux indefinitely - this means that longer times between position changes cause more energy loss. The power associated with each magnetization state can be determined using equation (18).

$$P_{EM} = I_{EM}^2 R \tag{18}$$

To find the BTI we equate the energy loss of the TM actuator E_{TM} with the power loss of an EM actuator:

$$T_{be} = \frac{E_{TM}}{P_{EM}} = \frac{E_{coil} + E_{hyst}}{P_{EM}} \tag{19}$$

This yields the estimated time in s between tuning cycles for which the TM actuator becomes more efficient than an EM actuator.

3.2 Visualization of BTI

We can illustrate the BTI of the tuning methods by comparing the energy consumption of both an EM and TM actuator over time, as demonstrated in figure 7. The EM actuator has a linear characteristic, because of the constant power that is required to hold position. Contrary to this, we see that the TM tuning methods initially consume more energy during the tuning step, but afterwards require none at all. This way, the continuous consumption of the EM actuator eventually catches up for longer stationary times - intersecting with the TM curve. From figure 7, we can estimate the BTI for the SMST method at 3.55 s.

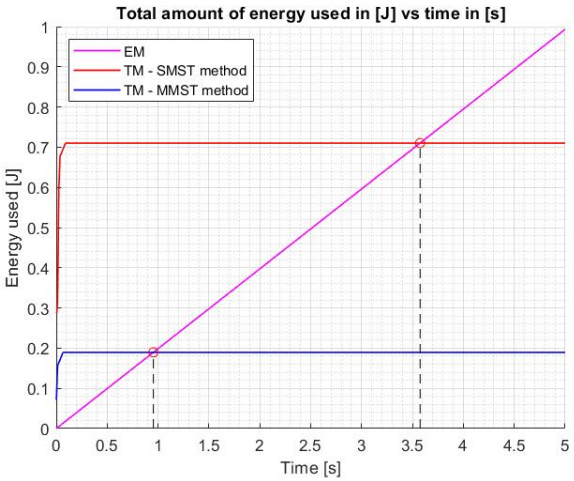

Fig. 7. Visualization of BTI prediction, for both the SMST and MMST methods. Used variables: $B_g = 50mT$, $l_g = 2000\mu m$, $T_{sat} = 24ms$, $T_{tune} = 12ms$.

In section 6.1, projected BTI values will be validated using practical experiments. First, we consider an alternative to the SMST method - aiming to mitigate some of the limitations that were introduced in the previous section.

4 Alternative Tuning Methods

In order to reduce the dynamic, time and energy constraints that the SMST method imposes on the TM system, two alternative tuning strategies have been proposed. The first was proposed by [10], in order to improve on the SMST method during down-steps.

4.1 Hybrid TM State Tuning Method

In his 2018 research, Viëtor recognized that saturating the magnet for every tuning step is suboptimal from an energy loss perspective. Therefore, a hybrid method was proposed - in accordance with figure 8: if the magnetization level of the new desired operating-point B_o lies *above* the currently measured value B_m, the algorithm saturates the magnet before demagnetization - just like the SMST method. However, if the new operating point lies *below* the measured value, only a demagnetizing step is applied. This was possible because the recoil-line slopes - μ_{rec} - were quite well-understood for the second quadrant, allowing for proper corner-point estimation along the minor loops.

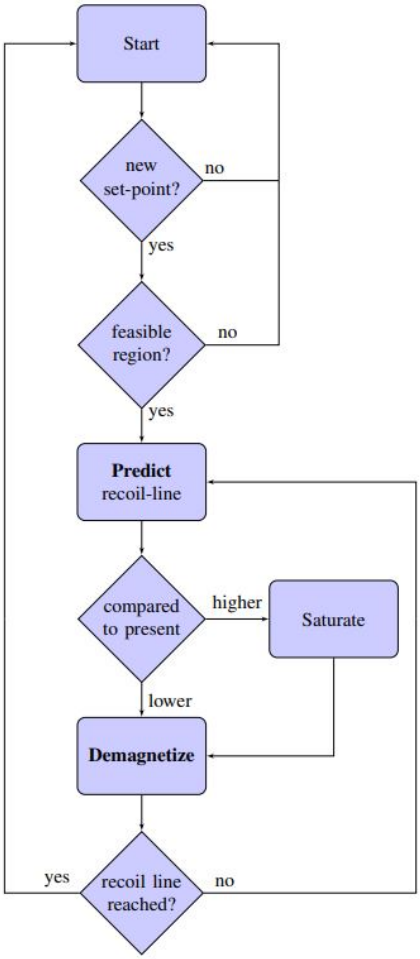

Fig. 8. Flowchart representation of the hybrid TM state tuning methods: up-steps require saturation, whereas downsteps can immediately demagnetize. Adapted from [10].

This tuning method is already an improvement over the default SMST method during down-steps, but for up-steps the limitations of sections 2.1 to 2.3 prevail. Therefore, a novel TM actuator tuning method is proposed in this research: the Minor-loop Magnetization State Tuning (MMST) method.

4.2 Envelope TM State Tuning Method

We remember from chapter 3 that in order to tune a TM material properly, saturating first and then demagnetizing requires us to find the corner-point intersection in the second quadrant of the BH-curve. Adding compensation methods such as DRS, DA, FF and PPI flux-feedback control has been shown to improve both tuning accuracy and repeatibility - as evidenced by chapter 3. In order to achieve robust up-steps without using magnet saturation, we must also precisely determine the corner-point (H_c, B_c) in the *first* quadrant. For this, we rewrite the second-quadrant corner-point equation for first-quadrant operation, yielding a set of corner-point prediction equations for both quadrants:

$$\begin{cases} B_{c,q_1} = \frac{B_r - \mu_0 \mu_{r,max} H_c}{\left(\frac{\mu_{r,max}}{\mu_{rec}}\right) - 1} + B_r \\ B_{c,q_2} = \frac{B_r + \mu_0 \mu_{r,max} H_c}{\left(\frac{\mu_{r,max}}{\mu_{rec}}\right) - 1} + B_r \end{cases} \tag{20}$$

So, we use the first-quadrant corner-point prediction for up-steps and second-quadrant prediction for down-steps. An example of an up-step using the MMST method is demonstrated in figure 9. We notice that the first-quadrant corner-point intersections are expected to appear higher along the major BH-curve - which would indicate a reduced air-gap operating range of the MMST method when compared to SMST. It is expected that the MMST method provides major improvements to all three limitations of the SMST method. By eliminating the saturation step, we require significantly less magnetizing current when compared to complete saturation. Therefore, magnetization levels in the air-gap will also remain more modest, causing less deflection on the mover stage - in turn improving dynamic performance. Additionally, tuning times can be shortened because the time required for saturation can now be removed from the total tuning cycle. Lastly, it is expected that because of the reduced tuning current, the energy loss will also be decreased - improving TM actuator efficiency. In the practical experiments, the performance of the proposed new MMST tuning method is compared to the existing SMST method.

5 Experimental performance comparison between the SMST and MMST method

We compare the performance between the SMST method used by [10] with the new MMST method in four major areas:

1. Mover dynamics: the behaviour of and disturbance given to the moving stage.
2. Tuning time: the degree to which total tuning times can be reduced.
3. Energy loss: the amount of energy lost after a full cycle.
4. Accuracy and repeatibility: the precision of the tuning methods.

We begin with a short overview of the practical setup used for these experiments.

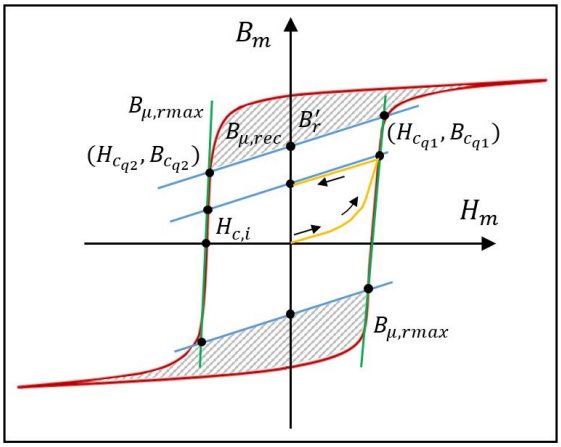

Fig. 9. Typical up-step Envelope tuning loop. First-quadrant intersect points appear closer to the top of the major BH-curve when compared to second-quadrant intersections, limiting the useable air-gap flux density.

5.1 Dynamic-gap experimental Setup

In this research, the same dynamic air-gap setup has been used as previously introduced in chapter 3, as shown in figure 10. Setup dimensions have previously been summarized in table 1.

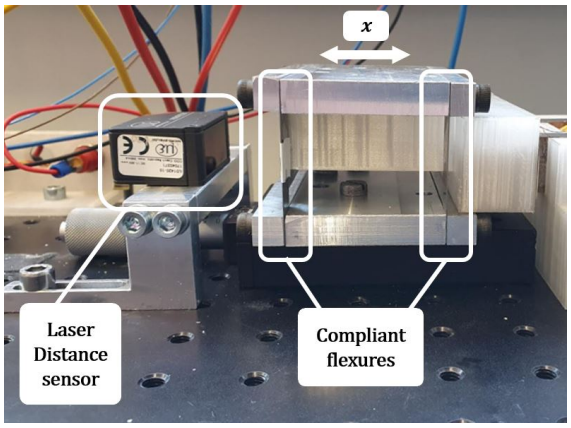

Fig. 10. Side-view of the dynamic stage module, installed on top of the manual linear precision stage.

This setup uses the same sensor equipment, controllers and movement stage as introduced previously. Compliant flexure dimensioning is summarized once more in table 2.

5.2 Mover dynamics

It was mentioned previously that one of the expected benefits of using the MMST method is that it eliminates the initial peak in magnetic flux density - caused by saturation of the circuit with the SMST method. This effect is demonstrated in figure 11. We notice that the saturation tuning method provides almost 791 μm of peak displacement, which corresponds very well with the 832 μm that was estimated in section 2.1. Conversely, the envelope tuning method only displays a peak displacement of roughly 126 μm -a reduction in maximum displacement of almost six times.

Table 2. Measured and obtained flexure parameters

Symbol	Value	Comment
Flexures (Hardened spring steel)		
n_f	4	Number of flexures
l_f	30 mm	Free-moving length
t	0.4 mm	Thickness
b	12.7 mm	In-plane width
E	180 GPa	Young's modulus

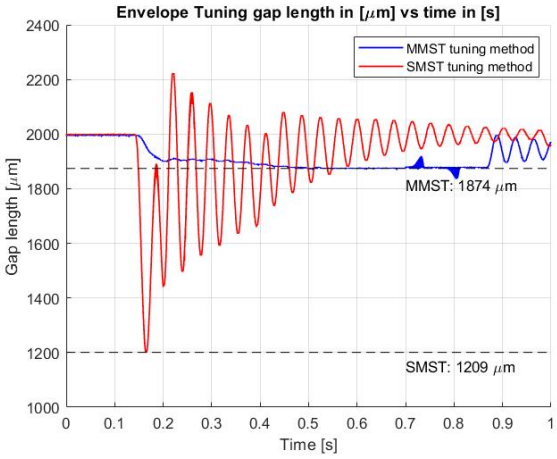

Fig. 11. Experimental results show that the MMST method - in blue - causes significantly less disturbance to the mover when compared to the SMST method.

In figure 11, we can see that after this initial SMST saturation step, the system oscillates quite heavily and with considerable settling time - eventually reaching a final stroke of 39 μm once the tuning process has settled. These characteristics are undesirable in a precision mechanical system. Comparatively, the MMST method displays very little oscillations during the tuning process, with very minor disturbance afterwards. The reduction in disturbance creates several benefits. First of all, a reduced amplitude of displacement causes settling times to decrease - ensuring that the system reaches the desired position sooner. Additionally, the reduced movements cause less strain in the mechanical components of the system - such as the flexures. Lastly, we can consider the air-gap length. We observed in section 2.1 that an initial air-gap length of 1000 μm would be insufficient for the SMST method, as the maximum displacement at saturation was predicted to be close to 1135 μm - indicating that the actuator would shut completely. This could cause concerns for damage and wear of components - negatively influencing actuator life-time expectancy. Therefore, the SMST method can only feasibly operate for larger air-gaps, causing the maximum achievable air-gap flux density to decrease - in accordance with the load-line equation as introduced in chapter 3:

$$B_m = -\mu_0 \cdot \frac{k_1}{k_2} \frac{A_g l_m}{2 A_m l_g} \cdot \left(H_m - \frac{nI}{l_m} \right) \tag{21}$$

Contrary to this, the MMST method can operate at air-gap lengths in the order of 200 to 300 μm without shutting completely - improving the achievable air-gap flux density range. As a result, the initial loss in air-gap magnetization range as discussed in figure 9 can be compensated by reducing the air-gap length of the circuit, with improved system dynamics.

5.3 Tuning time

Removing the saturation peak from the tuning cycle means that the time required for execution of this step can be eliminated. With the tuning times used in this research, the time-related gains are minimal: 50 *ms* removed from a total of 575 *ms* yields a 8.7 % reduction of cycle tuning time. In this instance, most of the time gains are obtained by the reduced dynamic system settling time - as elaborated in the previous section.

If we were able to achieve the minimum tuning times mentioned before in section 2.2, however, larger improvements can be expected. In this case, saturation requires at least 24 *ms* of tuning time from a total cycle of 56 *ms*. Eliminating the saturation step yields a 42.9 % reduction in total tuning time - almost halving the time required for a total tuning cycle when compared to saturation tuning method. Therefore, the improved tuning time of envelope tuning method becomes more pronounced with improvements in control bandwidth.

5.4 Energy loss

Directly related to the tuning time is the amount of energy used by the system. In section 2.3, the contribution of each of the tuning steps to the total energy consumed has been discussed. It was shown that the power consumed during the saturation step could reach ten times that of the demagnetizing step - due to the high coil current required for saturation. So, although currently the saturation step is very short when compared to the demagnetizing step, this results in an almost equal contribution to the total amount of energy used for TM state magnetization. Therefore, even when whe sustain the relatively long 500 *ms* demagnetizing time, we can already halve the total amount of energy emitted through Joule heating by eliminating the saturation step from the tuning sequence. As demagnetizing step times decrease, however, the energy consumption can be reduced even more, as we will discuss later.

Additionally, the hysteresis loss of the TM system can also be reduced by switching from saturation to envelope tuning. The reason for this is the reduced length of the path along the BH-curve: we no longer need to trace it all the way to saturation and back into the second quadrant - encompassing both the first and second quadrant as surface area. Instead, the worst-case tuning step would revolve around the step from $B_m = 0T$ to $B_m = B_r$ - a step to the magnet's saturation remanent flux density. Even in this case, the total hysteresis loss concerns only quadrant 1, meaning that hysteresis losses can at least be halved by using this method - providing even more gains for smaller tuning steps. Although hysteresis loss remains relatively small compared to Joule heating at long tuning intervals - respectively 0.29 J versus 18.37 J for saturation tuning - the effect becomes more pronounced as tuning times are decreased and Joule heating loss dwindles. An more extensive comparison of energy consumption is provided in section 6.1.

5.5 Accuracy and repeatibility

Tuning accuracy and repeatibility of the MMST method can be compared to the SMST method, and is summarized in table 6.

Table 3. Measured air-gap flux density tuning performance comparing the SMST and MMST methods. All figures obtained with $N = 25$ measurement runs, for starting $l_g = 2000 \mu m$. DRS, DA and FF compensation on, moving air-gap.

$B_g[mT]$	$Measured[mT]$	$MAE[mT]$	$3\sigma[mT]$
SMST method			
50	43.25	6.75	0.75
25	17.61	7.39	0.70
MMST method			
50	60.99	10.99	0.30
25	35.28	10.28	0.90

We can see from table 3 that in its current state, 3σ repeatibility appears to be largely unaffected by changing from the SMST to MMST method. However, MMST performs worse than SMST in MAE accuracy at large dynamic air-gaps. This reduction in air-gap flux density accuracy causes the position error to increase from approximately 0.67 to 1.55 μm, as determined by using equation (22):

$$\Delta x_{MAE} = \frac{(MAE)^2 A_g}{\mu_0} \frac{l_f^3}{2Ebt^3} \tag{22}$$

The discrepancy between the proposed minor and established major loop tuning methods can most likely be attributed to an observed difference in first quadrant recoil-line slope when compared to second quadrant slopes. Additionally, it is believed that following minor loops can cause an error in adequate corner-point prediction. Currently, the corner-point is predicted based on the intersect between the recoil-line and major BH-curve. It might be beneficial to find compensation methods that estimate the minor-loop intersects, increasing tuning accuracy.

An overview of the accuracy and repeatibility performance comparison between the SMST and MMST method can be summarized in table 4.

Table 4. Relative performance comparing SMST and MMST methods. Conditions: starting $l_g = 2000\mu m$, DRS, DE and FF compensation on. Lower is better.

Area of Improvement	SMST baseline	MMST difference
Max. Deflection	791 μm	-84.1%
Tuning Times	575 ms	-9.7%
Energy Used	18.37 J	-51.3%
Accuracy (MAE)	7.1 mT	+50.4%
Repeatibility (3σ)	0.7 mT	-17.3%

Evaluating the MMST method performance for five areas of improvement, we can distinguish the largest performance gain in peak system deflection. The largest hit to performance is currently taken in MAE tuning accuracy, but might be overcome using the improved corner-point prediction methods suggested previously. Lastly, major improvements can still be made with tuning time and energy loss by introducing high-bandwidth control. If this is done, the MMST advantage can be expected to reduce tuning times by up to 43.9 % when compared to SMST. Energy loss might experience the largest improvement: with up to 95.2% expected reductions. In the optimal case with 24 *ms* of saturation, the large power draw causes a minimum energy loss of 4.49 *J* due to Joule heating. Comparing this with the 12 *ms* demagnetizing step losing only 0.168 *J* - we can see that the advantage increases with shorter tuning times.

6 Experimental validation of BTI

Previously in section 3, the analytical calculation of the BTI was introduced. This metric can also be experimentally validated - making use of measured energy losses with the moving air-gap TM experimental setup.

6.1 SMST method BTI Validation

Used in the experimental setup is a current sensor, which allows the user to measure the current that is supplied to the coil at all times. We can use this measurement to calculate the power draw and thus TM energy loss at each sampling time instance by using:

$$E_{TM} = \int_0^{T_{sample}} I^2 R dt \tag{23}$$

Here, T_{sample} equals $1 \cdot 10^{-4} s$, governed by the NI DAQmx module used in this research - which is set to a sampling speed of 10 kHz. I is the value logged by the current sensor and R the coil resistance as introduced in table 1. Added to this is the estimated worst-case hysteresis loss - as calculated before using equation (12). The measurements are carried out for gap magnetization levels of B_g = 25, 50 and 75 mT, with demagnetization tuning times of T_{demag} = 500, 250 and 100 ms. Saturation tuning time is kept constant at 35 ms. Results are summarized in table 5.

Table 5. Measured TM saturation method energy usage for varying B_{gap} and T_{demag} values. All figures obtained with $N = 25$ measurement runs, for $l_g = 2000\mu m$. DRS, DA and FF compensation on, $T_{sat} = 35ms$.

SMST Method BTI

B_g $[mT]$	Energy $[J]$	EM Power $[Js^{-1}]$	BTI $[s]$	Error $[\%]$
T_{demag} **= 500 ms**				
75	15.29	0.45	34.21	3.4
50	16.25	0.20	81.76	2.6
25	16.79	0.05	337.85	6.1
T_{demag} **= 250 ms**				
75	10.43	0.45	23.34	8.2
50	10.74	0.20	54.08	5.4
25	11.37	0.05	228.68	0.0
T_{demag} **= 100 ms**				
75	7.70	0.45	17.24	11.2
50	7.69	0.20	38.72	11.4
25	7.80	0.05	156.85	10.2

Reviewing the results shown in table 5, we notice that for varying levels of B_g, energy loss does not change that much. For example, at 500 *ms* demagnetizing time, the difference between 25 and 75 mT is only 1.5 J. However, the power usage of EM actuators scales quadratically with B_g, which causes the low power draw observed for gap magnetization levels of 25 mT. In turn, the BTI values for low gap-magnetization become very large - which favors the use of the EM actuator for these cases. As expected, the BTI values decrease significantly with reduced demagnetzation tuning times, to as low as $T_{be} = 17.24s$ at T_{demag} = 100 ms and $B_g = 75mT$. Lastly, we can distinguish with decreasing demagnetization times an increasing error between predicted and measured BTI. This can be partly attributed to a decrease in tuning accuracy with decreased tuning times, as can be demonstrated by table 6.

Table 6. Measured air-gap flux density tuning performance for decreased tuning times. All figures obtained with $N = 25$ measurement runs, for $l_g = 1000\mu m$. DRS, DA and FF compensation on. Static setup.

SMST Method tuning time vs MAE **and** 3σ

$B_g[mT]$	$MAE[mT]$	$3\sigma[mT]$
T_{demag} **= 500 ms**		
125	2.28	0.34
75	2.17	0.78
25	2.28	0.87
T_{demag} **= 250 ms**		
125	1.02	1.40
75	0.92	1.36
25	5.71	4.70
T_{demag} **= 100 ms**		
125	10.56	5.95
75	12.72	13.50
25	44.21	16.89

Recorded in table 6 is the performance of the SMST method for different tuning times. We can see that decreasing the demagnetization tuning time from 500 *ms* to 100 *ms* causes significant performance loss, both in *MAE* accuracy and 3σ repeatibility. This can be attributed to the limitations of the currently used hard-and software. Upgrading the setup to an FPGA-based platform could already greatly improve control bandwidths, which in turn is expected to yield better performance at short tuning times.

6.2 MMST method BTI Validation

Similar to the SMST method, we can execute BTI-experiments for the proposed MMST method, summarizing the results in table 7.

Table 7. Measured MMST method energy usage for varying B_{gap} and T_{demag} values. All figures obtained with $N = 25$ measurement runs, for $l_g = 2000\mu m$. DRS, DA and FF compensation on. Dynamic setup.

MMST Method BTI

B_g $[mT]$	Energy $[J]$	EM Power $[Js^{-1}]$	BTI $[s]$	Error $[\%]$
T_{demag} **= 500 ms**				
75	12.33	0.45	27.59	15.4
50	9.59	0.20	48.26	1.3
25	5.86	0.05	117.90	20.6
T_{demag} **= 250 ms**				
75	5.61	0.45	12.54	7.36
50	3.82	0.20	19.20	9.7
25	2.55	0.05	51.32	46.6
T_{demag} **= 100 ms**				
75	2.35	0.45	5.27	41.7
50	1.60	0.20	8.04	44.1
25	0.76	0.05	15.29	37.1

Contrary to the SMST method, we see that with a change in magnetization level comes a large change in MMST method energy loss. Additionally, higher levels of magnetization now lose more energy when compared to lower levels, whereas SSMT method shows the opposite trend. This can be explained by the tuning approaches: the single up-step MMST method takes larger steps for higher magnetization levels, thus requiring more magnetizing current which yields greater energy loss. On the other hand, SMST method approaches the corner-point from opposite direction, thus making small magnetization levels more prone to losses. Similar to SMST method, we see that BTI values decrease for increased magnetization level, and estimator errors increase with a decrease in tuning times. The larger discrepancies in estimator error for this method align with the increased MAE and 3σ values discussed before in section 5.5.

6.3 Measured Efficiency Gain

The efficiency gain can be calculated by comparing the energy usage between tables 5 and 7. We can calculate the percentage gained from switching from SMST to the MMST method by evaluating:

$$\eta_{gain}(\%) = -\frac{E_{env} - E_{sat}}{E_{sat}} \cdot 100\% \tag{24}$$

Efficiency gains can then be summarized in table 8.

Table 8. Measured MMST method efficiency gain over the SMST method, for varying B_{gap} and T_{demag} values. All figures obtained with $N = 25$ measurement runs, for $l_g = 2000\mu m$. DRS, DA and FF compensation on. Dynamic setup.

MMST Method Efficiency improvements

B_g $[mT]$	SMST Energy $[J]$	MMST Energy $[J]$	Efficiency gain $[\%]$
T_{demag} **= 500 ms**			
75	15.29	12.33	19.4
50	16.25	9.59	41.0
25	16.79	5.86	65.1
T_{demag} **= 250 ms**			
75	10.43	5.61	46.2
50	10.74	3.82	64.4
25	11.37	2.55	77.6
T_{demag} **= 100 ms**			
75	7.70	2.35	69.5
50	7.69	1.60	79.2
25	7.80	0.76	90.3

From table 8, it becomes apparent that for the measured states, efficiency improved by at least 20 % in the worst case to 90% in the best case. Lower B_g and T_{tune} values both positively influence the efficiency gain of MMST method when compared to the SMST method.

6.4 BTI projections

In order to project future developments in Tunable Magnet control, we can extrapolate the trends observed in the tables shown in sections 6.1 and 6.3. We can determine the projected BTI for tuning times smaller than 100 *ms*, where T_{tune} is evaluated up to the theoretical limits of the magnetic circuit used in this research, as calculated per equations (9), (10) and (11):

1. **Saturation:** 24 *ms*
2. **Demagnetizing:** 12 *ms*
3. **Decay:** 20 *ms*

Evaluating this using $B_g = 50mT$ for both the SMST and MMST method, figure 12 emerges.

Figure 12 suggests an increased advantage for MMST at smaller tuning times. The projected BTI for $B_g = 50mT$ at the lowest possible tuning times is projected to be approximately 3.57 *s* for SMST tuning, and 0.95 *s* for MMST tuning - making the system suitable for 1 Hz operation.

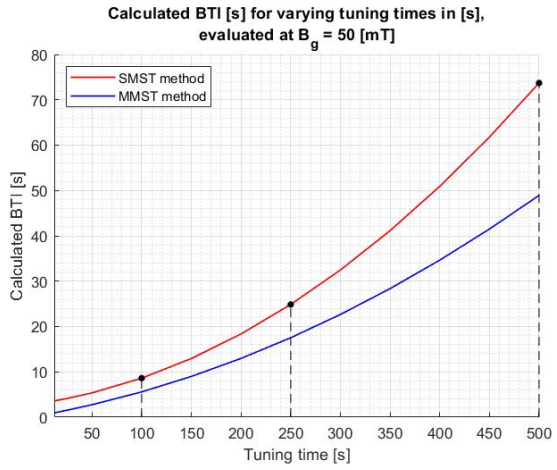

Fig. 12. Calculated progression of BTI times when subjected to increasing demagnetizing tuning times. Evaluated for $l_g = 2000\mu m$, $B_g = 50mT$ and $T_{sat} = 35ms$.

Air-gap magnetization of 50 mT can - however - be considered the lower-end of the achievable gap flux density values, which range from 25 to 175 mT. As demonstrated in tables 5 and 7, TM actuators are disadvantaged compared to EM actuators at these lower magnetization levels. Evaluating the lowest possible tuning times for the entire range of achievable B_g levels, we arrive at figure 13.

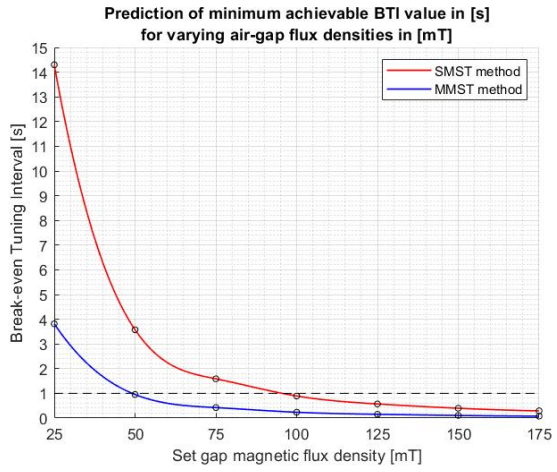

Fig. 13. Estimated maximum achievable performance of the currently explored tuning methods and setup topology. Tuning times are minimized, B_g is evaluated from 25 to 175 mT.

From figure 13, we can recognize an exponential reduction of BTI times for both the SMST and MMST method - favoring TM over EM actuators for larger values of B_g. As previously discovered when comparing tables 5 and 7, we recognize the advantage of using MMST over the SMST method for smaller values of B_g. Indicated with the horizontal striped line in figure 13 is the sub-1 Hz operation threshold.

With currently available predictions and circuit dimensions, the system is estimated to achieve this for the range of 50 to 175 mT using MMST tuning, and she slightly more narrow 100 to 175 mT range using SMST. Ultimately, both tuning methods reach their estimated smallest BTI values at 175 mT, with SMST tuning at 0.29 s (3 Hz) and MMST tuning at 0.08 s (12 Hz) interval times.

7 Conclusion

In this paper, a tuning algorithm based on the MMST method has been implemented into the control software - alongside the pre-existing SMST method. Capable of calculating the magnetizing corner-point in both quadrant 1 and 2 - making use of the AlNiCo 5 minor hysteresis loops - it circumvents the need for a saturation step within the tuning cycle. Performance improvement was expected to be in the form of reduced peak mover displacement, tuning time and energy loss. Tuning accuracy and repeatability were also compared between the two methods.

In line with analytical calculations, it was observed that peak mover displacement during saturation reached almost 800 μm at an initial air-gap length of 2000 μm. On the other hand, the MMST method required significantly less magnetizing voltage when compared to the saturation step, yielding in a peak displacement of just under 130 μm - a reduction of more than six times. Therefore, the MMST method appears to greatly improve dynamic performance of the actuator.

In the SMST tuning method, saturation makes up only 10 % of the total tuning time. If one were to be able to reduce the tuning times to the theorized minimum for this actuator, this would be almost half. Excluding saturation by using the MMST method naturally means that tuning times theoretically could be halved in comparison to the SMST method. For this to happen, however, major improvements in control bandwidth must first be achieved, making the tuning time performance gain at this point in time quite insignificant, but promising in future developments.

It was estimated that the short saturation step would consume approximately the same amount of energy as said demagnetizing step, caused by the comparatively large power draw required to sustain the saturation current. Practical experiments proved this to be true. At 500 ms demagnetizing time, energy loss reduction by using the MMST method would range between 20 and 65 %. For shorter tuning times, this advantage grew even larger, peaking between 70 and 90% reduction in energy loss at 100 ms demagnetizing time.

MMST repeatability was measured to range between 0.30 and 0.90 mT - very similar to the 1 mT performance range of the SMST method. The MAE, however, increased significantly - by 1.5 times when compared to the SMST method. This can probably be attributed to incorrect first-

quadrant corner-point estimations. For applications where tuning accuracy is paramount, the MMST tuning method is not yet mature enough. For most other applications - due to excellent repeatability combined with very favorable benefits in dynamic performance and reduced energy loss when compared to SMST - the MMST already provides a great advantage over the established tuning method.

The BTI has been validated for both the SMST and MMST method. Starting with SMST, analytical calculations and experimental results never deviated more than an absolute error of 11% - worsening with decreased tuning times. For the tuning time-scales studied in this research, the BTI calculation therefore appears to be valid. Similarly, the MMST method predictions show adequate similarity to the measured results at tuning times of 500 and 250 *ms*. The discrepancies, however, become larger for small magnetization levels and short tuning times - indicating an error in the BTI prediction. This can partly be attributed to the worsened tuning accuracy of the MMST method: the MMST BTI prediction is in theory already more subjective to errors in magnetization current - and thus in BTI - when compared to SMST prediction.

Extrapolating the BTI prediction results obtained from this research gives an idea of what might be possible in future work. Based on this, it is believed that the SMST method - if tuning times of this circuit can be reduced to the theoretical minimum - is capable of achieving a BTI between 1 and 0.29 s for a tuning range from 100 to 175 mT, making the system suitable for 1 to 3 Hz operation. More promising is the MMST method. At minimal tuning times, this method is projected to reach a BTI in the order of 1 to 0.08 s for a tuning range of 50 to 175 mT - rendering it usable for up to 12 Hz operation.

It is therefore recommended for future work to improve the accuracy and repeatability of the Minor-loop Magnetization State Tuning method. Investigating other causes of corner-point discrepancies, such as minor loop nonlinearities and first-quadrant recoil-line slope differences, might already solve most of the inaccuracies observed here. Regarding tuning speed, replacing the currently used DAQmx USB module with an FPGA-based platform - such as CompactRIO is advised. By doing this, control bandwidth and tuning speeds can be substantially increased - greatly reducing energy loss. Additionally, it is recommended to expand the operating principles of the MMST control method - which is currently only equipped to make large tuning steps, typically observed with large amplitudes. In order to also catch the high-frequency low-amplitude operations, we could use control similar to EM actuators in parallel: by continuously altering small currents along the recoil-lines. This will further improve the BTI performance of the TM actuator.

References

[1] Lomonova, E. A., 2010. "Advanced actuation systems - State of the art: Fundamental and applied research". *2010 International Conference on Electrical Machines and Systems, ICEMS2010*, pp. 13–24.

[2] Hüfner, T., Radler, O., Ströhla, T., Sattel, T., Wesselingh, J., Vogler, A., and Eicher, D., 2017. "A note on electromagnetic gravity compensation actuators based on soft electro-permanent magnets for adjustable reluctance force". *Proceedings of the 17th International Conference of the European Society for Precision Engineering and Nanotechnology, EUSPEN 2017*(May), pp. 149–150.

[3] Philips Innovation Services, 2016. "Comparative evaluation of Lorentz and reluctance actuators". pp. 1–3.

[4] Vrijsen, N. H., Jansen, J. W., and Lomonova, E. A., 2010. "Comparison of linear voice coil and reluctance actuators for high-precision applications". *Proceedings of EPE-PEMC 2010 - 14th International Power Electronics and Motion Control Conference*(October).

[5] Munnig Schmidt, R., Schitter, G., Rankers, A., and Van Eijk, J., 2014. *The Design of High Performance Mechatronics*, 2nd revise ed. Delft University Press - IOS Press BV, Amsterdam.

[6] Knaian, A., 2010. "Electropermanent magnetic connectors and actuators : devices and their application in programmable matter". PhD thesis, Massachusetts Institute of Technology.

[7] Campbell, P., 1994. *Permanent Magnet Materials and their Application*. Cambridge University Press.

[8] Parker, R., 1990. *Advances in Permanent Magnetism*. John Wiley and Sons, Inc.

[9] Roters, H., 1941. *Electromagnetic Devices*, first edit ed. John Wiley and Sons, Inc., New York.

[10] Viëtor, S. G., 2018. "Tunable Magnets: Modeling and Validation for Dynamic and Precision Applications". PhD thesis.

[11] Eclipse Magnets, 2017. "Alnico Magnets Datasheet". pp. 5–8.

[12] National Instruments, 2021. "USB-6351X DAQmx module". *url: https://www.ni.com/nl-nl/shop/hardware/products/multifunction-io-device.html?modelId=124936*(accessed: 29-07-2021).

[13] National Instruments, 2021. "CompactRIO FPGA module". *url: https://www.ni.com/nl-nl/shop/compactrio.html*(accessed: 29-07-2021).

5

Conclusions and Recommendations

5.1. Conclusions

We revisit the main goal of the Tunable Magnet actuator research program, which has been defined as:

Develop a Tunable Magnet that can be robustly tuned in the presence of a dynamically varying air-gap and investigate its use in precision actuation systems.

With the help of our objectives, we can draw the following conclusions from the research.

Design and build a demonstrator capturing the true movements of a moving TM actuator

The existing TM actuator experimental setup was incapable of delivering free motion as the mover was mounted on a manual linear precision stage. In practical actuators, the air-gap length changes when a current is applied to the magnetizing coil. In order to emulate the dynamic behaviour of a gap-closing reluctance actuator, a 4-member compliant flexure topology was designed and built. Although this research used hardened spring steel flexures with a thickness of 0.4 mm, the components can be interchanged - allowing for more extensive experimentation in the future. The movement stage initial air-gap length can be precisely set by utilizing the pre-existing manual linear precision stage, while the modular flexure stage adds dynamic motion during actuator operation.

In conjunction with the stage, the integration of a laser triangulation distance sensor now allows the user to read out motion stage displacements. This made it possible to study the dynamic behaviour of the motion system when subjected to both the SMST and MMST tuning algorithms. Lastly, because displacements can now be measured, the position and flux feedback data can be used in parallel to refine the calculations of the proposed compensating techniques - improving robustness, accuracy and repeatability of the tuning method.

Increase robustness and performance of the magnetization state tuning algorithm

It is important that the TM actuator allows for robust, accurate and repeatable tuning performance within a broad range of dynamic air-gap lengths. For this reason, the SMST method had to be expanded in order to account for continuous non-constant recoil-line slopes, dynamically changing air-gap length and accompanying fringe flux-loss effects. Additionally, a PI flux-feedback controller was programmed in parallel to the standard inverse controller. The static-gap performance contributions of the four compensation methods are summarized below.

- **Dynamic Recoil-line Slope (DRS) compensation**
  Rewriting the existing DRS compensation method to a continuous analytical equation allowed for easy substitution into the corner-point magnetization algorithm. In turn, the user no longer needs to use a look-up table in order to find the corner-point magnetization corresponding to the desired air-gap magnetization. The DRS method significantly increases tuning performance, displaying between 8.8 to 78.5 % reduction in MAE - improving accuracy - and up to 33.6 % gains in 3σ repeatability. Because of this, MAE and 3σ remain below 2.3 and 0.9 mT respectively at baseline 1000 μm air-gap length. It can

therefore be concluded that due to better corner-point approximation by DRS compensation significant performance improvements are provided in both accuracy and repeatability, with little sacrifice in computation effort - making the implementation worthwile.

- **Dynamic Air-gap (DA) compensation**
  Using the air-gap measurements of the laser triangulation distance sensor, DA compensation continuously updates the values for l_g in corner-point and gain computations. Adding DA to the DRS compensation method enabled up to 50 % MAE reduction for air-gap lengths smaller than the 1000 μm baseline value. For large values of l_g, the compensator appeared to overshoot - causing an increase in MAE of up to 7.5 % at 1500 μm. Conversely, repeatability 3σ appeared to improve across the board - ranging from 37.1% at 1200 μm to 77.2% at 1500 μm. In conclusion, the addition of DA compensation only appears to provide minor improvements to MAE reduction, whilst significantly improving 3σ repeatability. Meanwhile, the computation cost is increased due to the introduction of gap length measurements - making it difficult to justify implementation.

- **Fringe Flux-feedback (FF) compensation**
  Introducing FF to DA and DRS compensation, the tuning performance stabilizes for all gap lenths considered in this research. The combination of FF and DA compensation more dan halves the MAE error at 1500 μm, and across the entire range MAE no longer exceeds 5 mT - making the system very stable. repeatability performance also sees great improvements, with 3σ values never exceeding 1 mT - for all air-gap lengths. In conclusion, DA and FF need to be used in tandem in order to ensure stabilized tuning control. Adding both to the system adds computational stress due to the use of real-time l_g measurements, but the excellent robustness and tuning performance make up for this.

- **Parallel PI (PPI) flux control**
  Placing a PI flux-feedback controller in parallel with the inverted controller yields some mixed results. On one hand, MAE can be reduced significantly - with up to 75% improvement recorded for 25 mT gap magnetization at $l_g = 1000\mu m$. On the other hand, 3σ appears to worsen across the entire range of magnetization levels - almost doubling for values of 25 and 75 mT. Still, repeatability remains within 2 mT at all times, so some aplications the potential MAE error reduction might outweigh the reduction in 3σ repeatability. The PI controller used in this research has not been tuned to perfection, which might have aided in the reduction in stability. In conclusion, PPI control shows promising results, but with the currently observed instabilities it is deemed not ready for implementation just yet.

Next to static-gap performance contributions, we can compare accuracy and repeatability each of the compensators during dynamic-gap operation. Dynamic results are summarized once more in table 5.1.

Table 5.1: Measured dynamic air-gap flux density tuning performance improvements for invividual compensators. All figures obtained with $N = 25$ measurement runs, for $B_g = 50mT$ and $t_{tune} = 500ms$.

Compensation method	MAE $[mT]$	Δx_{MAE} $[\mu m]$	Position Improvement	3σ $[mT]$	$\Delta x_{3\sigma}$ $[\mu m]$	Position Improvement
None (reference)	19.18	5.58	-	2.38	85.9e−3	-
DRS	8.72	1.15	79.4 %	1.92	55.9e−3	34.9 %
DRS, ED & FF	7.55	0.86	84.6 %	0.78	9.2e−3	89.3 %
DRS, ED, FF & PPI	6.75	0.69	87.6 %	0.75	8.5e−3	90.1 %

At a large air-gap length of 2000 μm, the actuator cannot be used without compensation methods. With almost 20 mT tuning error at 50 mT setpoint, the corner-point prediction seems to be way off - which is also reflected by an unusable 5 μm position error. The problem with accuracy can be easily solved by adding DRS compensation on top. This way, Δx_{MAE} is reduced by almost five times to just over 1 μm, with a third reduction in $\Delta x_{3\sigma}$ - down to 56 nm. Similar to static gap experiments, adding ED and FF compensation on top significantly imroves stability and thus position repeatability - which is now improved by almost ten times to less than 10 nm. The introduction of PPI control in dynamic operation yields a slight improvement in both MAE and 3σ performance, but not enough to warrant full implementation. Perhaps with improved controller tuning, this contribution can be improved.

To summarize, the implementation of DRS, ED and FF compensation results in excellent improvements - up to ten times in both position accuracy and repeatability. PPI control can potentially be used to squeeze out a bit of extra performance, but in its current state the contribution is too weak when compared to the computational load it adds to the system.

Introduce a novel Minor-loop Magnetization State Tuning (MMST) method in order to increase the energy efficiency and dynamic behaviour of the TM actuator

A tuning algorithm based on the MMST method has been implemented into the control software - alongside the pre-existing SMST method. Capable of calculating the magnetizing corner-point in both quadrant 1 and 2 - making use of the AlNiCo 5 minor hysteresis loops - it circumvents the need for a saturation step within the tuning cycle. Performance improvement was expected to be in the form of reduced peak mover displacement, tuning time and energy loss. Tuning accuracy and repeatability were also compared between the two methods.

- **Peak mover displacement**
  With the introduction of a moving stage and laser triangulation distance sensor, it was made possible to directly measure the position of the mover at all times during the tuning cycle. During the experiments, it was observed that - in line with analytical calculations - peak mover displacement during saturation reached almost 800 μm at an initial air-gap length of 2000 μm. On the other hand, the MMST method required significantly less magnetizing voltage when compared to the saturation step, yielding in a peak displacement of just under 130 μm - a reduction of more than six times. Therefore, the MMST method appears to greatly improve dynamic performance of the actuator.

- **Tuning time**
  In this research, tuning times in the SMST sequence were divided as follows: saturation required 50 ms, demagnetizing 500 and decay another 25. This way, the exclusion of saturation allows for only 10 % reduction of the total tuning time. If one were to be able to reduce the tuning times to the theorized minimum for this actuator - respectively 24, 12 and 25 ms - total tuning time within the MMST method could be halved in comparison to the SMST method. For this to happen, however, major improvements in control bandwidth must first be achieved, making the tuning time performance gain at this point in time quite insignificant, but promising in future developments.

- **Energy loss**
  It was estimated that the short saturation step would consume approximately the same amount of energy as said demagnetizing step, caused by the comparatively large power draw required to sustain the saturation current. Practical experiments proved this to be true. At 500 ms demagnetizing time, energy loss reduction by using the MMST method would range between 20 and 65 %. For shorter tuning times, this advantage grew even larger, peaking between 70 and 90% reduction in energy loss at 100 ms demagnetizing time. Thus, it can be concluded that the MMST method provides significant improvements in this area - which will only increase with reductions in tuning time.

- **Accuracy and repeatability** Where the MMST method appears to be very advantageous in the areas described above, the same cannot yet be said for accuracy and repeatability. MMST repeatability was measured to range between 0.30 and 0.90 mT - very similar to the 1 mT performance range of the SMST method. The MAE, however, increased significantly - by 1.5 times when compared to the SMST method. This can probably be attributed to incorrect first-quadrant corner-point estimations. The expected cause of this error will be further explored in the recommendations, but it can be concluded that for applications where tuning accuracy is paramount, the MMST tuning method is not yet mature enough.

The areas of improvement listed above are summarized once more in table 5.2. As mentioned before, the MMST method may not yet be applicable for applications that require the highest level of accuracy. However, due to excellent repeatability combined with very favorable benefits in dynamic performance and reduced energy loss when compared to SMST, the MMST already provides a great advantage over the established tuning method. This advantage can only become greater with future improvements - making it a promising tuning method to further investigate.

Table 5.2: Measured TM envelope method efficiency gain over saturation method, for varying B_{gap} and T_{demag} values. All figures obtained with $N = 25$ measurement runs, for $l_g = 2000\mu m$, recoil, gap and flux compensation on.

MMST method efficiency improvement over SMST method

B_g $[mT]$	SMST Energy $[J]$	MMST Energy $[J]$	Efficiency gain [%]
T_{demag} **= 500 ms**			
75	15.29	12.33	19.4
50	16.25	9.59	41.0
25	16.79	5.86	65.1
T_{demag} **= 250 ms**			
75	10.43	5.61	46.2
50	10.74	3.82	64.4
25	11.37	2.55	77.6
T_{demag} **= 100 ms**			
75	7.70	2.35	69.5
50	7.69	1.60	79.2
25	7.80	0.76	90.3

Achieve experimental validation of the Break-even Tuning Interval (BTI)

The BTI has been validated for both the SMST and MMST methods. Starting with SMST, analytical calculations and experimental results never deviated more than an absolute error of 11% - worsening with decreased tuning times. For the tuning time-scales studied in this research, the BTI calculation therefore appears to be valid. Similarly, the MMST method predictions show adequate similarity to the measured results at tuning times of 500 and 250 ms. The discrepancies, however, become larger for small magnetization levels and short tuning times - indicating an error in the BTI prediction. This can partly be attributed to the worsened tuning accuracy of the MMST method: the MMST BTI prediction is in theory already more subjective to errors in magnetization current - and thus in BTI - when compared to SMST prediction.

Extrapolating the BTI prediction results obtained from this research gives an idea of what might be possible in future work. Based on this, it is believed that the SMST method - if tuning times of this circuit can be reduced to the theoretical minimum - is capable of achieving a BTI between 1 and 0.29 s for a tuning range from 100 to 175 mT, making the system suitable for 1 to 3 Hz operation. More promising is the MMST method. At minimal tuning times, this method is projected to reach a BTI in the order of 1 to 0.08 s for a tuning range of 50 to 175 mT - rendering it usable for up to 12 Hz operation.

5.2. Recommendations

Though the contributions from this research yield an increase in all-round performance from the fundamental work performed by Viëtor in 2018, it does not yet present a complete solution for a practically applicable TM actuator. For this, more research is necessary. Hoping that the work on TM actuators will be continued in the future, some recommendations can be subdivided into three categories:

1. **Improve the accuracy and repeatability of the Minor-loop Magnetization State Tuning method.** Considering the measured and predicted all-round performance advantage of the MMST over the SMST method, it is advised to further develop this tuning method by:
    - Further refining the PPI flux-feedback controller. The current design has not been optimized, so some performance can be gained from here
    - Investigating other causes of corner-point discrepancies, such as minor loop nonlinearities and first-quadrant recoil-line slope differences
    - Refinements to the fringe flux loss (k1) compensator. Currently, an empirical approximation is used, whereas Roters provides analytical alternatives [22].
2. **Increase the flux and position feedback control speed of the Tunable Magnet, using appropriate hard- and software.** Using the DAQmx in combination with LabView has allowed this research to move quickly to experimental validation and testing of new compensation and tuning methods. Having obtained dynamic-gap robustness, now it is time to increase tuning speeds to allow for practical use. This can be done by:
    - Rewriting some of the LabView program from pulse-train waveform generation to sequential control, allowing for faster refresh times.
    - Replacing the currently used DAQmx USB module with an FPGA-based platform - such as CompactRIO. By doing this, control bandwidth and tuning speeds can be substantially increased - greatly improving performance and applicability.
    - Altering the dimensions of the TM setup. With the current setup being quite bulky, tuning times are restricted. The large mass of the mover will cause a low dynamic-system eigenfrequency and the large magnet causes a large inductance, restricting tuning and settling times.
    - Using a charge-in circuit to obtain high tuning voltages. This shortens tuning time significantly, and allows for more accuracy in large air-gaps - where at the time of writing voltage restricts the maximum achievable tuning current.
3. **Investigate how a TM actuator can be used in practice for both low- and high-frequency applications.** With estimations obtained by the BTI calculations, it was estimated that the MMST control method would be limited to 12 Hz operating speeds. In precision engineering, however, disturbance and operating frequencies can be much higher than this. We might be able to achieve high-frequency operating speeds by considering:
    - Switching input parameter. Currently, we set the desired gap flux-density, for which the tuning algorithm decides the appropriate corner-point flux density. In practice, we would like the system input to be desired position, which is then translated into B_g automatically. This should be possible with a few small additions to the analytical calculations.
    - Expanding the MMST control method. Currently, the method is only equipped to make large tuning steps - typically observed with large amplitudes. In order to also catch the high-frequency low-amplitude operations, we could use control similar to EM actuators in parallel: by continuously altering small currents along the recoil-lines.
    - Investigating parallel use of TM and EM actuators. This was also proposed by Viëtor: using a TM actuator for low-frequency high-amplitude and an EM actuator for high-frequency low-amplitude input signals, we obtain the best of both worlds: efficient and broad-range actuator control.

A

Experimental Hardware

A.1. Baseline experimental setup

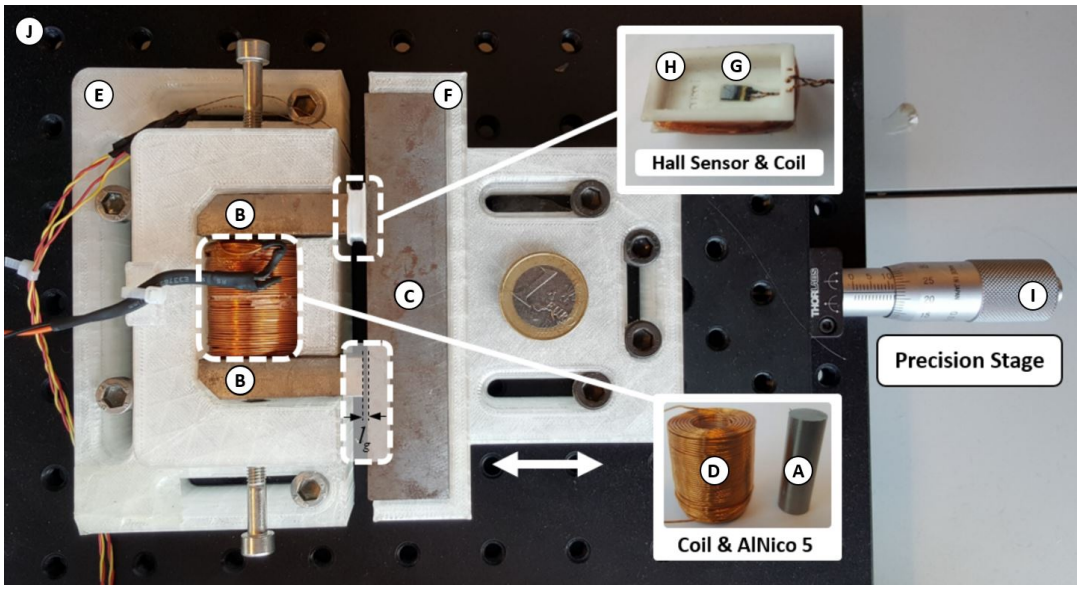

Figure A.1: Top-down detailed view of the original static-gap setup. Components are labeled from A to J, adapted from [26]

Figure A.1 shows a detailed view of the static-gap magnetic circuit as introduced by [26]. Dimensions and characteristics of components A through D are detailed in table A.1.

Magnetic Circuit Dimensions and Parameters				
Parameter	Value	SI Unit	Comment	Source
A: AlNiCo 5 (LNG44, Alcomax) Magnet				
l_m	30.2	$[mm]$	Magnet length	[26]
d_m	9.83	$[mm]$	Magnet diameter	
B_r	1.25	$[T]$	Remanent flux density	Appendix C
H_c	50	$[kAm^{-1}]$	Coercive force	Appendix C
H_s	150	$[kAm^{-1}]$	Saturation field intensity	$3 \times H_c$ [3]
$\mu_{r,max}$	270	$[-]$	Maximum permeability	[3]
B + C: St.37 Magnetic Circuit				
l_p	39.9	$[mm]$	Pole piece length	[26]
w_p	10.0	$[mm]$	Pole piece width	
h_p	20.0	$[mm]$	Pole piece height	
l_k	100	$[mm]$	Mover length	[26]
w_k	20.0	$[mm]$	Mover width	
h_k	20.0	$[mm]$	Mover height	
$\mu_{r,avg}$	1000	$[-]$	Average relative permeability	Appendix C
D: Copper Magnetizing Coil				
l_c	28.2	$[mm]$	Coil length	[26]
d_c	21.5	$[mm]$	Coil outer diameter	
d_w	0.45	$[mm]$	Copper wire diameter	
n	668	$[-]$	Number of coil windings	
ρ_c	2.09e-9	$[\Omega m]$	Copper wire resistance	[26]

Table A.1: Summarized magnetic circuit dimensions and parameters - components (A - D) - adapted from [26].

Components A to D are fixed into 3D-printed PMMA components E and F. Hall sensor bracket H can be slid over pole piece B, with the Hall sensor G glued onto H. Hall sensor properties are summarized in table A.2, the extended datasheet can be found in appendix C. The sense coil as shown in figure A.1 has never been implemented - because the Hall senso alone provided adequate performance. Stator bracket E is bolted directly to I - a Thorlabs optical breadboard [24], which serves as the base for the full experimental setup. Between mover bracket F and base I, a Thorlabs manual precision linear stage, providing 25 mm of accurate linear motion [25]. This way, the air-gap length can be set to the desired value - but remains static during operation.

Parameter	Value	SI Unit	Comment	Source
F: Hall sensor				
Range	± 1.5	$[A]$	Calibrated range	[26]
Sensitivity	5.13	$[TV^{-1}]$	Measured sensitivity	[26]
Resolution	sub-1	$[mT]$	Datasheet resolution	Appendix C
Bandwidth	100	$[kHz]$	Communicated with supplier	[26]

Table A.2: Hall sensor summarized properties, adapted from [26].

If we zoom out from the magnetic circuit overview as presented in figure A.1, we can also consider the eletronics that drive the magnetizing coil. Schematically, the setup can be represented by figure A.2. The AlNiCo 6 subsystem was built previously by [26], but has not been used in this research. Therefore, the setup can be broken down into three subsystems: power management, sensors and signal conditioning and data log/send.

A.1.1. Power management

In order to accomodate AlNiCo magnet saturation, a supply voltage of $\pm 30V$ is required [26]. Two Delta Elektronica ES 030-10 $30V/10A$ DC power supplies are used in parallel, in order to deliver both positive and negative voltage and current to the magnetizing circuit. Additionally, a $\pm 15V$ board conditioning voltage is required to provide current for the Hall sensor and signal conditioning board. The Delta Elektronika D1D

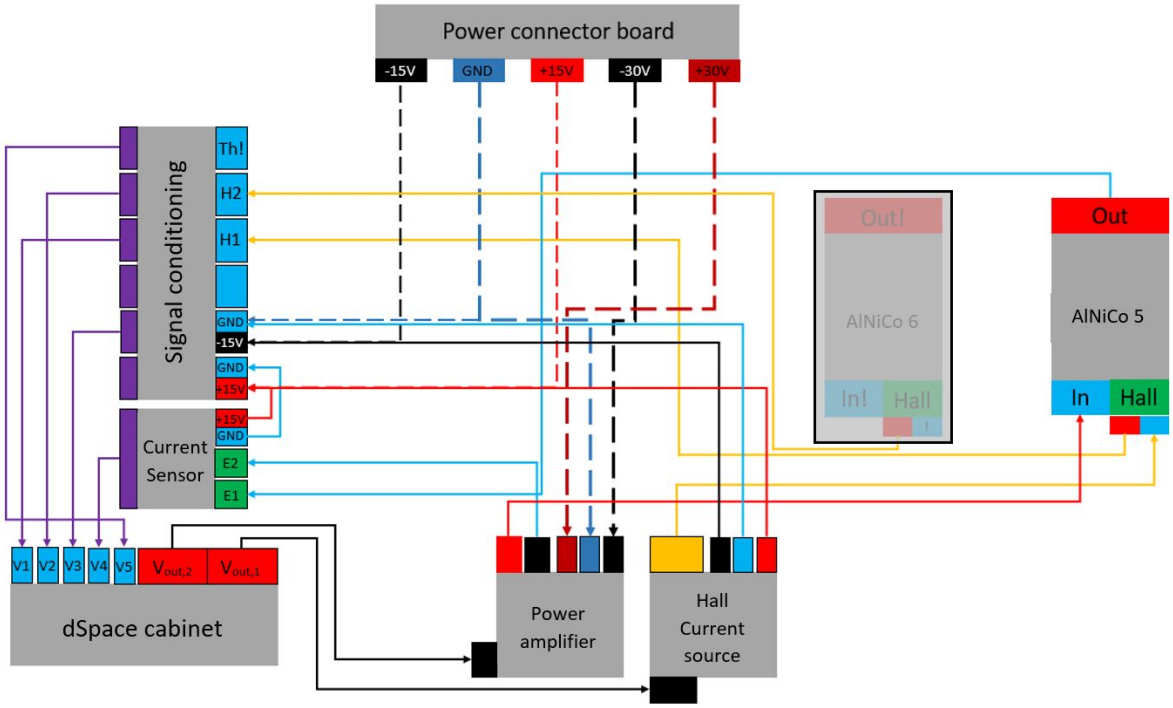

Figure A.2: Schematic wiring overview of the AlNiCo 5 TM setup. Power connector board connects the power supplies with the setup, signal conditioning filters incoming data and sends it to the dSpace cabinet. Hall sensor is conditioned by the Hall current source, power amplifier sends the voltage signal to the magnetizing coil, the current of which is measured by the current sensor.

$15V/1A$ power supply is used to provide this. Power supply specifications can be accessed via [6] and [7], all three cabinets are depicted in figure A.3a.

The $\pm 30V$ source is hooked up to a custom linear power amplifier - making use of the TI OPA549 OpAmp [26]. The amplifier is connected to a PCB and large heat sink, as shown in figure A.3. The amplifier translates the input signal as determined by the tuning algorithm to a coil saturation voltage, and serves as the intermediate step between the data log/send devide and power supplies. Output figures are: $\pm 8A/25V$, resulting in an amplifier gain of 3. Schematics are supplied in appendix C.

The $\pm 15V$ source is hooked up to both the hall current sensor source. Additionally, it connects to the current sensor and signal conditioning board - which will be discussed in the next section. The hall current sensor source is a simple custom board, designed to supply a constant supply voltage to the AlNiCo 5 hall sensor, determined at 5.085 V [26].

A.1.2. Sensors and signal conditioning

Two sensors are used in the original setup for logging of TM actuator performance. The Hall sensor mentioned previously measures air-gap flux feedback and a current sensor determines voltage drop over the magnetizing coil. The current sensor was custom designed by the electronic and mechanical support division of the TU Delft (DEMO) [26]. An overview of the PCB is provided in figure A.4a, sensor specifications in table A.4b and a detailed schematid in appendix C.

The sensor outputs are sent to the conditioning PCB shown in figure A.5a, which amplifies and filters the signals. In addition to the Hall and current sensor, it has the capability to handle up to six channels. It was originally designed for two sense coils - one for each of the AlNiCo 5 and 6 setups, two Hall sensors, one current sensor and a Hall current source. Due to malfunctioning of the latter, this has been replaced by the Hall current supply board referenced in section A.1.1. Detailed schematics are provided in appendix C.

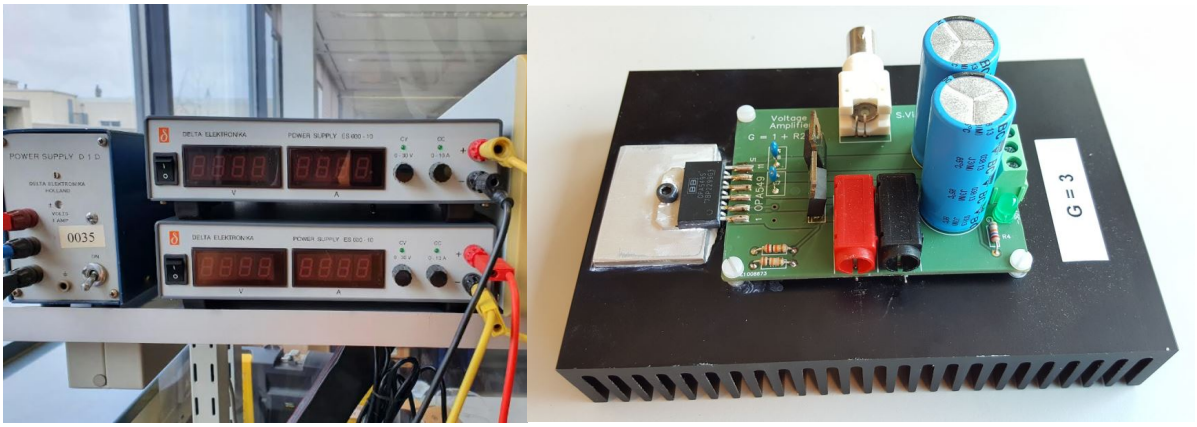

(a) (b)

Figure A.3: (a): ± 15 V power supply (left) supplying the PCB's, two times ± 30 V parallel-circuit power supplies (rigt) supplying the linear power amplifier and magnetizing coil. (b): the linear power amplifier, mounted on a custom PCB with large heat sink.

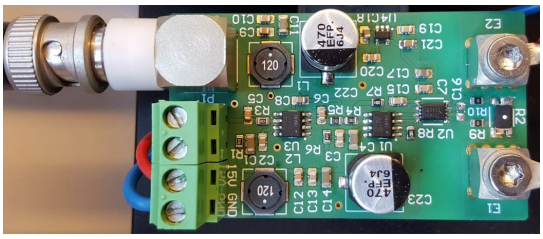

(a)

Parameter	Value	SI Unit
Current sensor		
Range	± 10	$[A]$
Sensitivity	2	$[AV^{-1}]$
Resolution	≈ 5	$[mA]$
Bandwidth	3	$[kHz]$

(b)

Figure A.4: (a): Custom current sensor PCB. (b):Current sensor summarized properties, adapted from [26].

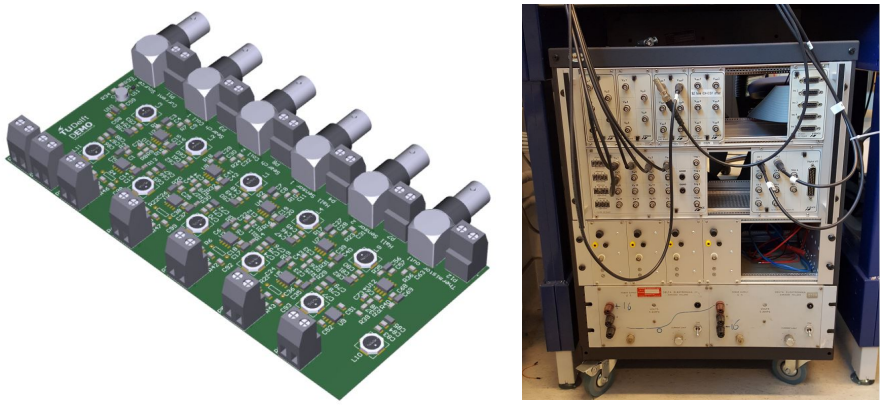

(a) (b)

Figure A.5: (a): Custom PCB six-channel signal conditioning board. (b): the dSPACE RTI1005 cabinet.

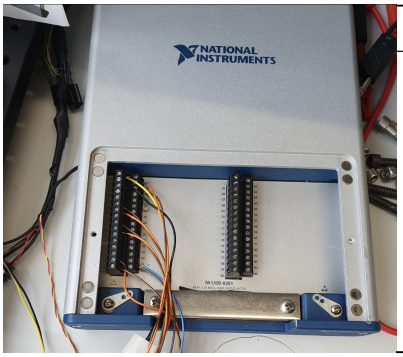

(a)

Pin	Type	Measurement
AI0	Analog in	Distance sensor $[x_{pos}]$
AI2	Analog in	AlNiCo 5 Hall sensor $[B_g]$
AI3	Analog in	Current sensor $[I]$
AO0	Analog out	(De-) magnetizing voltage $[U_s]$
AO1	Analog out	Hall current source

(b)

Figure A.6: (a): Overview of the NI 6351 USB X DAQmx module. (b): DAQmx pin arrangement. Three input sensors are used for varying degrees of control, output voltage U_s is variable between $\pm 10V$ - Hall current source voltage is kept constant at 5.085 V.

A.1.3. Data log/send

In Viëtor's research, data was recorded by using a dSPACE RTI1005 PPC Board - which acts like the brain of the setup [26]. The tuning script is run in real-time on the board, which delivers a signal between $\pm 10V$ to the linear power amplifier. This is then amplified with a gain of 3, sending the signal to the magnetizing coil. Within the setup, the current and Hall sensor respectively measure the voltage drop and gap flux density. After passing through the signal conditioning board, the signals are recorded in separate channels. Matlab postprocessing then allows for analysis of the tuning data. The dSPACE cabinet is shown in figure A.5b for completion, but was replaced in this research by a National Instruments 6351 USBX DAQmx I/O device in order to allow for modernized hard- and software. This will be discussed in the next section.

A.2. Hardware additions

In this research, three hardware upgrades have been perfromed. Each addition is shortly summarized below.

A.2.1. National Instruments (NI) DAQmx module

The hard- and software used in the original setup dates from approximately 2005. Running with a long outdated version of Matlab, an old Windows XP desktop and the discontinued dSPACE RTI1005 cabinet caused the desire for future-proofing of the experimental setup. This was originally intended to be replaced by a National Instruments CompactRIO chassis [18]. During this research, however, the conversion from dSPACE to CompactRIO FPGA proved to be too big of a challenge. This was mainly caused by a change in both soft- and hardware - because switching to NI systems also meant using LabView instead of Matlab.

Instead of switching immediately to an FPGA-based application, the easy-to-use NI 6351 USBX DAQmx module [19] was selected - with the input and output pins connected as shown in figure A.6a and table A.6b. Although the module is capable of sampling at 1.25 MSs^{-1} - spread out over all analog channels - the connection to an external pc appeared to be the bottleneck of this setup. Connected to a simple laptop running LabView, DAQ sampling times would often exceed the computation speed achievable on the laptop. This way, loop iterations and thus tuning times remained limited, respectively at 20 and 500 ms. It is therefore recommended to transfer the tuning algorithms to an FPGA-based application such as CompactRIO, so that refresh tuning rates can be matched to high sampling speeds - improving both control and tuning times.

Choosing the DAQmx module allowed this research to rewrite the tuning algorithms in LabVIEW - significantly modernizing the experimental setup. More on this in appendix B.

A.2.2. Distance sensor subassembly

In order to expand the setup for dynamic-gap operation, the Micro Epsilon optoNCDT ILD1420-10 laser triangulation distance sensor has been added to the experimental setup [16]. The sensor is placed on a bridge, consisting of three milled aluminium brackets, providing sturdy support while still allowing the Thorlabs linear stage to move freely underneath. The subassembly is depicted in figure A.7a, with technical data in table A.7b.

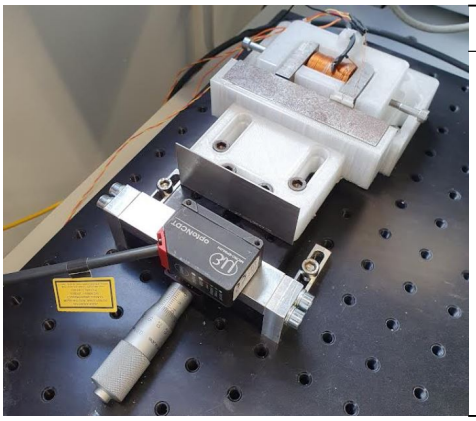

(a)

Parameter	Value	SI Unit
Measuring range	10	mm
Start measuring range	20	mm
Mid measuring range	25	mm
End measuring range	30	mm
Measuring rate	4	kHz
Linearity	$\pm$ 8	μm
Repeatability	0.5	μm

(b)

Figure A.7: (a): Overview of the added distance sensor. The optoNCDT sensor is mounted on a bridge, supported by two brackets that can be slid backwards and forwards for coarse adjustments. (b): Summarized laser distance sensor specifications

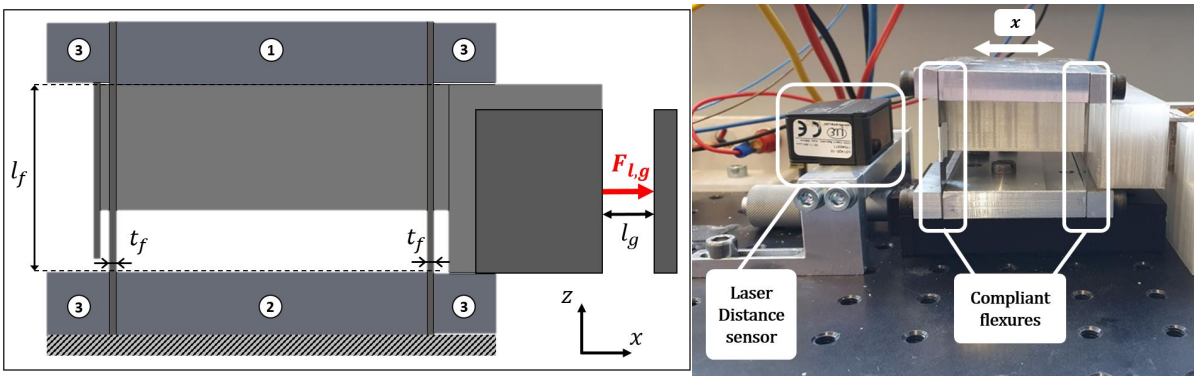

(a) (b)

Figure A.8: (a): Side-view of the dynamic stage subassembly. (b): Another side-view of the assembled assembly - secured on top of the manual linear stage.

Using the slots that have been milled in the sensor brackets, the sensor can be coarsely aligned with the stator - so that the motions will remain within the 10 mm measuring range. Fine adjustments can then independently be performed using the Thorlabs linear stage. For the measurements conducted within this research, the 0.5 μm repeatability provided ample resolution. However, if one were to desire accurate measurements of TM position errors, it might be beneficial to exchange the sensor for one with increased measurement resolution.

A.2.3. Modular moving stage subassembly

In order to allow for dynamic motion during tuning cycles, a moving-stage subassembly has been designed and built - allowing it to be attached to the existing setup. A side-view render of the setup is provided in figure A.8a, with the built setup shown in figure A.8b. Mover components are milled from 6068-grade Aluminium, with the flexures laser-cut from hardened spring steel. The PMMA mover yoke bracket can be bolted to component 1 by means of threaded holes. The entire subassembly is fixed to the Thorlabs manual linear stage with bolts threading through component 2. Components 3 can be clamped to the faces of 1 and 2, in turn clamping the flexures inbetween. Mover stroke as a result of flexure thickness can be calculated by using:

$$\text{stroke} = (l_{g,0} - l_g) = \frac{B_g^2 A_g}{\mu_0} \frac{l_f^3}{2E b_f t_f^3} \tag{A.1}$$

Magnetic circuit dimensions are defined with $l_{g,0}$ as initial and l_g as measured gap length, B_g the measured gap flux density, A_g gap cross-sectional area and μ_0 the permeability of free space. Compliant system parameters are represented by table A.3.

Table A.3: Measured and obtained flexure dimensions and parameters

Symbol	Value	SI unit	Comment
Flexures (Hardened spring steel)			
n_f	4		Number of flexures
l_f	30	mm	Flexure free length
t	0.4	mm	Thickness
b	12.7	mm	In-plane width
E	180	GPa	Young's modulus

The flexures are dimensioned with a length of 50 mm, but because of the clamping mechanism the free length only stretches for 30 mm. Additionally, they have been designed to place the point of attraction force very close to the center of the flexure: the discrepancy is only 5 mm. Because of this, the moment around the mover can be considered negligible - eliminating the concern for flexure buckling.

Additionally, the compliant mechanisms topology warrants some concern for z-axis displacement. If this displacement becomes too large, the mover and stator yokes no longer align - causing a change in A_g. The z-axis deflection can be written as [12]:

$$u_z = \frac{3}{5}\frac{u_x^2}{l_f} \tag{A.2}$$

Considering worst-case x-axis displacements to be in the order of 1 mm, this in combination with flexure length l_f yields z-axis displacements in the order of 2 μm. The air-gap surface area change this would cause is so small, it can be considered negligible.

B

Experimental Software

B.1. Prerequisites

The demagnetizing controller has been programmed using LabView - in order to be compatible with the NI DAQmx module. Though the data flow must be altered in future work in order to become compatible with FPGA-based applications, it serves a modern baseline for the SMST and MMST algorithms. To run the program, it is recommended to use the NI Labview 2020 32 bit standard version, as this version appears to be compatible with all necessary drivers and add-ons. If another version is given preference, please be aware to install at least the 32 bit version - as some drivers and add-ons are only available in this format. An overview of recommended packages is shown in figure B.1. Additionally, it is recommended to install the latest drivers for the DAQmx and CompactRIO devices.

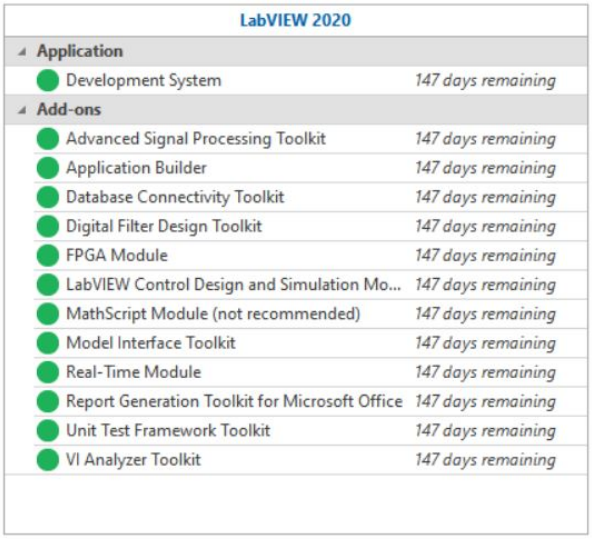

Figure B.1: Recommended Labview 2020 32 bit standard development system and additional toolkits/modules.

B.2. User interface

LabView offers a large array of possibilities for the user to make extensive user interfaces. The interface built for this research is shown in figure B.2.

In the leftmost column, pulse train times can be set. We distinguish full cycle time and tuning time - which represents the time reserved for demagnetizing. Additionally, it allows the user to set the number of consecutive tuning cycles, the limit of saturation voltage and the desired air-gap flux density.

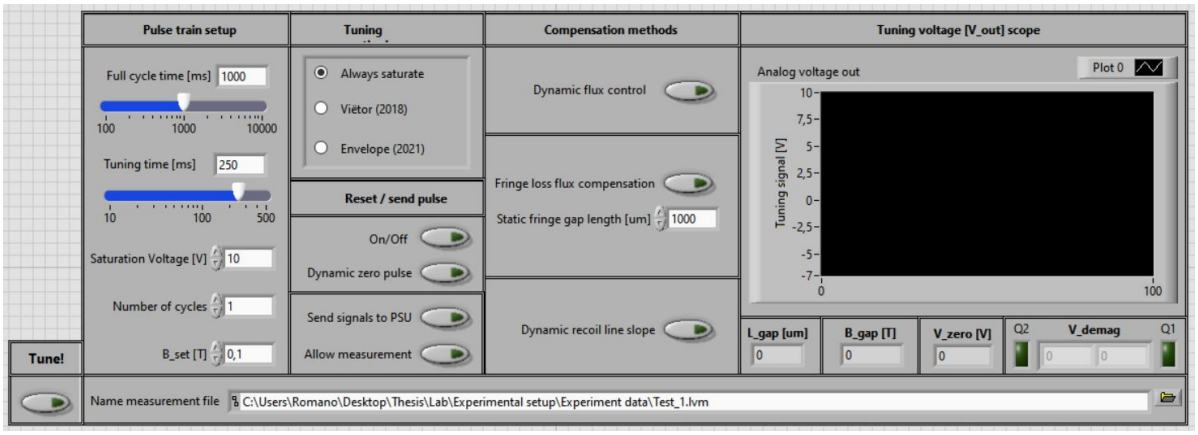

Figure B.2: User interface built using LabView.

Next to this, the tuning type can be selected. Always saturate represents the basic SMST method. With the Viëtor method, up-steps are saturated whereas down-steps do not use saturation. Finally, Envelope corresponds to the MMST method, where saturation is always avoided. Below this section, we can choose a zero-step between each of the tuning cycles. Send signals to PSU allows the user to troubleshoot the sequence without activation of the power supply - which is mostly a safety feature. Lastly, enabling allow measurement allows datalogging by the DAQmx module. Otherwise, the tuning cycle will not be recorded - which allows for quick and easy testing.

The 'compensation methods' - column allows the user to choose between the four compensation methods presented in chapter 3. Each method can be chosen separately, or stacked on top of the others. Some final features include a live window displaying the output voltage, live gap length and B_g measurements and corner-point selection indications.

B.3. Data flow

The data flow behind this dashboard consists of five consecutive tuning steps, all programmed within a for-loop iterating every 10 ms. Step 1 - shown in figure B.3 - revolves around reading the measurements from the sensors. From these, the Hall and current sensors are used for the compensation methods.

In step 2, the read sensor data is combined with known circuit parameters - as shown in figure B.4. The corner-point calculations are performed within the large script block. Using this, the result is compared to the measured gap flux density, and fed to the transfer functions of the tuning first and second quadrant tuning controllers. These output the required coil voltage, which is then sent to step 3.

In step 3 - shown in figure B.5 - the tuning sequence pulse train type is determined, similar to a switch. Depending on the tuning method selected, the step characteristics change. For example, if MMST is selected, we demagnetize immediately in the first step. When SMST is selected, the first step is dedicated to saturation, after which demagnetizing occurs in step two. A third slot remains reserved at all times for the zero-step and decay. Pulse data is sent to step 4.

Step 4, which is shown in conjunction with step 5 in figure B.6, sorts the tuning step characteristics provided by 3. It then places them in a tuning sequence, setting up the complete voltage pulse train. If applicable, a default zero-step can be added to the end of the tuning sequence. Finally, the signals are sent to step 5 where signals are sent to the power supplies, and data is logged. Depending on the options selected by the user, these can also be independently disabled.

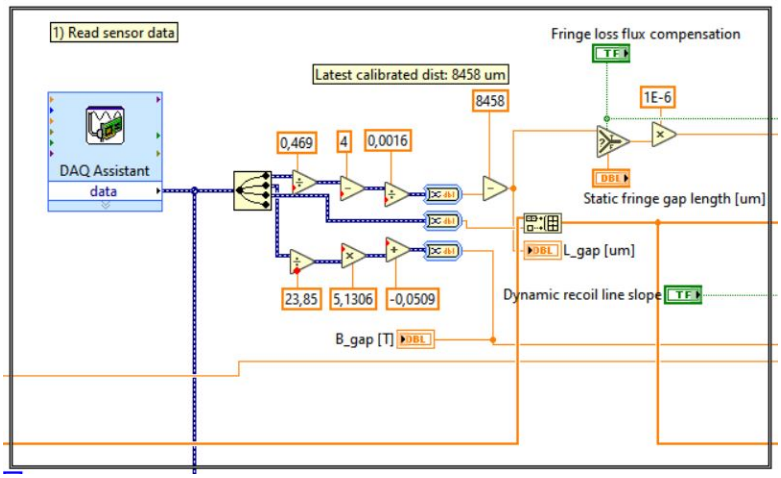

Figure B.3: Step 1: Reading sensor data

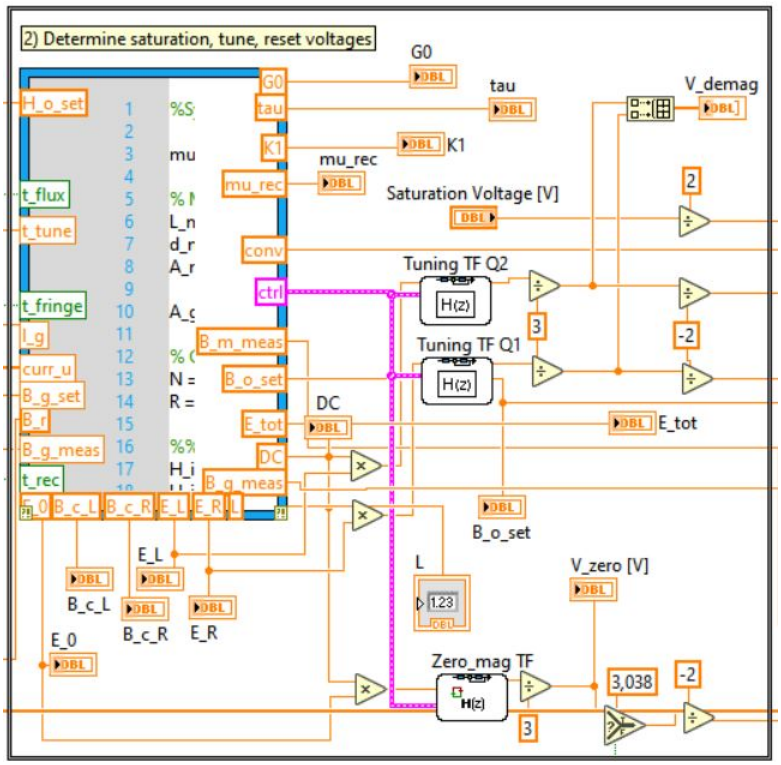

Figure B.4: Step 2: Determining (de-) magnetization voltages

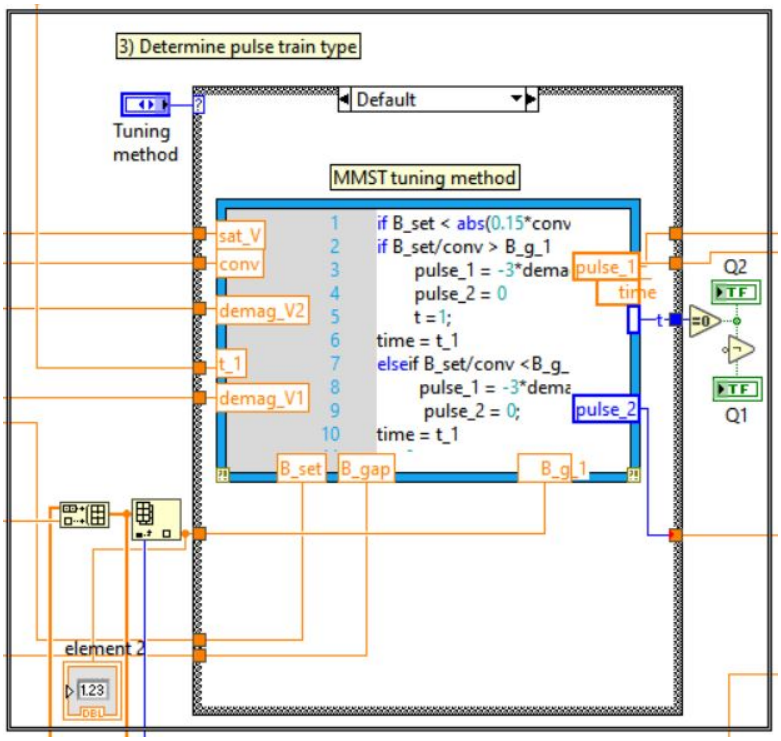

Figure B.5: Step 3: Selecting pulse train type: SMST, Hybrid or MMST

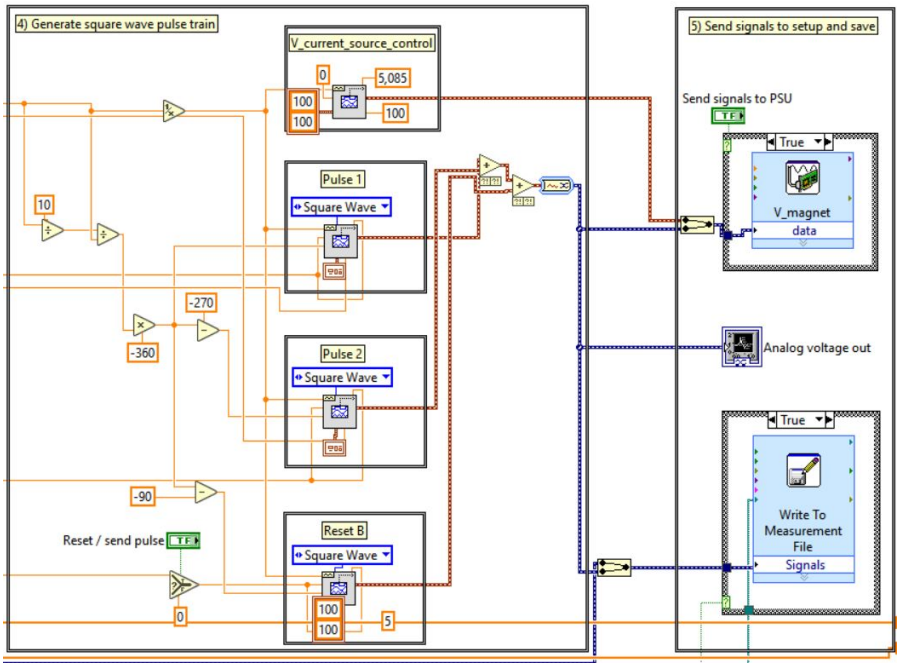

Figure B.6: Steps 4 and 5: Generating square wave pulse train and sending/logging data

B.4. Scripts

The script blocks used in steps 3 and 4 are attached to the end of this appendix.

Corner-point prediction and control transfer function setup

```
%% Corner-point prediction method

%% Introduce constant parameters

mu_0 = 4*pi*10^(-7);            % permeability of free space [-]

% Magnetic circuit dimensions
L_m = 30.20e-3;                 % length [m]
d_m = 9.83e-3;                  % diamter [m]
A_m = 0.25*pi*d_m^2;            % magnet surface [m^2]

% avg pole surface [m^2]
A_g = (9.98e-3*19.96e-3+10.01e-3*20.07e-3)/2;

% Coil parameters
N = 668;                                % amount of turns [-]
R = 3.5;                                % coil resistance [ohm]

%% Demagnetizing controller
H_int_L = 55.1e3;               % left coercivity point AlNiCo 5
H_int_R = 54.4e3 ;              % right coercivity point AlNiCo 5

mu_rmax = 250;                  % max material permeability
mu_rec_avg = 5.529;             % constant recoil line slope
                                        % without DRS compensation

% required controller BW, gain-scheduled
omega_c =50+(B_g_set/0.100)*35;

if t_fringe ==true              % if FF compensation is enabled:
        K1 = 2.44*(-67890*(l_g)^2 + 476.24*l_g + 0.5924);
else
        K1 = 2.44;                      % k1 is constant if disabled
end
K2 = 1.10;                              % k2 always constant

%Calculate required corner point
conv = K1*(A_g/A_m);            % convert from gap to magnet flux density
B_m_meas = conv*B_g_meas;

B_o_set = conv*B_g_set;         % calculate operating point
H_o_set = -K2*(2*l_g/L_m)*(B_g_set/mu_0);

if t_rec == true                % if DRS is enabled, use compensation
        B_r = (B_o_set-4.69*H_o_set*mu_0)/(1+0.955*H_o_set*mu_0);
        mu_rec = 0.955*B_r+4.69;
else                                    % otherwise, use constant recoil line
        B_r = (B_o_set-mu_0*mu_rec_avg*H_o_set);
        mu_rec = mu_rec_avg;
end
%mu_rec_r =4.45;                %experiment for different Q1 slopes
```

```
B_c_L = (B_r - mu_0*mu_rmax*H_int_L)/((mu_rmax/mu_rec)-1)+B_r;
B_c_R = (B_r + mu_0*mu_rmax*H_int_R)/((mu_rmax/mu_rec_r)-1)+B_r;
B_c_0 = (-mu_0*mu_rmax*H_int_L)/((mu_rmax/mu_rec)-1);
                                                    % above: q1 and q2 corner-point and zero
                                                    % predictions

E_L = B_c_L/conv-B_g_meas;      %error calculations q1, q2 and zero
E_R = B_c_R/conv-B_g_meas;
E_0 = B_c_0/conv-B_g_meas;

%% Model terms for inverse model control:
G0 =(N/A_m)/(R*((K2/K1)*((2*l_g)/(A_g*mu_0))+(L_m)/(A_m*mu_0*mu_rmax)));
L = N^2*((K2*2*l_g)/(K1*A_g*mu_0)+(L_m)/(A_m*mu_0*mu_rmax))^(-1);
tau = L/R;
DC  = omega_c/G0;
                                                    % above: system DC gain, inductance

%% system TF - coefficients obtained using Matlab c2d function
num =  [0.03145 -0.02145];
den = [1 -1];
ctrl = tf(num,den);

%% PPI control TF - coefficients obtained using Matlab c2d function
a = 0.01005;
b = 0.00995;
num2 = [a -b];
den2 = [1 -1];

%% Enable PPI flux feedback control
if t_flux == true
pi_ctrl = tf(num2,den2);
else
pi_ctrl = 0;
end

%% Set up total control transfer function
ctrl = ctrl+pi_ctrl;

%Energy used
t_step = 1/100;             % time elapsed per sampling step, in [s]
%Hysteresis loss
E_hyst_max = 2*1.25*50e3*L_m*A_m;
%Coil loss
a_Current = 0.5;
b_Current = 5.0142;
I_coil = (curr_u-b_Current)/a_Current;
P_coil = I_coil.^2*R;
E_coil = cumsum(t_step*P_coil);
% quick estimation of total energy consumed [J]
E_tot = E_coil(end)+E_hyst_max;
```

SMST method algorithm

```
%% Vietor SMST method algorithm
if B_set/conv > B_g_1                    %if set value is larger than measured:
        pulse_1 = sat_V;                         %saturate first, then demagnetize
        pulse_2 = -demag_V
        time = 5;
elseif B_set/conv < B_g_1                %elseif set value is smaller than measured:
        pulse_1 = -3*demag_V;            %demagnetize, empty second step
        pulse_2 = 0;
        time = t_1;
else
        pulse_1 = 0;                             %otherwise, do nothing
        pulse_2 = 0;
end
```

MMST method algorithm

```
%% MMST method algorithm
if B_set < abs(0.15*conv);               %if set value is smaller than limit, use MMST
        if B_set/conv > B_g_1            %if new value is larger than current, select Q1
                pulse_1 = -3*demag_V1;
                pulse_2 = 0
                t =1;
                time = t_1
        elseif B_set/conv < B_g_1        %if new value is smaller than current, select Q2
                pulse_1 = -3*demag_V2;
                pulse_2 = 0;
                time = t_1
                t = 0;
        end
elseif B_set>=abs(0.2)                   %if set value is smaller than limit, saturate
        pulse_1 = sat_V;
        pulse_2 = 0;
end
```

C

Component Datasheets

C.1. Magnetics - AlNiCo 5

,

Technical Data Sheet - Alnico Magnets

Alnico Magnets

Alnico magnets have the best temperature coefficients of any magnet material.
Alnico magnets should be regarded as the best choice in extremely high temperature applications.
Alnico magnets can be produced by Casting or Sintering. Alnico is also rarely made by Bonding within a binder.
Cast Alnico is the most common form of Alnico magnet. Casting is often used to get "near net shape" Alnico magnets.
Casting Alnico is cost effective for both low and high volume, for small and very large magnets.
Sintered Alnico is cost effective for medium to high volume runs due to tooling cost. The parts are generally small to medium.
Sintered Alnico magnets are not so commonly used due to lower magnetic performance and limitation to simpler shapes.
Anisotropic magnets have the direction of magnetisation (DoM) permanently within the structure and give the maximum performance.
Isotropic magnets can be magnetised in many ways as they have no preferred direction of magnetisation but give reduced performance.
Cast Alnico 5 is the most common grade of Alnico, with the LNG44 variant of Alnico 5 (Alcomax 3) being the most popular.
Alnico5, Alnico 8 and Alnico 9 all exist with several sub-grades with differing performance characteristics.
Where the shape is new, tooling charges may apply. It is common for the magnet pole faces to be machined to finish.
Alnico produced to specific Br, Hc, Hci and BHmax may be possible but at extra cost. Keeping within normal grades is advised.
Custom or bespoke magnet shapes may carry an additional tooling cost and even a minimum order charge.
Alnico Assemblies are also possible.

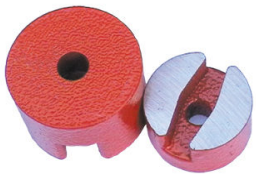

Anisotropic Cast Alnico

Typical Range of Values

Material	Br		Hc (Hcb)		Hci (Hcj)		BHmax	
	T	kG	kA/m	kOe	kA/m	kOe	kJ/m³	MGOe
Alnico 5 (Alnico5_LNG34)	1.10	11.0	50	0.63	52	0.65	34	4.25
Alnico 5 (Alnico5_LNG37)	1.18	11.8	50	0.61	51	0.64	37	4.63
Alnico 5 (Alnico5_LNG40)	1.20	12.0	50	0.63	52	0.65	40	5.00
Alnico 5 (Alnico5_LNG44)	1.25	12.5	50	0.65	54	0.68	44	5.50
Alnico 6 (Alnico6_LNG28)	1.15	11.5	58	0.73	60	0.75	28	3.50
Alnico 5DG (Alnico5DG_LNG52)	1.30	13.0	56	0.70	58	0.73	52	6.50
Alnico 5-7 (Alnico5-7_LNG60)	1.35	13.5	58	0.73	60	0.75	60	7.50
Alnico 8 (Alnico8_LNGT38)	0.80	8.0	110	1.38	112	1.4	38	4.75
Alnico 8 (Alnico8_LNGT40)	0.85	8.5	115	1.44	117	1.46	40	5.00
Alnico 8 (Alnico8_LNGT44)	0.90	9.0	115	1.44	117	1.46	44	5.50
Alnico 8HC (Alnico8HC_LNGT36J)	0.72	7.2	150	1.88	152	1.90	36	4.50
Alnico 9 (Alnico9_LNGT60)	1.00	10.0	110	1.38	112	1.4	60	7.50
Alnico 9 (Alnico9_LNGT72)	1.05	10.5	115	1.44	117	1.46	72	9.00
Alnico 9 (Alnico9_LNGT80)	1.08	10.8	120	1.50	122	1.53	80	10.00

Alnico 5 (LNG44) = Alcomax 3 = Alnico 500 = LNG44
Alnico 6 (LNG28) = Alcomax 4 = Alnico 400 = LNG28
Alnico 5DG (LNG52) = Alcomax 3SC = Alnico 600 = LNG52
Alnico 5-7 (LNG60) = Columax = Alnico 700 = LNG60
Alnico 8 (LNGT44) = Hycomax 3 = Alnico 8HE = LNGT44
Alnico 8 (LNGT40) = Hycomax 2 = Alnico 8H = LNGT40
Alnico 8 (LNGT38) = Alnico 8B = LNGT38
Alnico 8HC (LNGT36J) = Alnico 8HC = LNGT36J

Anisotropic Sintered Alnico

Typical Range of Values

Material	Br		Hc (Hcb)		Hci (Hcj)		BHmax	
	T	kG	kA/m	kOe	kA/m	kOe	kJ/m³	MGOe
Alnico 5 (Alnico5_FLNG34)	1.15	11.5	48	0.60	50	0.63	34	4.25
Alnico 6 (Alnico6_FLNG28)	1.10	11.0	58	0.73	60	0.75	28	3.50
Alnico 8HC (Alnico8HC_FLNG36J)	0.72	7.2	150	1.88	152	1.90	36	4.50
Alnico 8 (Alnico8_FLNGT38)	0.80	8.0	110	1.38	112	1.40	38	4.75
Alnico 8 (Alnico8_FLNGT44)	0.85	8.5	120	1.50	122	1.53	44	5.50
Alnico 8 (Alnico8_FLNGT48)	0.92	9.2	125	1.56	127	1.59	48	5.50

Isotropic Cast Alnico

Typical Range of Values

Material	Br		Hc (Hcb)		Hci (Hcj)		BHmax	
	T	kG	kA/m	kOe	kA/m	kOe	kJ/m³	MGOe
Alnico 3 (Alnico3_LN10)	0.65	6.5	38	0.48	40	0.50	10	1.25
Alnico 2 (Alnico2_LNG12)	0.75	7.5	45	0.56	46	0.58	12	1.50
Alnico 8 (Alnico8_LNG18)	0.55	5.5	90	1.13	97	1.21	18	2.25

Isotropic Sintered Alnico

Typical Range of Values

Material	Br		Hc (Hcb)		Hci (Hcj)		BHmax	
	T	kG	kA/m	kOe	kA/m	kOe	kJ/m³	MGOe
Alnico 3 (Alnico3_FLN10)	0.65	6.5	40	0.50	42	0.53	10	1.25
Alnico 2 (Alnico2_FLNG12)	0.75	7.5	45	0.56	46	0.58	12	1.50
Alnico 8 (Alnico8_FLNGT18)	0.60	6.0	95	1.19	98	1.23	18	2.25
Alnico 8 (Alnico8_FLNGT20)	0.62	6.2	100	1.25	105	1.31	20	2.50

Bonded Alnico

Typical Range of Values

Material	Br		Hc (Hcb)		Hci (Hcj)		BHmax	
	T	kG	kA/m	kOe	kA/m	kOe	kJ/m³	MGOe
Alnico_BLN7	0.31	3.1	79	1.00	103	0.85	6.77	0.86
Alnico_BLN8	0.34	3.4	83	1.05	107	1.00	7.96	1.00

Additional Information

The magnet shape, its environment, and the actual application affect how the Alnico magnet will perform.
The Intrinsic curve (not the Normal curve, although similar in shape for Alnico) is needed to assist in determining magnet suitability.
For Alnico, it is important to keep the working point above the "knee" of the Intrinsic curve to avoid severe demagnetisation.
Rotating machines and generators using Alnico need careful design due to the varying air gap during rotor rotation.
We can assist in designing in resistance to demagnetisation. We can guide you with your design options.
A length to diameter (L/D) ratio of at least 4 or 5 is a rule of thumb guide when using Alnico. A high L/D ratio is important for resisting demagnetising.
External demagnetising factors such as other magnets and electromagnets must be taken into account. They will put a field onto the magnet risking demagnetising it.
Even pushing two Alnico magnets in repulsion into each other can weaken their output. However careful handling will quickly resolve this. Alnico can be remagnetised.
The risk of demagnetisation of Alnico is reduced by improving the working point (e.g. use a longer magnet, increase the L/D ratio, use a higher Hc, introduce magnetic steel to the circuit, etc).
Alnico magnets have the best temperature coefficients of any magnet type. Alnico has the least change in field output over a change in temperature. They can also operate at the highest temperatures of any magnet.
Cast Alnico can have a blackened surface - this is the "As Cast" finish with the surface texture coming from the sand cast mold. Machining of the Alnico (e.g. precision ground pole faces) leaves a bright silvery metallic finish.
Very small air holes may be seen from time to time within the structure of cast Alnico magnets. This is natural for cast magnets (due to the casting process) and cannot be avoided.
If you have any more questions, require technical assistance and would like a quotation, simply contact us.
Although we have made every attempt to provide accurate information, we do reserve the right to change any of the information in this document without notice.
We cannot accept any responsibility or liability for any errors or problems caused by using any of the information provided.

Physical Characteristics (Typical)

Characteristic	Symbol	Unit	Value
Density	D	g/cc	6.9-7.3
Vickers Hardness	Hv	D.P.N	520-700
Curie Temperature	Tc	°C	800
Compression Strength	C.S	N/mm²	300-400
Coefficient of Thermal Expansion	C//	10^{-6}/°C	11.5-13
	C⊥	10^{-6}/°C	11.5-13
Electrical Resistivity	ρ	μ Ω.cm	45-70
Tensile Strength	σ_{UTS} or S_U	x10^6 Pa	20-450 (37 LNG44)
Hardness		Rockwell	45-55
Curie Temperature	Tc	°C	810-860

Max Working Temperature
(Please note - your application will affect the performance available)

Material	Maximum recommended temperature
Alnico 2	450 degrees C
Alnico 3	450 degrees C
Alnico 5	525 degrees C
Alnico 6	525 degrees C
Alnico 5DG	525 degrees C
Alnico 5-7	525 degrees C
Alnico 8	550 degrees C
Alnico 8HC	550 degrees C
Alnico 9	550 degrees C
Bonded Alnico	150-200 degrees C (binder limiting)

Corrosion Resistance

Alnico is regarded as having very good to excellent corrosion resistance for most applications.
Because iron exists within the Alnico alloy, corrosion may be seen during prolonged exposure to water.
Alnico can be coated or painted (e.g. Red Paint) but this is often only for aesthetic purposes.

Temperature coefficients

Rev.Temp.Coef. of Induction (Br), α, %/°C	Rev.Temp.Coef. of Intrinsic Coercivity (Hci), β, %/°C
-0.03 (Alnico 2, Cast)	-0.02 (Alnico 2, Cast)
-0.035 (Alnico 2, Sintered)	-0.025 (Alnico 2, Sintered)
-0.035 (Alnico 3, Cast)	-0.025 (Alnico 3, Cast)
-0.03 (Alnico 3, Sintered)	-0.02 (Alnico 3, Sintered)
-0.02 (Alnico 5, Cast and Sintered)	+0.01 (Alnico 5, Cast and Sintered)
-0.02 (Alnico 6, Cast and Sintered)	+0.03 (Alnico 6, Cast and Sintered)
-0.02 (Alnico 5DG, Cast)	+0.03 (Alnico 5DG, Cast)
-0.02 (Alnico 5-7, Cast)	+0.03 (Alnico 5-7, Cast)
-0.025 (Alnico 8, Cast and Sintered)	+0.01 (Alnico 8, Cast and Sintered)
-0.025 (Alnico 8HC, Cast and Sintered)	+0.01 (Alnico 8HC, Cast and Sintered)
-0.025 (Alnico 9, Cast and Sintered)	+0.01 (Alnico 9, Cast and Sintered)

Example Alnico second quadrant demagnetisation BH curve

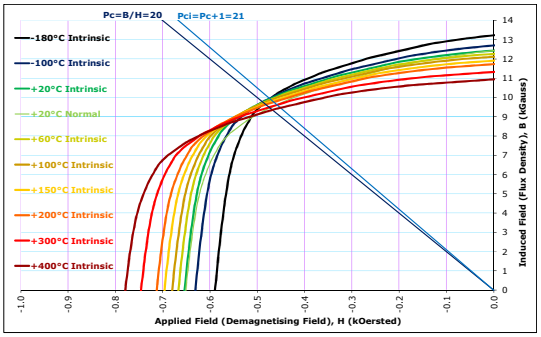

www.eclipsemagnetics.com
sales@eclipsemagnetics.com
Tel: +44 (0)114 225 0600
Fax: +44 (0)114 225 0610

FM31278

C.2. Hall sensor datasheet

’

HE144

Advanced Sensor Technology

Linear High Precision

Analog Hall Sensor HE144

Features

- Large magnetic field range - below milli-Tesla to over 10 Tesla
- Very small linearity error - typically 0,1 % up to 1,5 T
- Optimized for low Hall sensor current - typical 1000 Ohm and 0,2 Volt/Tesla at 1 mA
- Very high sensitivity
- Low noise
- Low drift
- Low inductive zero component, low EMC pickup
- Low temperature coefficients
- Very wide operating temperature range
- Very low PHE, Planar Hall Effect Error
- Very flat miniature package
- Pin compatible with Siemens®/Infineon® KSY14 and KSY44

Deviation from linearity at 1mA, 20 °C
Comparison with Infineon KSY44

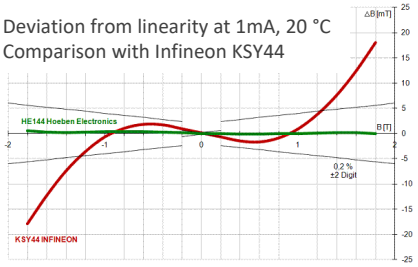

Our products are lead free devices, compliant with RoHS, REACH and ‘Japan green’ demands.

Typical applications

- Magnetic field measurements
- Oil drill measurement
- Position and rotation sensing
- Distance and thickness measurements
- Aerospace
- Current and power measurement
- Multi-sensor and differential usage
- Control of motor flux strength
- Windmills
- Movement sensing

Asensor Technology AB
Maskinvägen 6
746 30 Bålsta
Sweden

When Performance Matters

E-mail: hallsensor@asensor.eu
Phone: +46 8 590 755 10
Phone (NL): +31 6 515 900 81
www.asensor.eu

Specifications HE144

Electrical specifications		Values
Advised supply current		0,1 to 2,0 mA recommended 1 mA*
Open-circuit Hall voltage B=1 T		typical 200 mV at I=1 mA min 180 to max 360
Temperature coefficient of open-circuit Hall voltage B=1 T, at 25°C		typical -0,015 %/K at I=1 mA min -0,02 to max 0,02
Ohmic offset voltage B=0 T		≤± 12 mV at I=1 mA typical 10 mV **
Temperature coefficient of ohmic offset voltage B=0 T		typical 40 ppm/K (6,7 µT/K) at I=1 mA
Linearity of Hall voltage at I=1 mA	B = ± 0 to 1 T B = ± 1 to 2,4 T	≤± 0,2 % typical ≤± 0,1 % Limit not specified typical ≤± 0,2 %
Supply side internal resistance B=0 T		900 to 1250 Ω typical 1000 Ω
Hall side internal resistance B=0 T		900 to 1700 Ω typical 1000 Ω
Thermal conductivity in air		≥ 1,5 mW/K
Thermal conductivity soldered		≥ 2,2 mW/K
Bandwidth		Not specified (contact us)

* Optimal signal to noise ratio and low power consumption

** Variations within the same production batch are very small.

Absolute maximum ratings		Values
Supply current		10 mA
Operating temperature	**P-version**	-40 to +170 °C
	SH-version	-40 to +125 °C
	T-version	-40 to +125 °C
	HT-version	-40 to +200 °C

For very low (cryogenic down to a few Kelvin) or very high (over 200 °C) temperature applications, contact us for more information.

C.3. PCB schematics - Linear power amplifier

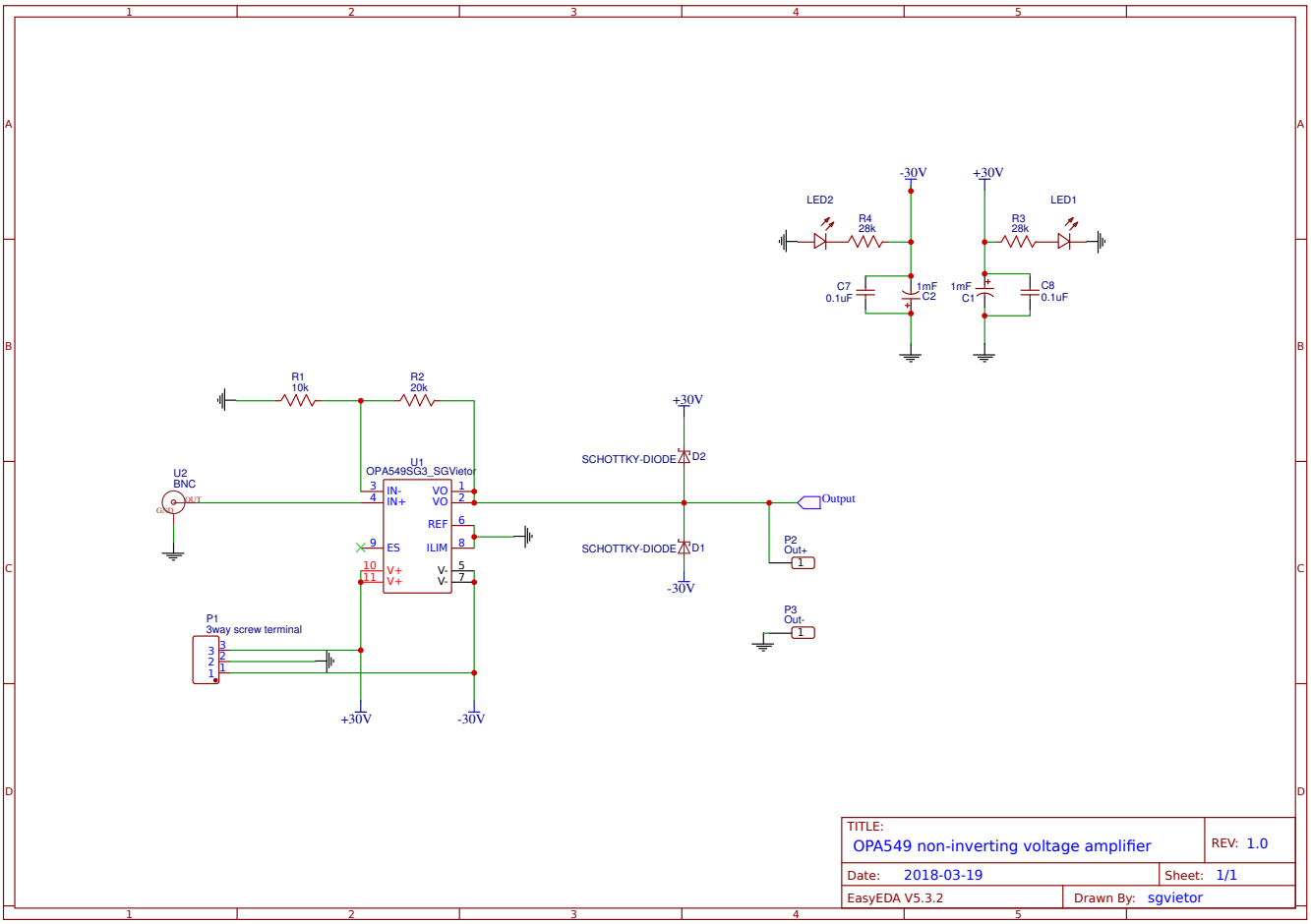

C.4. PCB schematics - Current sensor

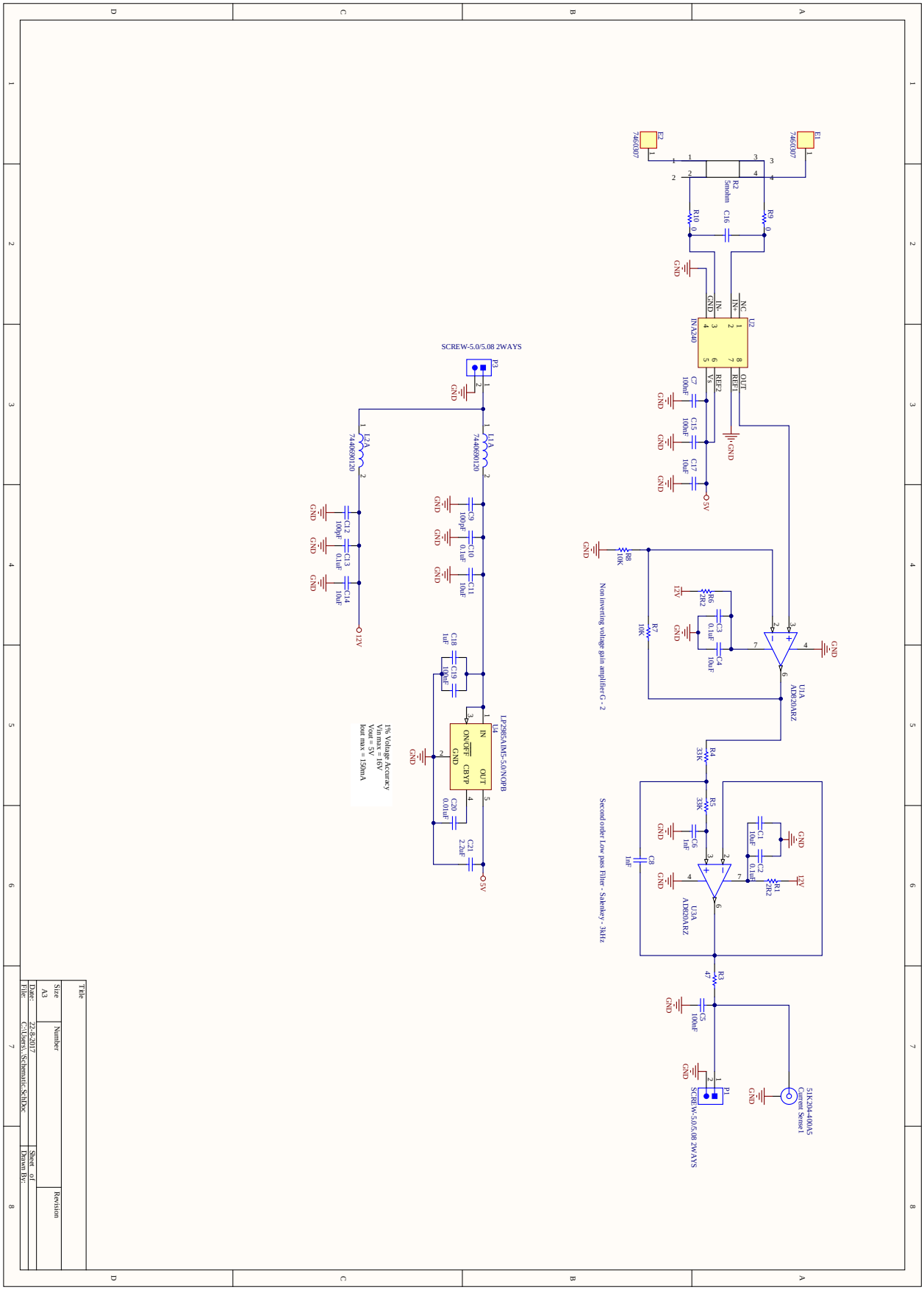

C.5. PCB schematics - Signal conditioning board

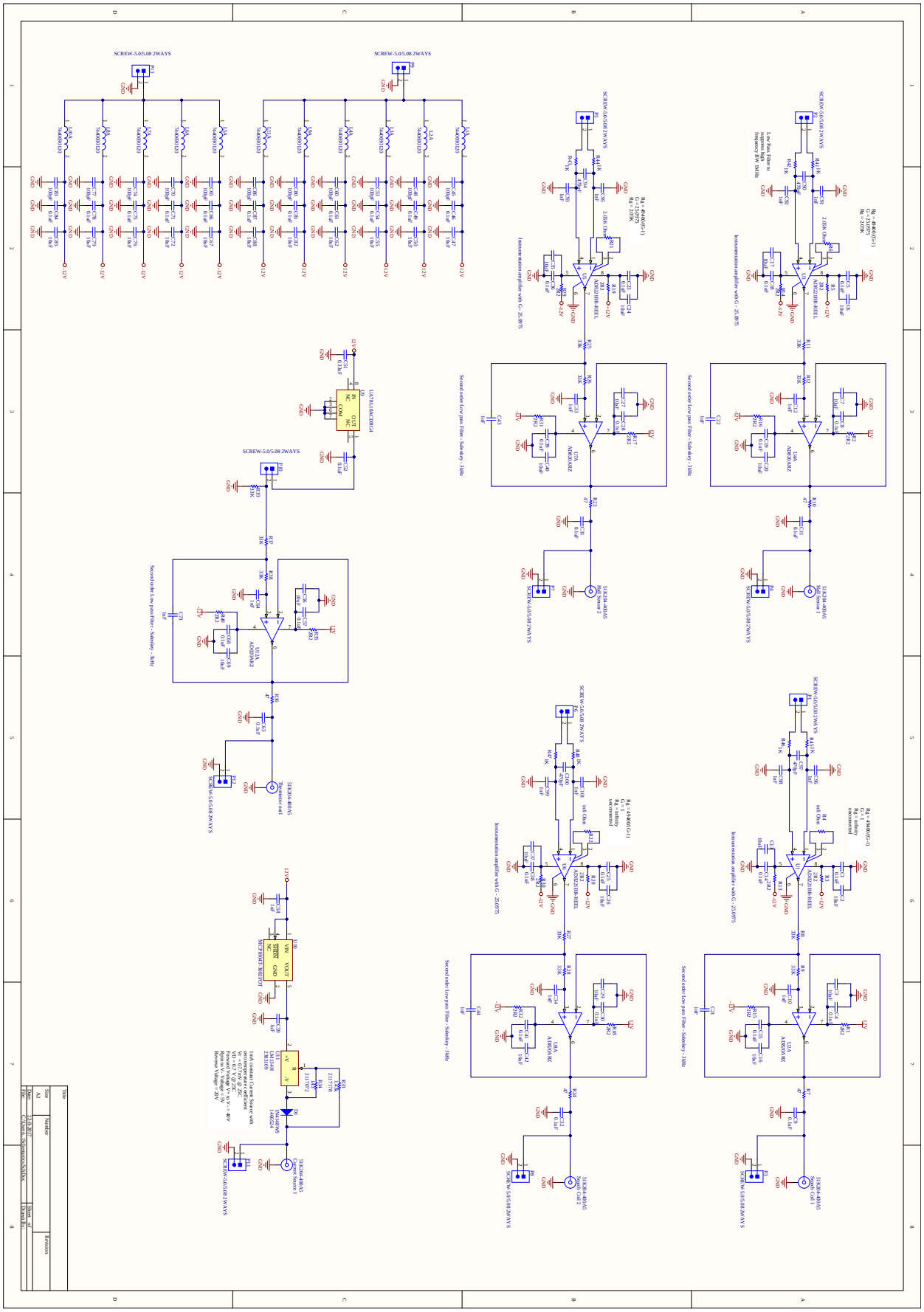

D

Recommended Literature

Summarized below, the interested reader will find a reading list of recommended literature. Subdivided into theory regarding magnetism, actuator design and Tunable Magnet actuatos, the list details some of the books that proved to be most valuable when performing this research.

D.1. Magnetism

Books that theoretically detail permanent magnets, modelling, circuit design and hysteresis:

- **Permanent magnet materials and their application [3]** - *Peter Campbell* - Book (204 pages)
  Concise, easy-to-read and comprehensive introduction to permanent magnets, circuit operation and hysteresis. It is recommended to start with this book, as it provides a very well-written introduction to the subject.

- **Advances in permanent magnetism [20]** - *Rollin J. Parker* - Book (336 pages)
  Excellent alternative to the book by Campbell. Provides similar insights, adding to this more emphasis on applications, flux measurement techniques and (de-) magnetization, albeit a bit harder to read.

- **Electromagnetic devices [22]** - *Herbert C. Roters* - Book (560 pages)
  Although even the book was printed in 1941, it still provides insightful information concerning magnetic circuit design. Additionally, methods of analytically modelling flux leakage and fringing effects are derived.

- **Hysteresis in magnetism [2]** - *Giorgio Bertotti* - Book (558 pages)
  Excellent overview of methods to describe hysteresis analytically. Although not used extensively in this research, it provides the basis of the work performed by Viëtor, by detailing methods of Preisach hysteresis modelling. The book is quite dense and technical, so prerequisite knowledge is advised.

D.2. High-precision actuator design

Books, disserations and papers that detail the design, comparison and application of high-precision actuators:

- **The design of high performance mechatronics [17]** - *Robert Munnig Schmidt* - Book (901 pages)
  Excellent and complete handbook concerning all aspects of high-tech system design. Providing insights in motion system dynamics, motion control, electromagnetic actuators and high-tech applications, the book can be used as a complete reference.

- **Comparison of linear voice coil and reluctance actuators for high-precision applications [27]** - *Nilles H. Vrijsen* - Paper (12 pages)
  Nice overview of types of linear precision actuators, detailing the difference between Lorentz and reluctance actuators - supported by experimental analysis.

- **Design and Optimization of a Magnetic Gravity Compensator [10]** - *Sven A.J. Hol* - Dissertation (200 pages)
  Extensive overview of magnetic gravity compensator theory and design. Many other MGC papers and dissertations refer back to this fundamental work, such as [8] and [28].

D.3. Tunable Magnet actuators

Papers and dissertations that can be considered fundamental to this research in TM actuator design and control:

- **Electropermanent Magnetic Connectors and Actuators: Devices and Their Application in Programmable Matter [13]** - *Ara N. Knaian* - Dissertation (206 pages)
  The work on Switchable Magnet connectors by A.N. Knaian can provides good insight in magnetic material arrangements, switching control algorithms and practical applications.
- **Tunable Magnets: Modeling and Validation for Dynamic and Precision Applications [26]** - *Silvan G. Viëtor* - Thesis (132 pages)
  This research is a continuation of the work performed by S.G. Viëtor in 2018. Therefore, his thesis can be regarded the most fundamental piece of literature that made this research possible. Extensive and easy-to-read, it provides an excellent introduction to Tunable Magnet actuators.

Bibliography

[1] ASML. EUV Lithography Machines. *url: https://www.asml.com/en/products/euv-lithography-systems*, (accessed29-07-2021), 2021.

[2] G. Bertotti. *Hysteresis in magnetism*. Academic Press, Inc, San Diego, CA, 1998. ISBN 0-12-093270-9.

[3] Peter Campbell. *Permanent Magnet Materials and their Application*. Cambridge University Press, 1994. ISBN 0-521-24996-1. doi: 10.1017/cbo9780511623073.

[4] Peter Campbell and Saad A. Al-Murshid. A Model Of Anisotropic Alnico Magnets For Field Computation. *IEEE Transactions on Magnetics*, 18(3):898–904, 1982. ISSN 19410069. doi: 10.1109/TMAG.1982.1061943.

[5] Steve Constantinides. Semi-Hard Magnets: The important role of materials with intermediate coercivity. *Magnetics 2011*, 2011.

[6] Delta Elektronika. ES 030-10 specifications. *url: https://www.delta-elektronika.nl/en/products/dc-power-supplies-300w-es300-series.html*, (accessed: 29-07-2021), 2021.

[7] Delta Elektronika. D1D product manual. *url: https://www.delta-elektronika.nl/en/support/discontinued-products.html*, (accessed: 29-07-2021), 2021.

[8] R Deng, R Saathof, JW Spronck, S Hol, and RH Munnig Schmidt. Integrated 6-dof lorentz actuator with gravity compensator for precision positioning. *Proceedings of the 22$ˆ{nd}$ international conference on magnetically levitated systems and linear drives*, (September), 2014.

[9] Eclipse Magnets. Alnico Magnets Datasheet. pages 5–8, 2017.

[10] SAJ Hol. *Design and optimization of a magnetic gravity compensator*. Number 2004. 2004. ISBN 9038615639. doi: 10.6100/IR574485. URL `http://www.narcis.nl/publication/RecordID/oai:library.tue.nl:574485`.

[11] Thorsten Hüfner, Oliver Radler, Tom Ströhla, Thomas Sattel, Jasper Wesselingh, Alexander Vogler, and Dirk Eicher. A note on electromagnetic gravity compensation actuators based on soft electro-permanent magnets for adjustable reluctance force. *Proceedings of the 17th International Conference of the European Society for Precision Engineering and Nanotechnology, EUSPEN 2017*, (May):149–150, 2017.

[12] JPE Innovations. Compliant Mechanism Design. *url: https://www.jpe-innovations.com/precision-point/2-leaf-springs-parallel/*, (accessed: 29-07-2021), 2021.

[13] A Knaian. *Electropermanent magnetic connectors and actuators : devices and their application in programmable matter*. PhD thesis, Massachusetts Institute of Technology, 2010. URL `http://dspace.mit.edu/handle/1721.1/60151`.

[14] Stefan Kuiper, Niek Doelman, Evert Nieuwkoop, Ton Overtoom, Tjeerd Russchenberg, Martijn van Riel, Justin Wildschut, Max Baeten, Jet Human, Helma Spruit, Sanneke Brinkers, and Matthew Maniscalco. Electromagnetic deformable mirror development at TNO. *Advances in Optical and Mechanical Technologies for Telescopes and Instrumentation II*, 9912:991204, 2016. ISSN 1996756X. doi: 10.1117/12.2230891.

[15] E. A. Lomonova. Advanced actuation systems - State of the art: Fundamental and applied research. *2010 International Conference on Electrical Machines and Systems, ICEMS2010*, pages 13–24, 2010.

[16] Micro Epsilon. optoNCDT ILD1420-10 sensor. *url: https://www.micro-epsilon.com/displacement-position-sensors/laser-sensor/optoNCDT_1420_CL1/*, (accessed: 29-07-2021), 2021. URL `https://www.micro-epsilon.com/displacement-position-sensors/laser-sensor/optoNCDT{_}1420{_}CL1/`.

[17] R.H. Munnig Schmidt, G. Schitter, A. Rankers, and J. Van Eijk. *The Design of High Performance Mechatronics*. Delft University Press - IOS Press BV, Amsterdam, 2nd revise edition, 2014. ISBN 978-1-61499-367-4.

[18] National Instruments. CompactRIO FPGA module. *url: https://www.ni.com/nl-nl/shop/compactrio.html*, (accessed: 29-07-2021), 2021.

[19] National Instruments. USB-6351X DAQmx module. *url: https://www.ni.com/nl-nl/shop/hardware/products/multifunction-io-device.html?modelId=124936*, (accessed: 29-07-2021), 2021. URL https://www.ni.com/nl-nl/shop/hardware/products/multifunction-io-device.html?modelId=124936.

[20] R.J. Parker. *Advances in Permanent Magnetism*. John Wiley and Sons, Inc., 1990. ISBN 0-471-82293-0.

[21] Philips Innovation Services. Comparative evaluation of Lorentz and reluctance actuators. pages 1–3, 2016. URL https://www.innovationservices.philips.com/app/uploads/2017/01/comparative-evaluation-lorentz-reluctance-actuators-philips-precision-engineering-example.pdf.

[22] H.C. Roters. *Electromagnetic Devices*. John Wiley and Sons, Inc., New York, first edit edition, 1941.

[23] Hexu Sun, Jie Gao, Yan Dong, and Yi Zheng. Analysis of temperature field in switched reluctance motor based on finite-element. *Proceedings of the 11th International Conference on Electrical Machines and Systems, ICEMS 2008*, pages 597–601, 2008.

[24] Thorlabs. Optical Breadboard. *url: https://www.thorlabs.com/newgrouppage9.cfm? objectgroup_id=159*, (accessed: 29-07-2021), 2021.

[25] Thorlabs. Manual Linear Stage. *url: https://www.thorlabs.com/newgrouppage9.cfm? objectgroup_id=706*, (accessed: 29-07-2021), 2021.

[26] S. G. Viëtor. *Tunable Magnets: Modeling and Validation for Dynamic and Precision Applications*. PhD thesis, 2018.

[27] N. H. Vrijsen, J. W. Jansen, and E. A. Lomonova. Comparison of linear voice coil and reluctance actuators for high-precision applications. *Proceedings of EPE-PEMC 2010 - 14th International Power Electronics and Motion Control Conference*, (October), 2010. doi: 10.1109/EPEPEMC.2010.5606572.

[28] Xuan Wang, Valérie Pommier-Budinger, Aurélien Reysset, and Yves Gourinat. Simultaneous compensation of hysteresis and creep in a single piezoelectric actuator by open-loop control for quasi-static space active optics applications. *Control Engineering Practice*, 33:48–62, dec 2014. ISSN 0967-0661. doi: 10.1016/J.CONENGPRAC.2014.09.005.